Modeling Motion Detection in Striate Visual Cortex Using Massive Excitatory Feedback

Thesis by Humbert H. Suarez

In Partial Fulfillment of the Requirements

for the Degree of

Doctor of Philosophy

California Institute of Technology

Pasadena, California

1995

(Defended February 13, 1995)

Acknowledgements

Thanks to my advisor Christof Koch, who has provided much that made this work possible. Beyond providing constant feedback and innumerable suggestions during this research, he has always insisted on very high standards of excellence, for research quality as well as in technical writing, oral presentations, and scientific ethics. Last but not least, he is instrumental in maintaining a funloving, laid back atmosphere in his lab, that is very beneficial for creativity in research. He has always been approachable and only occasionally uses his authority, mostly to make demands on my expert cappuccino-making skills.

Rodney Douglas has provided and constantly reinforced many of the overall goals of this project and provided excellent guidance during his numerous stays in California.

My candidacy committee has provided useful feedback and comments. Thanks to John Allman, John Hopfield, Gilles Laurent, and Pietro Perona. Thanks also to Ojvind Bernander, Chris Chee, Martin Stemmler, and Marius Usher for stimulating scientific discussions. Thanks to Gary Holt for helping me with his knowledge of sophisticated perl scripts, and Wyeth Bair for helping with cross-correlation analyses.

Thanks to Pravin Tulachan, Dave Flowers, and Tom Tromey for help with my system management needs, and to all my fellow Koch Labers for tolerating me gobbling up more than my share of the lab's CPU time, memory, and disk space.

Thanks to all my friends, fellow CNS students, Caltechers, Jaycees, Toastmasters, and Pasadenans for making my thesis enjoyable and a learning experience in more than one dimension. Especially, thanks to the Moveable Feast committee (Chris Chee, Ernst Niebur, Martin Stemmler, and Marius Usher) for providing a venue for exploring innumerable Pasadenan eateries. Thanks also to the many Pasadena coffeehouses for providing me with a haven for quiet reading, writing, or indulging in my favorite addiction. And thanks to the California sunshine for warming my heart in between long stays in my air-conditioned office.

Finally, thanks to my father for motivating me to study the brain, which has proved to be a fascinating endeavor, and for fostering what I expect to be a lifelong habit of intellectual curiosity. Thanks to my mother for allowing me to move away from her love and from Europe, and setting me free in the wide world.

This research was supported by the Office of Naval Research, the Air Force Office of Scientific Research, the National Science Foundation, NIH grant EY06264-03, and the Parsons Foundation.

Abstract

This thesis is a detailed description and analysis of a model of direction-selective simple cells in cat striate visual cortex. There are three main defining features of our modeling effort compared to previous ones. (1) Local excitatory intracortical connections, known to be very numerous, are taken into account. (2) The model is very detailed: compartmental models of neurons are used and spiking is modeled using Hodgkin and Huxley-like active ionic currents. (3) Model responses are analyzed through standard electrophysiological methods and are compared in detail to physiology. Two separate operating modes are described. When the model acts as a proportional amplifier, contrast-response curves are relatively linear. In the hysteretic amplifier mode, contrast-response curves are much steeper initially, including an early portion with expansivity nonlinearity, but saturate abruptly at high contrasts. These features of the second mode are very similar to cortical contrast-response curves, but very different from the thalamus'. The second mode also predicts that hysteresis is latent in cortex, but that because of resetting through inhibition, cortical neurons do not fire in the absence of stimulation. In both modes, the model achieves strong amplification of the input through the excitatory cortical feedback. Amplification results in small changes in conductance for stimuli moving in the null direction, long a

puzzling experimental finding; direction selectivity also persists during blockade of all inhibition in a single cell, as observed in recent experiments. Due to the nonlinearity of this amplification, bandpass velocity-response curves of thalamic neurons can be transformed into velocity low-pass cortical curves. Direction selectivity is invariant over a wide range of contrasts and velocities, a prominent feature of direction-selective cells in cortex. The model also makes specific predictions concerning the effects of selective blockade of cortical inhibition on direction selectivity at different velocities. Finally, we address the important issue of testing experimentally the linearity of cortical neurons. The same intracellular linearity test that has been used for cortical neurons is performed on the model. Although the model has substantial nonlinearities, it appears quite linear according to the linearity test. We explain these surprising observations in detail, and conclude that such tests are much more limited in usefulness than apparent at first.

Contents

Chapter 1

Introduction

This thesis is a detailed description and analysis of a model of direction-selective simple cells in cat striate visual cortex. The impetus for modeling direction selectivity arises in part from the large body of experimental data available on these cells, concerning their physiological response properties, single-cell biophysics and morphology, and connectivity. However, there is another focus in this thesis, separate from direction selectivity. It arises from anatomical and physiological observations that have recently converged into a novel picture of local cortical circuits.

Cortical direction selectivity (DS) is usually thought to arise from a Barlow and Levick type feedforward scheme (Barlow and Levick, 1965), in which the response to the preferred direction of motion arises from the afferent input, while the response in the opposite (null) direction is suppressed by spatially offset inhibition (Bishop et al., 1971; Benevento et al., 1972; Emerson and Gerstein, 1977; Torre and Poggio, 1978; Ganz, 1984; Koch and Poggio, 1985; Ruff et al., 1987; Wörgötter and Holt, 1991; Maex and Orban, 1991; Wörgötter et al., 1992). Another class of models of direction selectivity were derived from spatio-temporal energy models of the psychophysics of motion detection (Burr, 1981; Watson and Ahumada, 1985; Adelson and Bergen,

1985). They are based on either purely linear spatio-temporal filtering (Reid et al., 1987, 1991; Hamilton et al., 1989; McLean and Palmer, 1989; Saul and Humphrey, 1990; McLean et al., 1994) or such filtering followed by an expansive nonlinearity (Albrecht and Geisler, 1991; DeAngelis et al., 1993; Heeger, 1993), and include both suppression in the null direction and facilitation in the preferred direction.

Variants of the first scheme are inconsistent with a number of features of cortical DS. In particular, these models fail to account for the massive excitatory interconnections seen in cortex, which numerically totally overshadow geniculo-cortical synapses. Indeed, only approximately 5-6% of all excitatory synapses onto a layer 4 spiny stellate cell is provided by thalamic afferents (Douglas and Martin, 1991; Peters and Payne, 1993; Ahmed et al., 1994). Even such an explicit nonlinear model based on intracellular data as the one by Carandini and Heeger (1994), completely disregards these anatomical findings.

Also, both classes of models fail to explain that intracellular *in vivo* recordings in cat simple cells fail to detect any changes in somatic input conductance during stimulation in the null direction (Douglas et al., 1988; Berman et al., 1991). In feedforward models, a large input from the direction symmetric lateral geniculate nucleus (LGN) is needed to generate the high firing rates observed during stimulation in the preferred direction. In the null direction, large inhibitory conductances changes would be needed to prevent the cell from firing to this excitatory input even in the absence of shunting inhibition. Physiological checks, assisted by simulations, have confirmed that these conductance changes should have been picked up by Douglas *et al.* (Koch et al., 1990; Douglas and Martin, 1991; Dehay et al., 1991; Berman et al., 1992). The remarkable lack of large inhibitory conductance changes has subsequently been confirmed by other laboratories (Pei et al., 1991; Ferster and Jagadeesh, 1992).

To explain these puzzling observations, Douglas and Martin (1990) proposed the *Canonical Microcircuit* of neocortex (Fig. 1.1b; see also Douglas and Martin, 1991a,

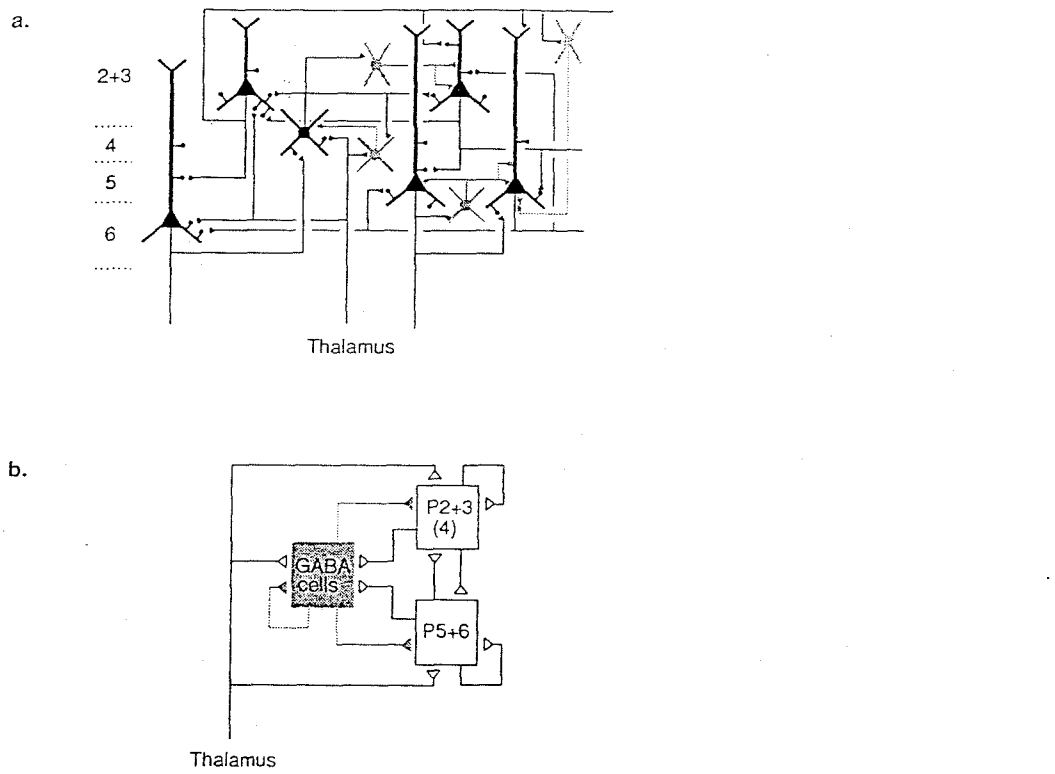

Figure 1.1: **Cortical circuitry and the Canonical Microcircuit. (a)** The basic neuronal types in cortex, their typical axonal arborizations and the laminar boundaries. Pyramidal cells and spiny stellate cells are drawn in black, while inhibitory, smooth interneurons are drawn shaded. **(b)** Cortical amplification in very schematic form. Superficial (P2 + 3(4)) and deep (P5 + 6) pyramidal cells are interconnected with a single pool of GABA cells. Open triangles indicate excitation and closed triangles inhibition (see Douglas et al., 1989; Douglas and Martin, 1991)

Berman *et al.*, 1991), which includes strong local excitatory connections among cortical pyramidal and spiny stellate cells. Only weak LGN input is needed, since in the preferred direction the cortico-cortical connections amplify the initial excitation coming from the LGN; counteracting the small LGN input in the null direction requires only weak inhibition below the detection limit of Douglas *et al.* (1988). In this view, Barlow-Levick inhibition in the null direction is combined with cortical amplification in the preferred direction, resulting in a direction-selective cortical cell.

Douglas and Martin (1991a) used computer simulations with continuous, mean-rate neurons to qualitatively verify some of the key concepts of their model. In this thesis, we perform much more realistic computer simulations, using spiking neurons described by compartmental models. We call this detailed model the *cortical amplifier* model, and compare in detail the properties of the cortical amplifier with those of a conventional *feedforward* model of DS, based on Barlow and Levick's scheme for retinal DS. We provide key insights into the model's functioning through detailed analysis. Through the model, we confront biophysics and anatomy with the known physiology. As a result, we provide novel, detailed explanations of cortical response properties and experimentally testable predictions. We also test directly the methodology of a physiological experiment, with surprising results.

In this thesis, we will see that the cortical amplifier circuit comes in two flavors, depending on the strength of the positive feedback. For moderate feedback strength, the pyramidal neurons' response increases proportionally to the stimulus strength over a substantial range of input values, before saturating very progressively. We call the model in this mode the *proportional amplifier.* For higher feedback, the response increases much faster over a narrow range of stimulus strengths, then saturates. Hysteresis is possible if inhibition is too weak, whereby the response persists even after stimulus withdrawal. We call the model in this mode the *hysteretic amplifier.* Since these two parameter regimes have substantially different response properties and lead

to different interpretations, we will investigate both modes in detail.

1.1 A guided tour

I will give here a quick overview of each chapter, describing briefly the procedures and main results.

Chapter 2 describes the cortical amplifier model and its components in detail, and introduces the analytical methods used later.

We first describe the three model neurons that are the basic building blocks of the direction selectivity model: the lateral geniculate nucleus (LGN) neurons that are modeled as a series of filters and used as input to cortex, and the compartmental models of the two cortical cell types (pyramidal or excitatory neurons, and smooth or inhibitory neurons). We then describe how these components are put together in the direction selectivity model. Finally, we explain the methods we used to analyze the model's output (including how contrast-response and velocity-response curves are calculated) and the procedures that define some of the experiments that we performed on the model.

Chapter 3 introduces a simplified theory of amplification in cortex at equilibrium, and describe the resulting dynamics too, in the linear approximation; two modes of amplification are discussed, *proportional* and *hysteretic* amplification; we demonstrate that hysteresis is latent in the hysteretic amplifier mode. In the last section of the chapter, we present a simplified dynamical model, known somewhat whimsically as DYNAMO.

Chapter 4 is a detailed investigation into the response properties and functioning of the cortical amplifier operating in the proportional mode, and compares it to a purely feedforward model of direction selectivity (the feedforward model). Input conductance changes little in the null direction. The contrast-response curves of the

model match certain cortical responses. Velocity-responses curves of the model are quite different from the LGN's and match physiology well. We explain the shape of the velocity-response curve through detailed analysis. Blocking inhibition in a single cell results in persistence of direction selectivity, and the model is linear to grating superposition, as are direction-selective cells in cortex. The model makes specific predictions concerning the effects of selective blockade of cortical inhibition on direction selectivity at different velocities.

Chapter 5 essentially parallels Chapter 4, but for the hysteretic amplification mode. Contrast-response curves are different for the hysteretic amplifier, but are very similar to those of cortical neurons. Velocity-response curves also match cortex well. Detailed analysis again allows us to understand the shapes of these curves. We propose that inhibition has a crucial role in resetting the cortical network after discharge, and draw parallels between the hysteretic mode and proposals for short-term memory.

Note that we have attempted to make these two chapters relatively self-contained, in that it is not necessary to read one of these chapters to understand the other one.

Chapter 6 directly probes the methodology of an intracellular linearity test based on grating superposition. After noting that the detailed models pass the test, we find that they present substantial nonlinearities. After showing in this way that the linearity test has only very limited usefulness, we proceed to explain its failures in detail. A surprising notion that emerges from this analysis is that cortical amplification is invisible if only measuring average intracellular potentials.

Chapter 7 discusses the assumptions behind the model. Assuming that cortex is in a given narrow region of a very high-dimensional parameter space is a major assumption, and we demonstrate that the model is very sensitive to the values of some parameters. We also describe a technical problem that complicated significantly our investigations of the hysteretic amplifier model.

Finally, Chapter 8 concludes the thesis by comparing proportional and hysteretic amplifiers and looking at the general lessons learned, and provides a perspective for future investigations. A final section gives a list of my publications while at Caltech.

Chapter 2

Building a model of direction selectivity in striate cortex

2.1 Introduction

This chapter describes the model and its components in detail, and introduces the analytical methods used later.

We describe all three models: the feedforward model, and the proportional and hysteretic amplifiers. These models and their context were introduced in Chapter 1.

The models describe events occurring in a small network of simple cells located in the primary visual cortex of the adult cat. For simplicity of implementation, only the ON portion of the X pathway is modeled (Lennie, 1980; Sherman, 1985). Visual input to the network is provided by a one-dimensional retino-geniculate module, transforming a given input, usually a moving bar or grating, into a series of spikes mimicking the output of the geniculate relay cells (Victor, 1987). The lateral geniculate nucleus (LGN) input is integrated by the network of excitatory and inhibitory neurons, which are identified here as pyramidal and smooth neurons (note, however,

that the excitatory neurons could also be spiny stellate cells in layer 4).

Section 2.2 describes the artificial visual stimuli provided to the model LGN neurons. Section 2.3 is about the LGN neurons; they are modeled as a series of filters. Section 2.4 gives a description of the compartmental models of the pyramidal and smooth neurons, including the noise sources present. Section 2.5 is about how these components are put together in the direction selectivity models. Section 2.6 explains how response properties are computed from the model's output, how linearity to grating superposition is tested, and how GABA blocking experiments are performed. Section 2.7 describes briefly the computer implementation of the model.

2.2 Visual stimuli

Visual stimuli are provided to the model as 1-D pixel frames (see Fig. 2.3) with 1′ per pixel resolution and an effective frame rate of 10 kHz. The amplitude at each pixel corresponds to the fractional deviation from the mean luminance. Moving bar stimuli were modeled by a group of same-valued pixels, moving at a constant velocity. Drifting sine wave gratings were modeled by moving patterns of pixel values that are modulated sinusoidally over space, and contrast-reversal stationary gratings by patterns of pixel values with separable spatial and temporal sinusoidal modulations. We give here the definition of stimulus contrast used in this paper. For a bar, it is the Weber contrast:

$$C = 100\frac{L - L_b}{L_b}, \tag{2.1}$$

where L is the luminance of the bar and L_b is the luminance of the background. For a moving grating, we use the Rayleigh-Michelson contrast:

$$C = 100\frac{L_{max} - L_{min}}{L_{max} + L_{min}}, \tag{2.2}$$

where L_{max} and L_{min} are the maximum and minimum luminance in the pattern.

2.3 Retino-geniculate module

The dynamics of the geniculate input to striate cortex needs to be modeled with some care, because the timing of geniculate input is critical for direction selectivity, and because the velocity-response curves of our model cortical neurons are only meaningful if the velocity-response curve of the geniculate input is accurate. Beyond these considerations, the detailed properties of the retinal and geniculate cells are not central to our simulations, and so we simplified the visual input in a number of ways.

Most importantly, the response to visual stimulation of ON geniculate relay cells of the X type is computed as a transfer function, rather than by simulating their biophysical properties. As in Wehmeier *et al.* (1989), we model a patch of retinal cells located 1 *mm* away from the *area centralis*, or about 4.5° eccentricity. Receptive fields at that eccentricity have a difference of Gaussians, center-surround type of receptive field (Rodieck, 1965; Enroth-Cugell and Robson, 1966; Linsenmeier *et al.*, 1982; Enroth-Cugell *et al.*, 1983; see Fig. 2.1a) with a center diameter of approximately 30′ (Fig. 2.1c; Peichl and Waessle, 1979, Linsenmeier *et al.*, 1982). The cells respond to a light stimulus by a transiently high discharge rate that adapts to a maintained level (Fig. 2.1d). We used Victor's model (1987) of the center component of retinal X cells to simulate the temporal properties of our geniculate cells (Fig. 2.1b). The Victor model postulates a series of low-pass filters followed by a high-pass filter and some nonlinear processing at high contrast values. We used identical temporal filters for both center and surround, neglecting differences in their dynamics (Dawis et al., 1984). Following Victor's model, the surround's response was substracted from the center's. The output of a model LGN cell is technically speaking not separable in time and space, because of a small temporal delay (3 *msec*) we introduced

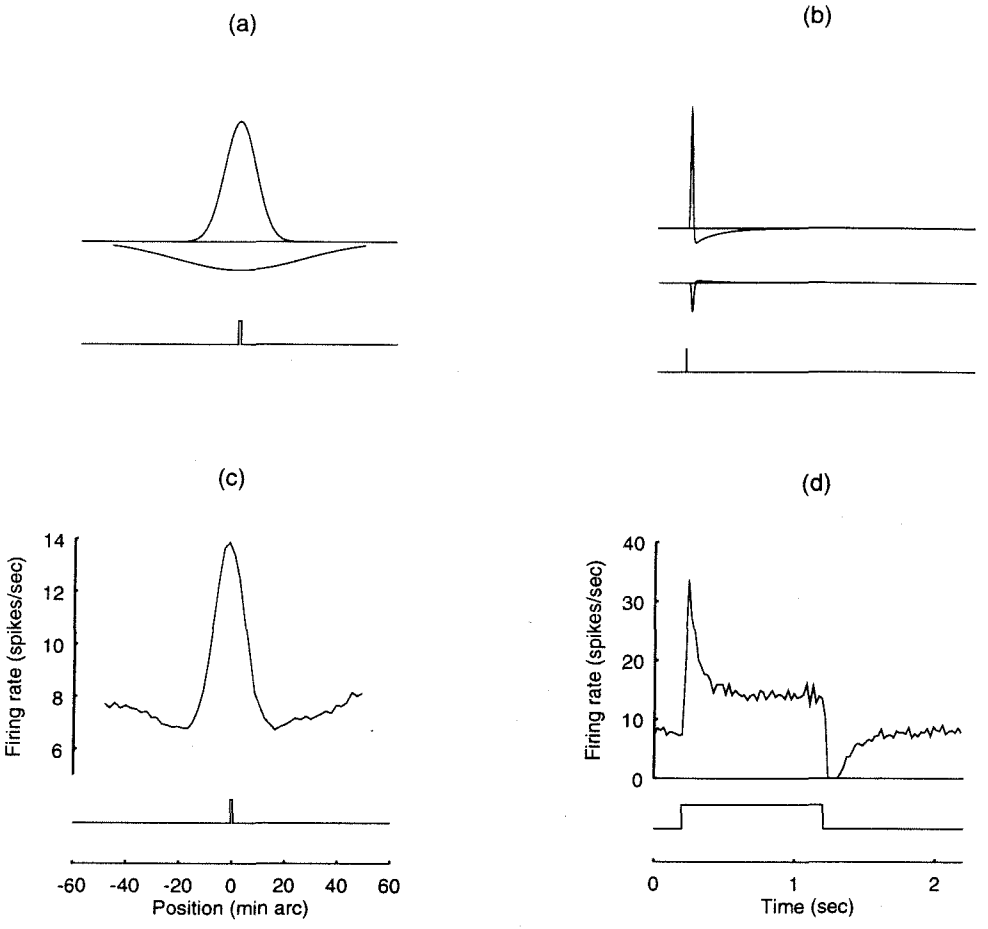

Figure 2.1: **Basic characteristics of the LGN model.** **(a)** Spatial filters for the center and surround, modulating the responses to a thin bar (shown here with 1′ width in the center of the receptive field). The σ of the Gaussians is 6′ for the center, and 24′ for the surround. **(b)** The impulse responses of the center and surround (to an impulse lasting 1 $msec$), summarizing the action of their temporal filters. **(c)** The sustained average response of an LGN neuron, in impulses/sec, to a thin bar (1′ width, 100% contrast). **(d)** Our geniculate cells respond to input with Poisson distributed spikes whose rate is modulated by the visual stimulus (superimposed onto a spontaneous firing activity of 8 Hz). We here show the mean rate of one LGN cell (in the form of a Post Stimulus Time Histogram; PSTH) in response to 1600 presentations of a thin bar (1′ width, 100% contrast) at the center of its receptive field.

between the center and the surround response, consistent with experimental observations (Enroth-Cugell et al., 1983). The continuous output of this filtering stage determines the instantaneous rate of a Poisson process that generates discrete impulses (spikes). We superimpose a spontaneous firing frequency of 8 Hz onto the stimulus-dependent response (Fig. 2.1d). For a 70% contrast bar moving at $10°/sec$, peak firing rates are around 140 Hz (see Fig. 4.8).

We used slightly different parameters values from Victor's (1987) retinal model, because of the different response amplitudes of LGN neurons (Bullier and Norton, 1979; Cleland and Lee, 1985; Kaplan et al., 1987). Additional contrast nonlinearities present in the LGN itself (Kaplan et al., 1987) are probably insignificant in the context of our simulations, and were not included in the model.

Only responses of the X pathway were simulated, because it accounts for most thalamic inputs to area 17 (Sherman, 1985; Ferster, 1989). Furthermore, since cortical direction selectivity does not require any significant interaction between the ON and OFF sub-systems (Schiller, 1982, 1992; Sherk and Horton, 1984), only responses of geniculate ON X neurons were simulated.

Spatially, the centers of the LGN neurons' receptive fields are positioned at one of six spatial locations which occur at 5′ intervals (Wörgötter and Koch, 1991). To ensure that each cortical neuron receives input from a realistic number of LGN neurons, the LGN array is two-dimensional: there are 13 LGN neurons at each of the 6 spatial positions (a 6 x 13 array) in the proportional amplifier model, and 208 in the hysteretic amplifier (a 6 x 208 array). The number of LGN neurons was increased for the hysteretic amplifier for the same reasons mentioned below for increasing the number of cortical neurons. Within each group of 13 or 208 cells, the one-dimensional spatial receptive fields are identical. Pyramidal neurons in cortex receive input from the first 5 groups of LGN neurons, and smooth neurons receive input from the last 5 groups of LGN neurons (see Fig. 2.3). Overall, there is a spatial offset of 5′ between

input fields of pyramidal and smooth neurons, providing the spatial asymmetry necessary for direction selectivity. Rather than connecting all 65 (1040) LGN cells to each cortical neuron, each geniculate afferent connects with a 30% probability to a given cortical neuron, so that on the average a cortical neuron receives input from $0.3 \cdot 5 \cdot 13 = 19.5$ (312) LGN cells. For the proportional amplifier, the number is low in comparison to estimates from experimental data (Tanaka, 1983; Freund et al., 1985a, 1985b; Peters and Payne, 1993; Peters et al., 1994); however, it is adequate when one considers that the model simulates only one subfield of cortical neurons and only geniculate ON afferents. For the hysteretic amplifier, the number is rather high. However, there are strong indications that it could be made significantly lower.

2.4 Pyramidal and smooth cells

Because we model the detailed dynamics of a network of cortical neurons, it is important that the underlying single cell model include the essence of most known dynamical properties of cortical neurons, with direct ties to parameters that can be measured experimentally. Thus, the cellular model takes into account the known morphology and biophysics of visual cortical neurons. In particular, our cells respond to synaptic input with a stream of discrete all-or-none action potentials, rather than with a continuous firing rate as in the vast majority of neural network models. Anatomical dimensions of a representative layer 5 pyramidal neuron and a smooth (basket) cell were obtained by reconstructing suitable cortical neurons that had been labelled intracellularly with horseradish peroxidase during *in vivo* experiments in the anesthetized, adult cat (Douglas et al., 1991). The 3-D coordinates and diameters of the dendritic arbor and soma yielded a model with many compartments that was reduced in a further step to either 3 or 4 compartments (Douglas and Martin, 1991; Bush and Sejnowski, 1993; Bernander, 1993). The aim was to capture the essen-

tial aspects of the neuronal biophysics without the need for the many hundreds of compartments that would be required for more detailed models.

2.4.1 Pyramidal cells

Each pyramidal neuron consists of an ellipsoidal somatic compartment, and three cylindrical compartments that represent the dendritic arbor. Each dendritic compartment is assigned a leak conductance ($R_m = 10,000\ \Omega cm^2$) and a particular profile of synaptically mediated membrane conductances (Fig. 2.2a). The soma contains five voltage-dependent ionic conductances that are modeled using Hodgkin-Huxley-like kinetics with voltage-independent time constants (Bush and Douglas, 1991; Bernander et al., 1991). The currents are a transient sodium and a delayed rectifier potassium current that underlie action potentials, a high-threshold calcium current, I_{Ca}, a calcium-dependent potassium current, I_{AHP}, and for the cortical amplifier model, a transient, A-like potassium current, I_A (not present in the hysteretic amplifier). I_{Ca} and I_{AHP} mediate the rapid (time constant $25 - 50msec$) adaptation seen in regular firing pyramidal cells (McCormick et al., 1985). After increasing during an action potential, intracellular calcium (in the somatic compartment) decays exponentially with a time-constant of 50 $msec$. This simplified cell's current-discharge curves (see Sections 3.2 and 3.4) are very similar to those of a substantially more complex pyramidal cell model that uses more than 300 compartments (Bernander et al., 1991).

At rest, the somatic input resistance, time constant and membrane potential of our pyramidal cells are 27.2 $M\Omega$, 7.75 $msec$ and $-66.5\ mV$ in the feedforward case, 52.9 $M\Omega$, 22.5 $msec$ and $-54.2\ mV$ for the proportional amplifier model, and 65.1 $M\Omega$, 21.3 $msec$ and $-57.0\ mV$ for the hysteretic amplifier model. The input resistance is much smaller in the feedforward than in the feedback case, since the LGN to pyramid synaptic weight is much larger (see Table 2.1) and therefore also the

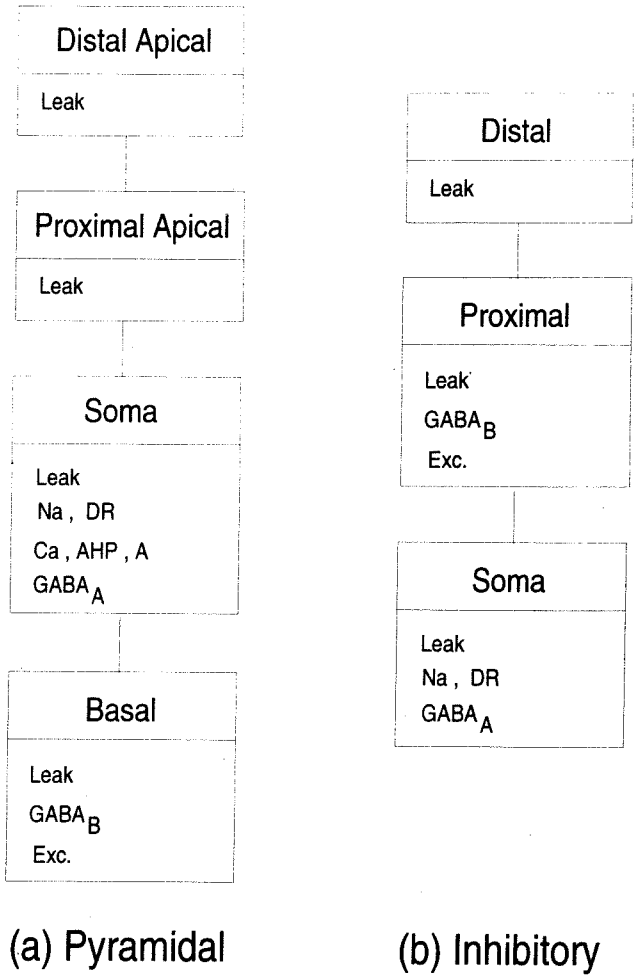

Figure 2.2: **Compartmental models of the pyramidal and smooth neurons.** Each compartment includes a number of membrane currents shown in the diagram. Not shown are the capacitances and axial resistances within and between each compartment. **(a)** Pyramidal cells each have four compartments, corresponding anatomically to the basal dendritic, somatic, proximal, and distal apical dendritic compartments. **(b)** Smooth GABAergic interneurons each have three compartments, for the somatic, proximal, and distal dendritic compartments. *Leak*: leak conductance. *Na*: transient sodium current. *Ca*: calcium current. *DR*: delayed rectifier K current. *AHP*: calcium-dependent K current. *A*: transient, inactivating K current (not present in hysteretic amplifier model). *Exc.*: synaptic excitatory current (from geniculo-cortical and cortico-cortical afferents).

synaptic background activity from the LGN. A larger input conductance also implies a smaller membrane time constant. The resting membrane potential is related to the neuron's threshold. The neuron's threshold, together with synaptic inhibition, contributes to direction selectivity; even if some LGN input is not cancelled by overlapping inhibition in the null direction, it will not result in any response as long as it remains subthreshold. Since the LGN weight is larger in the feedforward case, the pyramidal neuron's threshold has to be larger too.

2.4.2 Smooth cells

The smaller, smooth, GABAergic stellate cells are modeled by removing the basal compartment from our pyramidal cell model (Fig. 2.2b) and adjusting the size parameters for the remaining compartments (Douglas and Martin, 1991). I_{Ca}, I_{AHP}, and I_A were also removed to enable these cells to fire at high sustained rates without showing any adaptation, in agreement with intracellular data (McCormick et al., 1985). Smooth cell parameters are identical in the feedforward and cortical amplifier models; at rest, the input resistance, time constant and membrane potential of these cells is 65.2 $M\Omega$, 11.4 $msec$ and -56.0 mV. Compared to the cortical amplifier's pyramidal cells, despite the larger resting LGN input (because of the larger LGN weight, see Table 2.1), the input resistance is larger because of the smaller membrane area. The short time constant reflects the effect of the large geniculate background activity.

2.5 Network connectivity

A connection diagram of the cortical amplifier network in the proportional amplifier configuration is shown in Fig. 2.3. It comprises 40 pyramidal and 10 smoooth

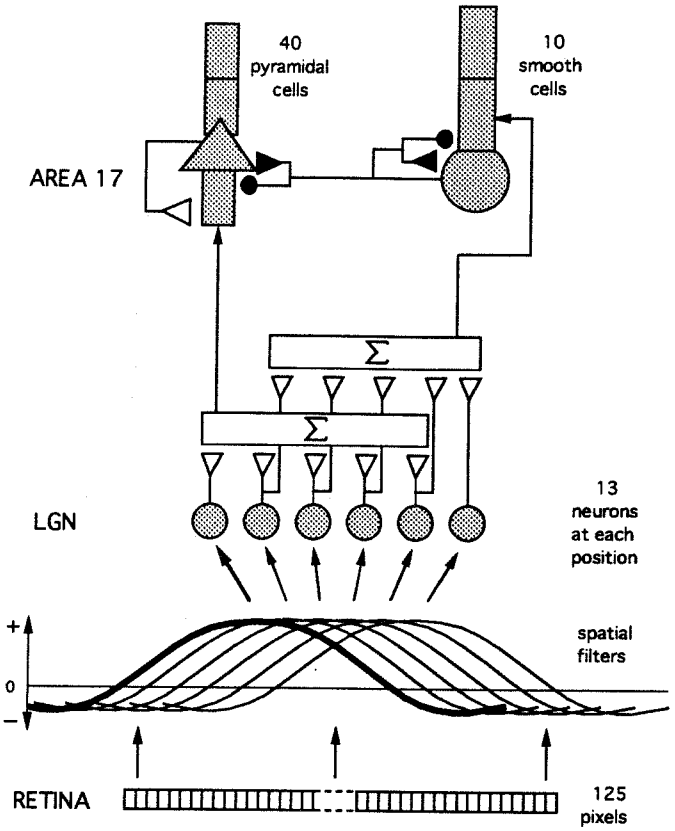

Figure 2.3: **Connectivity diagram of the direction selectivity model in the proportional amplifier configuration.** Input to LGN neurons comes from an one-dimensional array of retinal pixels. The intensities from those pixels are summed through difference-of-Gaussians spatial filters onto LGN neurons, with a spatially offset filter at each position. There are 13 LGN neurons at each of six spatial positions. The LGN neurons connect slightly differently with the two populations of cortical neurons, so that as a group the LGN inputs to the pyramids are spatially offset by 5′ with respect to those to the smooth neurons (Σ indicates convergence of the geniculate inputs onto cortical neurons). Each geniculate cell independently has a 30 % probability of making a synapse with its appropriate cortical target (see Section 2.3). The open triangle symbols denote excitatory connections, the filled triangles inhibitory $GABA_A$ connections, and the filled circles inhibitory $GABA_B$ connections.

neurons, respecting the known proportions of cortical neurons (Winfield et al., 1980; Beaulieu and Colonnier, 1983; Hamos et al., 1983; Gabbott and Somogyi, 1986; Peters and Payne, 1993). The connections between neurons reflect the connectivity of the canonical microcircuit with the exception that the pyramidal neurons do not connect to the inhibitory neurons. This lack of feedback inhibition in our current model substantially simplified our simulations. However, our model is compatible with feedback inhibition. Simulations with simplified neuron models (having continuous firing rate output instead of discrete action potentials, see Section 3.7) showed that suitable response characteristics can be obtained in the presence of these connections, including physiological contrast-response, velocity-response, DI-contrast and DI-velocity curves. In addition, and in contrast with the detailed simulations, smooth neurons now showed direction preference.

The hysteretic amplifier configuration is the same as the proportional amplifier, except that there are 640 pyramidal and 160 smooth neurons instead (in addition to there being 208 LGN neurons at each spatial position instead of 13, as mentioned previously). The number of neurons was increased to mitigate certain instabilities relating to the steepness of the contrast-response curve (see Section 7.4).

Each cortical connection drawn in Fig. 2.3 symbolizes synapses of equal strength from each neuron of one group to all neurons of the other group. Inhibition is of two types, $GABA_A$, or transient, and $GABA_B$, or sustained inhibition. As explained in Section 2.3, the LGN inputs to the smooth neurons are spatially displaced from those to the pyramidal neurons. Local inactivation experiments using GABA microiontophoresis provide some support for the presence of a spatial displacement between smooth neurons and the direction-selective pyramidal neurons that they inhibit (Eysel et al., 1988).

For the feedforward model, the connection diagram is similar to Fig. 2.3, except that there are no excitatory cortico-cortical connections, implementing a Barlow-

Levick scheme for direction selectivity (Barlow and Levick, 1965); the connection weights are different, as we will see below.

Because excitatory and inhibitory synaptic inputs change the local membrane conductance to a certain ion or ions, massive synaptic input can have a dramatic effect on a cell's spatio-temporal structure, in particular on the input resistance and time-constants (Bernander et al., 1991; Rapp et al., 1992). Therefore, it is important to explicitely model synaptic input as conductance change (in series with a battery), rather than a simple current injection, as common in nearly all neural network models.

The amplitudes of synaptic conductances and time constants that govern their behavior have yet to be determined experimentally in detail for pyramidal and spiny stellate cells in primary visual cortex (see also Bernander, 1993). However, there are estimates from the literature that can be used for constraining our model. This data is usually based on *in vitro* cortical preparations (Jack et al., 1975; Tanaka, 1983; Miles and Wong, 1984; Thomson et al., 1988; Connors et al., 1988; Bekkers and Stevens, 1989; Busch and Sakmann, 1990; Edwards et al., 1990; Kriegstein and LoTorco, 1990; Larkman et al., 1990; Lytton and Sejnowski, 1991; LaCaille, 1991; Mason et al., 1991; Williams and Johnston, 1991).

In the model, the excitatory postsynaptic currents arise exclusively from fast, voltage-independent non-NMDA or AMPA synapses located in the proximal dendritic compartment (Fig. 2.2). Voltage-dependent NMDA synaptic inputs are not included in the current version of our model (for discussion, see Section 7.2). However, because we wanted to retain the slower dynamics of the NMDA receptor, we adopt the compromise of using voltage-independent excitatory synaptic input with a decay of 20 *msec* rather than the few milliseconds appropriate for a pure AMPA synapse. A second reason for using a 20 *msec* decaying input is to compensate for the lack of distal dendritic compartments. The associated low-pass filtering will lead to a broadening of the synaptic current flowing into the soma.

Two types of inhibitory postsynaptic currents are included: fast, shunting, chloride based $GABA_A$ inhibitory synapses are located in the somatic compartment, while slow, hyperpolarizing, potassium-based $GABA_B$ inhibitory synapses are located in the dendritic compartments (Connors et al., 1988; Douglas and Martin, 1991).

The time-course of the geniculo-cortical and $GABA_B$ synaptic conductance change is a dual exponential (Wilson and Bower, 1989):

$$G(t) = e^{-t/\tau_1} - e^{-t/\tau_2}, \tag{2.3}$$

while that for the excitatory cortico-cortical synapse and the $GABA_A$ mediated response is a single exponential:

$$G(t) = e^{-t/\tau_1}. \tag{2.4}$$

Final synaptic parameter values are shown in Tables 2.1 (proportional amplifier and feedforward models) and 2.2 (hysteretic amplifier). For the proportional amplifier case, each connection's strength is in the range of individual synaptic contacts, while for the feedforward model some connections would be in the upper range for individual synaptic contacts; instead, they may correspond to several synaptic contacts; for the hysteretic amplifier, the connections strengths are significantly lower than experimentally measured values. For the cortical amplifier, the LGN-to-pyramidal weight was set so as to give a slightly suprathreshold excitation for low contrast values. The smooth-to-pyramidal $GABA_A$ and $GABA_B$ weights were just large enough to balance out the LGN excitation in the null direction over a range of velocities. For the proportional amplifier, the setting of the pyramidal-to-pyramidal weight was high enough to obtain peak firing rates that were compatible with experimental values (Orban et al., 1981a), but low enough to still have proportional amplification (see Section 3.3). For the hysteretic amplifier, the weight was high enough to have hysteresis, but low enough so that inhibition could still turn the network off after stimulation (see Sec-

From To	Connection strength pyramidal	smooth	Peak conductance pyramidal	smooth	Time constants τ_1	τ_2
FEEDFORWARD						
LGN	38.9	10.8	8.65	2.40	4.5	1.8
pyramidal	-	-	-	-		
smooth $GABA_A$	45.1	0.39	4.51	0.039	10	
smooth $GABA_B$	33.7	3.35	0.211	0.021	80	40
AMPLIFIER						
LGN	2.59	10.8	0.576	2.40	4.5	1.8
pyramidal	3.38	-	0.169	-	20	
smooth $GABA_A$	3.34	0.39	0.334	0.039	10	
smooth $GABA_B$	2.50	3.35	0.016	0.021	80	40

Table 2.1: Synaptic connectivity of our cortical module for the feedforward and proportional amplifier models. Connections are between all members of the cell types involved. The connection strength between two neurons is expressed in terms of the temporal integral over the postsynaptic conductance increase in response to a single presynaptic action potential, i.e., $\int g(t)dt$, in units of $pS \cdot sec$. The peak conductance is given in nS, as well as the synaptic time-constants, τ_1 and τ_2 (see eq. 2.3 and 2.4), in $msec$. The reversal potentials were 0 mV for all excitatory synapses, -75 mV for $GABA_A$ and -90 mV for $GABA_B$ synapses. All simulations in this paper were carried out with the same set of parameters.

tions 3.3 and 5.6). For the feedforward model, the LGN-to-pyramidal weight was large enough to enable model neurons to fire at physiological rates despite the strong delayed inhibition. Inhibitory connections were set according to the same criterion as in the cortical amplifier.

2.5.1 Noise

Two external noise sources provide trial-to-trial variability.

Firstly, the geniculate input itself consists of Poisson distributed spikes generated by the retino-geniculate module (see Section 2.3). Superimposed onto the stimulus

From To	Connection strength pyramidal	smooth	Peak conductance pyramidal	smooth	Time constants τ_1	τ_2
LGN	0.162	0.67	0.036	0.15	4.5	1.8
pyramidal	0.235	-	0.0117	-	20	
smooth $GABA_A$	0.209	0.024	0.021	0.0024	10	
smooth $GABA_B$	0.156	0.21	0.001	0.0013	80	40

Table 2.2: Synaptic connectivity of our cortical module for the hysteretic amplifier model. Connections are between all members of the cell types involved. The connection strength between two neurons is expressed in terms of the temporal integral over the postsynaptic conductance increase in response to a single presynaptic action potential, i.e. $\int g(t)dt$, in units of $pS \cdot sec$. The peak conductance (nS), and the synaptic time-constants, τ_1 and τ_2 (in $msec$; see eq. 2.3 and 2.4), are also given. The reversal potentials were 0 mV for all excitatory synapses, -75 mV for $GABA_A$ and -90 mV for $GABA_B$ synapses. All simulations in this paper were carried out with the same set of parameters.

driven geniculate response is a spontaneous firing activity of 8 Hz (Fig. 2.1d). Since the LGN weight is larger in the feedforward model than in the cortical amplifier model, the fluctuations in the resting somatic membrane potential are higher in the former case (see Fig. 4.1).

Secondly, some background noise is added to both pyramidal and smooth model neurons to simulate the effect of spontaneous activity in the numerous cortical neurons outside our network. Noise events are modelled either as conductance changes or as current injections. Parameters of each conductance change or current injection function are set so as to model inhibitory ($GABA_A$ or $GABA_B$) or excitatory non-NMDA synaptic inputs; the locations are the same as for these inputs. In the pyramidal neurons, we assume that 44% of the noise originates from current injections and the rest from spontaneous conductance increases (in the proportional amplifier). There were only conductance increases in the smooth neurons.

For the feedforward model, the spontaneous firing frequency of the pyramidal and smooth cells is 0.046 ± 0.009 Hz and 8.2 ± 0.2 Hz; for the proportional amplifier model, 1.56 ± 0.02 Hz and 8.1 ± 0.1 Hz; for the hysteretic amplifier model, 0.126 ± 0.005 Hz for the pyramidal neurons, and the same as the other models for the smooth neurons. Because we wanted to obtain good direction selectivity down to low contrast and low velocities, the threshold of the pyramidal neurons was higher than that of the smooth neurons, which explains the lower spontaneous rate of the pyramidal cells.

2.6 Data analysis and special experiments

Standard electrophysiological methods were used for data analyses.

Contrast-Response and Velocity-Response Curves: Contrast-response curves were obtained from sine wave gratings moving in the preferred direction with optimum spatial and temporal frequency (1 c/deg and 1 Hz), repeated for 26 cycles. Velocity-response curves were obtained from 0.5^o wide bars moving in the preferred direction with high enough contrast to elicit a strong response (70% contrast), repeated 6 times with a half-second pause between each presentation. The response measure used was the peak response, computed from 8 $msec$ binwidth poststimulus time histograms (PSTHs). Usually PSTHs were summed over all neurons of one group (pyramidal or smooth) to generate a *compound* (average) PSTH. The compound peak firing rate was computed from the compound PSTH as the highest bin in the histogram.

Direction Index: The direction index (DI) was computed from the compound peak firing rate in the preferred direction, minus the peak spontaneous firing rate (P), and the compound peak firing rate in the nonpreferred direction, minus the

peak spontaneous firing rate (NP):

$$DI = 100(1 - NP/P)\%. \tag{2.5}$$

In other words $DI = 0$ corresponds to a cell that is not at all selective for the direction of motion while $DI = 100\%$ corresponds to a cell that does not fire at all in the cell's null direction. Since the spontaneous firing rate is substracted to obtain P and NP, DI may be larger than 100% if the peak firing rate in the nonpreferred direction is smaller than the peak spontaneous rate. In one case, DI was computed from the modulation of the intracellular potential induced by a periodic moving stimulus: in that case the response (P or NP) was the peak-to-peak amplitude of the modulation in mV instead of the peak firing rate.

The Mean Direction Index (MDI) is a velocity-averaged direction index. The average is weighted by the response P_i in the preferred direction (Orban, 1984):

$$MDI = \frac{\sum_{i=1}^{n} P_i DI_i}{\sum_{i=1}^{n} P_i}, \tag{2.6}$$

where n is the number of velocities for which the direction index has been computed.

Linearity Test: Ferster and his colleagues (Jagadeesh et al., 1993) carried out an elegant set of intracellular experiments in direction-selective simple cells. They showed that the (somatic) membrane potential signal evoked by a drifting sinusoidal grating can be predicted from the linear sum of responses to stationary contrast-reversal gratings at several spatial phases, seemingly implying a simple linear feedforward model of direction-selective simple cells.

The Jagadeesh *et al.* (1993) linearity test is based on expressing drifting sinusoidal gratings as sums of eight stationary contrast-reversal gratings at specific spatial and temporal phases. With ω the temporal frequency of the grating and k its spatial

frequency, simple trigonometry implies

$$sin(kx \pm \omega t) = \frac{1}{4} \sum_{n=0}^{7} sin(kx + n\frac{\pi}{8}) \cdot sin(\omega t + \frac{\pi}{2} \mp n\frac{\pi}{8}) . \qquad (2.7)$$

Let $R(x)$ denote the neuron's somatic membrane potential in response to a stimulus x. If the cell's response is linear, according to eq. 2.7, the response to a drifting grating can be predicted from responses to stationary gratings. The predicted response can be calculated from the equation:

$$\frac{1}{4} \sum_{n=0}^{7} R\left(sin(kx + n\frac{\pi}{8}) \cdot sin(\omega t + \frac{\pi}{2} \mp n\frac{\pi}{8})\right) . \qquad (2.8)$$

Linearity to superposition was assessed for the feedforward and cortical amplifier models by comparing the response predicted from stationary gratings to the actual response to drifting gratings.

Practically, fluctuations in somatic transmembrane potential of one neuron in the model evoked by drifting or stationary contrast-reversal sine gratings (spatial frequency 1 c/deg, temporal frequency 2 Hz) were measured by averaging the response to 57 cycles of the grating. Action potentials were removed from individual voltage traces with a median filter (identical to the one used by Jagadeesh et al., 1993) before averaging. These average potentials were used to perform the linearity test.

Input Conductance: We defined the somatic input conductance as the amplitude of a small hyperpolarizing current step (injected into the somatic compartment) divided by the resulting change in somatic membrane potential. In practice, we recorded the somatic membrane potential in one neuron during one particular simulation run (with a given visual stimulus). We then repeated the identical simulation (including the same random number seeds) in the presence of the constant current injection and calculated the somatic input conductance at each time from the difference in these

two voltage traces. Note that this measure is inaccurate during and immediately after action potentials, so that it could not be used in the preferred direction.

Blocking GABA: Blocking $GABA_A$ and $GABA_B$ inhibition to all or to one particular pyramidal neuron in the model is done by simply setting the corresponding weight to 0.

In one experiment, we blocked inhibition to only one pyramidal neuron in the model, and measured the direction selectivity index of that neuron before and after blockade. The experiment was repeated for every pyramidal neuron in the model; the results were presented as histograms of the distribution of the neurons' direction indices before and after blockade, mimicking an experiment in cat area 17 (Nelson et al., 1994). The stimulus was a standard bar (70% contrast and moving at $2^o/sec$) that was repeated 6 times, and the response measure was the average number of spikes produced by a neuron while the stimulus is in the neuron's receptive field, corrected for the mean spontaneous rate. While blocking inhibition in a given cell, a constant hyperpolarizing current was injected into the cell to bring spontaneous firing down to values close to the unblocked case. The same manipulation was performed by (Nelson et al., 1994) to ensure that the neuron's threshold was not changed by blocking inhibition.

2.7 Computer implementation

The simulations were carried out on SPARC 2 and 10 UNIX-based workstations. The program, written in C, was developed by H.S. as part of his Ph.D. thesis. The associated differential equations were numerically solved using the exponential method (Wilson and Bower, 1989) with a variable timestep (Press et al., 1992). The shortest time constant in the system was 0.05 $msec$, the activation time constant of the tran-

sient sodium current. The minimum timestep for solving the differential equations was set to 0.01 *msec*. On a SPARCstation 10, our program simulated 1 *sec* of the proportional amplifier model (with 50 cortical neurons) output for a moving bar in about 404 *sec*, not counting the time to simulate the visual input and LGN model output. The simulation time was approximately linear in the number of neurons, so that for the hysteretic amplifier the simulation time was approximately 16 times longer. For instance, producing Fig. 5.7 (see Chapter 6) required about two weeks of SPARCstation 10 CPU time.

2.8 Summary

We model events occuring in a small network of neurons located in the primary visual cortex of the adult cat. The cortical network comprises 40 and 640 pyramidal (excitatory) and 10 and 160 smoooth (inhibitory) neurons for the proportional and hysteretic amplifiers, respectively. The basic architecture of the cortical amplifier model is shown in Fig. 2.3. Both proportional and hysteretic amplifiers are similar except for the values of some parameters. The feedforward model is similar except that there are no connections between the pyramidal neurons.

Visual input to the cortical network is provided by a one-dimensional retino-geniculate module, transforming the grating stimulus into a series of spikes mimicking the output of the geniculate relay cells (Victor, 1987). Spatially, the centers of the LGN neurons' receptive fields are positioned at one of six spatial locations which occur at 5′ intervals (Wörgötter and Koch, 1991). Pyramidal neurons in cortex receive input from the first 5 groups of LGN neurons, and smooth neurons receive input from the last 5 groups of LGN neurons (see Fig. 2.3). Overall, there is a spatial offset of 5′ between input fields of pyramidal and smooth neurons, providing the asymmetry necessary for direction selectivity.

The cellular model takes into account the known morphology and biophysics of visual cortical neurons. In particular, our cells respond to synaptic input with a stream of discrete all-or-none action potentials, rather than with a continuous firing rate as in the vast majority of neural network models. Anatomical dimensions of a representative layer 5 pyramidal neuron and a smooth (basket) cell were obtained by reconstructing suitable cortical neurons that had been labelled intracellularly with horseradish peroxidase during *in vivo* experiments in the anesthetized, adult cat (Douglas et al., 1991). The 3-D coordinates and diameters of the dendritic arbor and soma yielded a model with many compartments that was reduced to either three or four compartments (Douglas and Martin, 1991; Bush and Sejnowski, 1993; Bernander, 1993). Each compartment contains a number of membrane currents, including synaptic conductance changes. The somatic compartment has Hodgkin-Huxley like channels that produce action potentials in response to current injection.

Each cortical connection drawn in Fig. 2.3 symbolizes synapses of equal strength from each neuron of one group to all neurons of the other group. In particular, pyramids excite each other, and smooth cells inhibit pyramids and each other. In the current version of the model, we did not include excitatory connections from pyramids to smooth cells. Excitation is of the non-NMDA or AMPA variety. Inhibition is of two types, $GABA_A$, or transient, and $GABA_B$, or sustained inhibition. The amplitudes of synaptic conductances and time constants that govern their behavior have yet to be determined experimentally in detail for pyramidal and spiny stellate cells in primary visual cortex. However, estimates from the literature were used to constrain our model.

Chapter 3

A simplified theory of cortical amplification, and the proportional and hysteretic amplifiers

3.1 Introduction

The detailed biophysically-based cortical amplifier model is not analytically tractable, because it is based on a high dimensional system of coupled, nonlinear partial differential equations. Nevertheless, it is possible to gain some qualitative insight into the cortical amplifier model's behavior through analysis of reduced models (see also Douglas et al., 1994b). In this chapter, we discuss simplified cortical amplifier models, by introducing functions that characterize the equilibrium response of the detailed neuron model, and linearizing these functions; we use these simplifications to solve for the cortical network's firing.

As introduced in Chapter 1, the cortical amplifier model is a circuit that amplifies the geniculate input to cortex in the preferred direction, through excitatory intracortical connections, and cancels geniculate excitation in the null direction through inhibition. We refer you to that chapter for the context of the results presented here.

The detailed model itself and the simulation methods are described in Chapter 2. We describe there the geniculate model we used to provide input to cortex. We refer you to that chapter for these explanations.

This chapter is about a simplified theory of the operation of the cortical amplifier, and the two possible amplification modes, depending on the strength of positive feedback. Both modes were explored using detailed modeling. We have introduced the parameters and architecture for both models in Chapter 2. The detailed model in the first mode is called the proportional amplifier model and its response properties are explored in detail in Chapter 4; the other mode, the hysteretic amplifier, is dealt with in Chapter 5. In this chapter, we explain the fundamental theoretical differences between these models, both in their equilibrium responses and dynamics.

A simplified theory of amplification in cortex at equilibrium is introduced in Section 3.2, and the functions that characterize equilibrium behavior are defined and given, for the proportional amplifier only. Section 3.3 explains the fundamental, defining difference between proportional and hysteretic amplifiers. Section 3.4 gives for the hysteretic amplifier the functions that characterize equilibrium response. Section 3.5 derives a simplified equation for the network dynamics by using a linear approximation for the characterizing functions. We will use this equation in Sections 4.5 and 5.6. Section 3.6 gives an equation for the dynamics that is valid even in the presence of nonlinearities in the functions that characterize equilibrium behavior, and gives us some intuition into the influence of nonlinearities on the network dynamics. In the last section of the chapter, Section 3.7, we present a simplified nonlinear dynamical model that gets input from the same LGN model as the detailed model. We name

this model, somewhat whimsically, DYNAMO.

3.2 Neuronal responses at equilibrium and the proportional amplifier

In the present section, we introduce functions that characterize the equilibrium response of the detailed neuron model, and by linearizing these functions we solve for the cortical network's firing. This section is only about the proportional amplifier, one of the parameter conditions of the detailed model (see Section 2.5). The corresponding characterization at equilibrium for the hysteretic amplifier is in Section 3.4.

When a constant current is injected into the soma of a single pyramidal cell, the neuron responds with a stream of action potentials. The relationship between the current's amplitude I and the resulting spiking frequency F is known as the current-discharge curve $\mathbf{F} = \mathbf{F_i(I)}$. Initially during stimulation, this curve is steep. However, due to accumulation of calcium and resulting activation of a calcium-dependent potassium current (adaptation), the slope is later much reduced. The time constant of this adaptation is $15 - 50$ $msec$ (Ahmed et al., 1995). The unadapted and adapted current-discharge relations of a typical model pyramidal cell are shown in Fig. 3.1a. The slope of the adapted curve is 112 Hz/nA for the first nA of input currents. The F_i function is not strictly linear because of refractoriness and other nonlinearities, but for the qualitative purposes of the following discussion, the F_i curve can be considered linear. For the moment, let us ignore adaptation. We will see later, however, that adaptation is important for fully understanding the dynamics of the network (see Sections 4.5 and 4.8).

At the heart of the Canonical Microcircuit is massive, recurrent excitatory feedback, characterized by $\mathbf{I_{rec}}$, the function relating the input frequency of all excitatory,

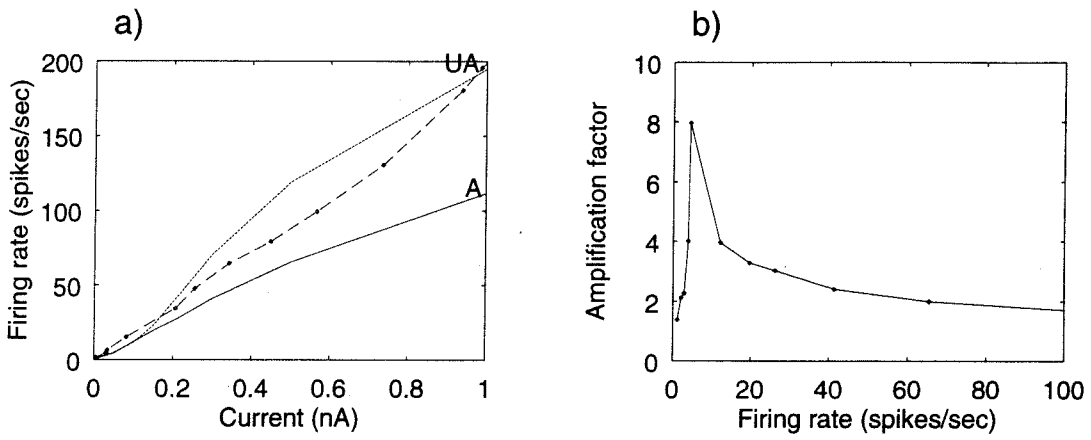

Figure 3.1: **Steady-state relationships in the proportional amplifier.** We illustrate here a number of steady-state relationships for pyramidal neurons in the proportional amplifier model, obtained by injecting constant current pulses into the pyramidal neurons only (in the absence of inhibition or geniculate input). Panels (a) and (b) are concerned with single-cell properties, and panels (c) and (d) describe attributes of the whole network. **(a)** I_{rec} (dashed line), and the adapted (A) and unadapted (UA) current-discharge curves $F_i(I)$. All curves have been shifted, with zero current corresponding to the current threshold (rheobase). **(b)** Pyramidal output firing rate as a function of the input firing rate ($F(f)$ of eq. 3.1; dashed line), as compared against a line of slope one. **(c)** The cortical amplifier's maintained firing rate as a function of the sustained input current injected into all pyramidal neurons. **(d)** The cortical amplifier's firing rate gain, defined as the ratio of the pyramids maintained firing rate in the cortical amplifier to the pyramidal cell's firing rate f in the absence of any recurrent connections, as a function of f. Note that amplification is much larger at low input values.

cortico-cortical synaptic inputs to a pyramidal cell (all assumed to fire at the same, constant frequency) to the maintained current flowing from these synapses into the soma. I_{rec} is estimated indirectly: a certain constant current is injected into the soma of all pyramidal neurons connected in the cortical amplifier configuration (in the absence of any inhibition), and their maintained firing rate is noted. The total current producing that firing rate is estimated from the adapted current-discharge curve, and the injected current is substracted from the total current to yield the contribution from recurrent excitatory connections. It is sometimes more convenient to display the inverse of I_{rec} (Fig. 3.1a).

The adapted F_i and I_{rec} can be used to compute the maintained output firing rate $F(f)$ in the pyramidal neurons that will result from activating the excitatory cortico-cortical synapses at a given input rate f, in the absence of inhibitory or geniculate input (a single-cell function; Fig. 3.1b):

$$F(f) = F_i(I_{rec}(f)) . \tag{3.1}$$

Operationally, this current is obtained by clamping the presynaptic firing frequency of all cortico-cortical fibers at f and then computing the resulting discharge rate of the pyramidal cells (in the absence of any further feedback).

We can use these relationships to estimate the discharge frequency of the pyramidal cells at equilibrium. It is defined implicitely by the requirement that the current-discharge curve, applied to the sum of the input current I_{in} (delivered to all pyramidal neurons either by the LGN or via an intracellular electrode) and the recurrent current must be equal to the discharge frequency. In other words, the discharge rate f must satisfy (see also Fig. 3.3):

$$f = F_i(I_{in} + I_{rec}(f)) . \tag{3.2}$$

This equation is difficult to solve analytically because of the nonlinearities present

in F_i and I_{rec}. However, it can be solved if F_i and I_{rec} are linearized as in:

$$F_i(I) = k_{F_i}(I - I_T)\,, \qquad I_T : \text{threshold} \tag{3.3}$$

and

$$I_{rec}(f) = k_{rec} f\,. \tag{3.4}$$

From eq. 3.2, the pyramidal neuron discharge rate at equilibrium is now:

$$f = \frac{k_{F_i}}{1-\alpha}(I_{in} - I_T)\,, \tag{3.5}$$

where $\alpha = k_{F_i} k_{rec}$ is the slope of $F(f)$. Since the firing frequency must be positive, we must have $\alpha < 1$ for this equation to be valid. As we can see from Fig. 3.1b, this condition is satisfied for the proportional amplifier model. Linearization implies that the steady-state firing rate is linear in the input current. As witnessed by Fig. 3.1c, this holds only approximately.

Another important steady-state function is the **firing rate gain G(f)**. It is given by the pyramidal neuron's maintained firing rate for the cortical amplifier divided by the pyramid firing rate in the absence of any excitatory cortico-cortical connections and is expressed as a function of firing rate in the absence of excitatory cortico-cortical connections f. $G(f)$ measures the effectiveness of the recurrent connections in driving the pyramidal neurons, relative to the LGN input.

In the linear approximation, the firing frequency in the absence of recurrent connections is given by replacing I by I_{in} in eq. 3.3, resulting in a firing rate gain:

$$G(f) = \frac{1}{1-\alpha}\,. \tag{3.6}$$

As α increases from 0, G increases, eventually diverging as $\alpha \to 1$.

The cortical amplifier's behavior is qualitatively similar, although its gain is not independent of the input current (Fig. 3.1d). At low firing rates, $G(f)$ is large, because the slope of $F(f)$ is very close to 1 (see Fig. 3.1b), but for larger inputs the slope of $F(f)$ decreases and so does the gain of the cortical amplifier model (recall that α is the average slope of $F(f)$). This variation in gain can be traced to saturation in the F_i curve as well as in I_{rec}, which originate for our model in the biophysics of spike production by Hodgkin and Huxley-like currents, as well as saturation of the excitatory driving potential in dendritic compartments. So the name "proportional amplifier" is, in part only, a misnomer. But we will see in Section 3.4 that the hysteretic amplifier is much more nonlinear; in comparison, the proportional amplifier amplifies rather linearly. But especially, the contrast-response curve of the proportional amplifier model is quite linear at low contrasts (see Section 4.3).

Since $F(f)$ arises from the combination of the F_i and I_{rec} curves, $G(f)$ can be increased by adjusting the slope of $F(f)$ to be close to 1 by changing the slope of either one of these. Increasing the excitatory cortico-cortical connection weight will increase the slope of the I_{rec} curve and so also the slope of $F(f)$.

We conclude that the proportional amplifier's action on steady stimuli is moderately nonlinear amplification, which can be roughly approximated by linear, proportional amplification.

3.3 Proportional and hysteretic amplifiers

Despite strong positive feedback in the network, the proportional amplifier described in the previous section has no trouble turning off once the LGN input returns to the resting level. The explanation lies in eq. 3.5. As long as the input current is smaller than the neuron's threshold, the pyramidal neurons do not fire.

However, in the other parameter condition described in Section 2.5, called the hys-

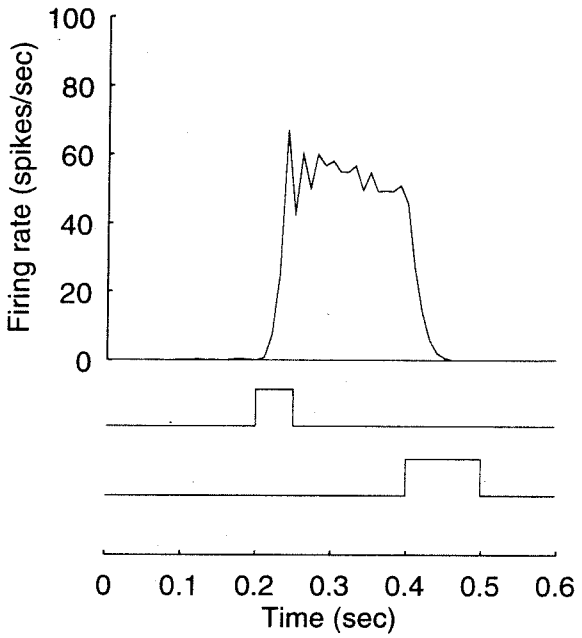

Figure 3.2: **Hysteresis in the hysteretic amplifier.** PST histogram of pyramidal neurons in the hysteretic amplifier model in response to the injection of two consecutive pulses of current (shown below the PSTH). The first pulse (upper pulse) was injected at time $t = 200$ *msec* in all pyramidal neurons, while the second pulse (lower pulse) was injected in the smooth cells at time $t = 400$ *msec*. Discharge persists in the pyramidal neurons after the initiating pulse has been withdrawn, meaning that hysteresis is present in the system. However, inhibition resulting from the activation of the smooth cells by the second pulse resets the network to its initial silent state.

teretic amplifier model, the situation is different, as shown in Fig. 3.2. The stimulus used in this case is injection of a pulse of current in all pyramidal neurons, followed by the delayed injection of a second pulse in all smooth neurons; we plot a PST histogram of the response of pyramidal neurons in the model. Surprisingly, model neurons do not stop discharging at the end of initial pulse, and fire instead in the absence of any stimulus until reset by the pulse injected into the smooth neurons. In other words, the model shows *hysteresis.*

This phenomenon can be understood graphically by looking at Fig. 3.3. The upper panel shows that the steady-state pyramidal neuron firing rate is the firing rate for which the horizontal separation between the two curves I_{rec} and F_i is equal to I_{in} (a graphical interpretation of eq. 3.2). For zero input, the equilibrium firing or attractor is 0 Hz, since that is the firing for which the two curves cross. So the network turns off without input. The condition depicted in this panel is similar to the situation in the proportional amplifier model (Fig. 3.1a): the initial slope of I_{rec} is larger than that of F_i: $\frac{1}{k_{rec}} > k_{F_i}$. If the converse is true, we obtain the situation depicted in Fig. 3.3b. There are now three crossing points. Although there is still an attractor at 0 Hz as long as the threshold is nonzero (since the curves still cross there), in addition there is an attractor for zero input corresponding to the firing rate at the upper crossing of the two curves; the middle crossing point is not stable. Therefore, the system of Panel b can fire without any input. In Fig. 3.4a, we will see that the cortical amplifier model operates in the mode of Fig. 3.3b. This explains that the model can fire without any input as in Fig. 3.2. However, in most conditions the model does not fire in the absence of any input, for instance for bar stimuli. We will explain this behavior later (see Section 5.6).

We now show that the hysteretic amplifier's equilibrium relationships are indeed as in Fig. 3.3b.

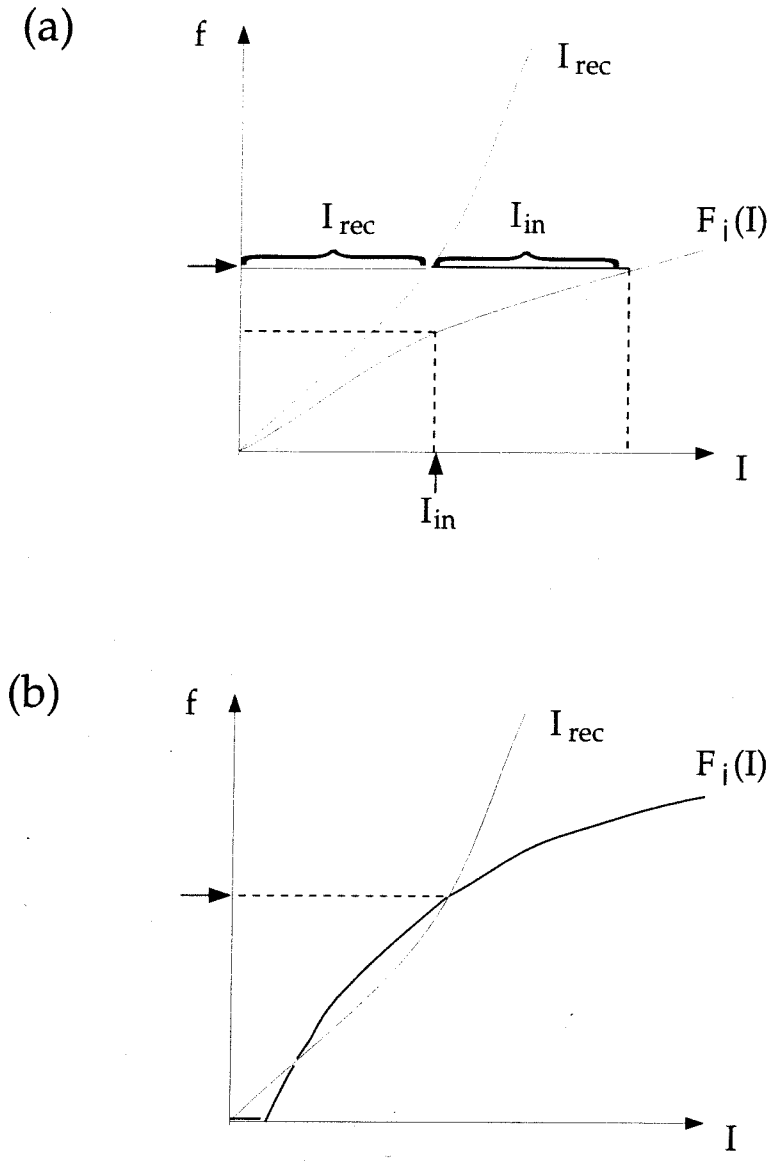

Figure 3.3: **Determining the steady-state discharge frequency.** We represent here schematically the relations that determine the steady-state discharge frequency of pyramidal neurons in the cortical amplifier model. **(a)** For a given input current I_{in} (vertical arrow), steady-state occurs at the firing rate (horizontal arrow) for which the horizontal separation between the two curves I_{rec} and F_i is equal to I_{in}. In the absence of excitatory feedback, the firing rate is lower (follow the vertical arrow up to the f axis). **(b)** A steeper F_i will intersect I_{rec}. In that case, sustained discharge in the absence of any input is possible, at the firing rate indicated by the horizontal arrow. In particular, even if the network initially does not fire, any small input will cause it to reach that high sustained firing rate; even if the input is then withdrawn, it will maintain the high discharge frequency (hysteretic mode).

3.4 Hysteretic amplifier at equilibrium

In this section, we describe the steady-state functions of the hysteretic amplifier model. These functions were already defined in Section 3.2. The unadapted and adapted current-discharge relations F_i of a typical model pyramidal cell are shown in Fig. 3.4a, together with the recurrent current function I_{rec}. We note that the initial slope of F_i is larger than that of I_{rec} (in the linear approximation, $\frac{1}{k_{rec}} < k_{F_i}$), as in Fig. 3.3b, reflecting the fundamental difference between proportional and hysteretic amplifier models. This corresponds in the network's steady-state transfer function $F(f)$ to an initial slope that is larger than one (Fig. 3.4b): in the linear approximation, $\alpha > 1$.

For simplicity, we define the threshold current of the neuron's f-I curve as "zero" input current for all these characteristics.

Injecting a constant current into all pyramidal neurons in the model and plotting the resulting firing rate at steady-state results in the equilibrium response function shown in Fig. 3.4c, that is related to I_{rec} and F_i by eq. 3.2. Since there is an attractor at a high firing rate, the network will reach that firing rate for even a small suprathreshold input (note that the thresholds are normalized to 0 in Fig. 3.4). When increasing the input current further, the firing rate rises rather slowly, because of compressive nonlinearities in both I_{rec} and $F(f)$. The response is much more nonlinear than for the proportional amplifier (Section 3.2).

The gain function is plotted in Fig. 3.4. The amplification is subtantial, especially at low inputs; for very small inputs, the amplification becomes extremely large, because of the large response to any small current injection that nudges the system to the high firing attractor (see Section 5.6 for a more detailed explanation of the hysteretic amplifier's responses to the injection of current pulses).

We conclude that the hysteretic amplifier's action on steady stimuli is character-

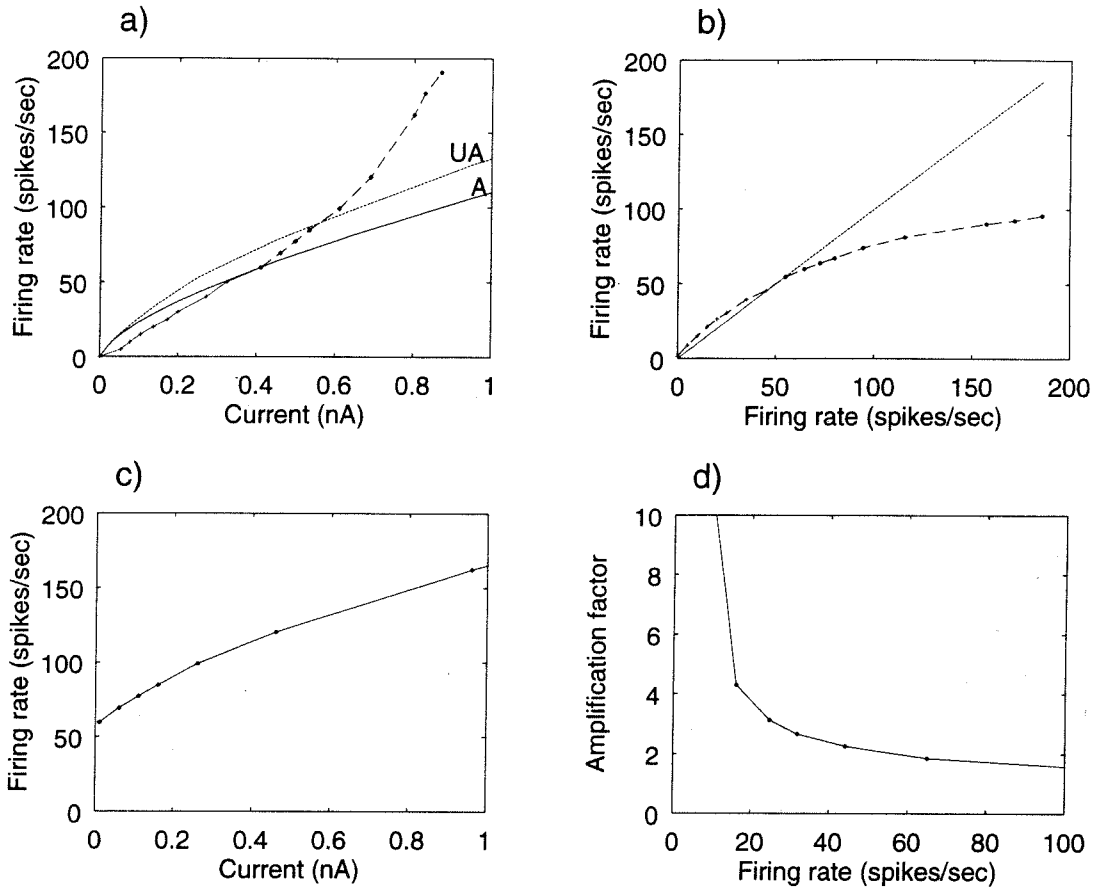

Figure 3.4: **Steady-state relationships in the hysteretic amplifier.** We illustrate here a number of steady-state relationships for pyramidal neurons in the hysteretic amplifier model, obtained by injecting constant current pulses into the pyramidal neurons only (in the absence of inhibition or geniculate input). Panels (a) and (b) are concerned with single-cell properties, and panels (c) and (d) describe attributes of the whole network. **(a)** I_{rec} (dashed line), and the adapted (A) and unadapted (UA) current-discharge curves $F_i(I)$. All curves have been shifted, with zero current corresponding to the current threshold (rheobase). **(b)** Pyramidal output firing rate as a function of the input firing rate ($F(f)$ of eq. 3.1; dashed line), as compared against a line of slope one. **(c)** The cortical amplifier's maintained firing rate as a function of the sustained input current injected into all pyramidal neurons. **(d)** The cortical amplifier's firing rate gain, defined as the ratio of the pyramids maintained firing rate in the cortical amplifier to the pyramidal cell's firing rate f in the absence of any recurrent connections, as a function of f.

ized by highly nonlinear amplification.

3.5 A linear neuronal dynamical equation

Moving stimuli are not steady stimuli, and the cortical amplifier model will generally not reach equilibrium firing when responding to them. Therefore, it is important to understand the dynamics of the cortical amplifier model to predict how much amplification can be achieved under these conditions.

In this section, we derive a simplified equation for the network dynamics by using a linear approximation for the characterizing functions F_i and I_{rec}. We will use this equation in Sections 4.5 and 5.6.

We can write the firing rate of the pyramidal neurons as:

$$f = F_i(I_{in} + I_{rec}(f)) . \tag{3.7}$$

Although I_{rec} was considered a static, equilibrium function earlier, it can be generalized into a filter that gives the time-varying synaptic current for a given time-varying pyramidal neuron firing rate. Its transfer function is then mainly that of the synapse.

Expression for I_{rec} The postsynaptic conductance at the synapse between pyramidal neurons, $G_{pp}(t)$ (pp stands for pyramidal to pyramidal), for an arbitrary presynaptic firing rate function $f(t)$, is a scaling constant g_{pp} times the elementary synaptic function G^0_{pp} convolved with the presynaptic firing rate function $f(t)$:

$$G_{pp}(t) = g_{pp} G^0_{pp} * f(t) . \tag{3.8}$$

We have the following expression for the elementary synaptic function between pyramidal neurons (see Section 2.5):

$$G^0_{pp} = \frac{1}{\tau_{syn}} e^{-t/\tau_{syn}}, \tag{3.9}$$

with $\tau_{syn} = 20\ msec.$ Making the simplifying assumption that the compartmental voltages are constant, and that current flowing through the synapses propagates instantaneously to the soma, the postsynaptic current, I_{rec}, is proportional to the postsynaptic conductance, so it can be written using a similar formula but changing the scaling constant g_{pp}. It turns out that this scaling constant is k_{rec} from eq. 3.4:

$$I_{rec}(t) = k_{rec} G^0_{pp} * f(t)\,. \tag{3.10}$$

Expression for I_{in} We now seek an expression for I_{in}, which lumps all current inputs that do not come from the pyramids. Potentially, it arises from two sources, one excitatory, the other inhibitory: the LGN and the smooth cells. We will make another simplifying assumption: that the elementary synaptic function of both inhibition and LGN input are the same as G^0_{pp}. We can then write a similar expression to eq. 3.10:

$$I_{in}(t) = w_{lp} G^0_{pp} * f_l(t) - w_{ip} G^0_{pp} * f_i(t)\,, \tag{3.11}$$

where the weight of the connection and firing rates are w_{lp} and $f_l(t)$, and w_{ip} and $f_i(t)$ for the LGN neurons and smooth neurons, respectively (lp stands for LGN to pyramidal, and ip for inhibitory to pyramidal). The terms $w_{lp} f_l(t)$ and $w_{ip} f_i(t)$ have the dimension of currents, and so we will name them LGN and inhibitory currents respectively (I_l and I_i). Note, however, that they are not exactly the currents injected,

because they are just scaled copies of the firing rates. So we now have the equation:

$$I_{in}(t) = G^0_{pp} * (I_l(t) - I_i(t)) . \tag{3.12}$$

Integral and differential equations Going back to eq. 3.7, we linearize F_i as in eq. 3.3, and we now have a linear integral equation for the dynamics of the network:

$$f(t) = k_{F_i} G^0_{pp} * (I_l(t) - I_i(t) - I_T + \alpha f(t)) , \tag{3.13}$$

where we substituted α from eq. 3.5. We can transform this equation into a differential equation. Assuming that the initial conditions are rest ($f(t) = 0$, $-\infty < t \leq 0$), we will show that the differential equation corresponding to eq. 3.13 is:

$$\tau_{syn} \frac{df}{dt} = -f + \alpha f + k_{F_i}(I_l - I_i - I_T) . \tag{3.14}$$

To show that, we first multiply Equation 3.14 by $(1/\tau_{syn})e^{t/\tau_{syn}}$:

$$e^{t/\tau_{syn}} \frac{df}{dt} = -\frac{1}{\tau_{syn})} e^{t/\tau_{syn}} f + \frac{1}{\tau_{syn}} e^{t/\tau_{syn}} (\alpha f + k_{F_i}(I_l - I_i - I_T)) . \tag{3.15}$$

Rearranging this equation we get:

$$\frac{d}{dt}(e^{t/\tau_{syn}} f) = \frac{1}{\tau_{syn}} e^{t/\tau_{syn}} (\alpha f + k_{F_i}(I_l - I_i - I_T)) . \tag{3.16}$$

Integrating from 0 to T we get:

$$e^{T/\tau_{syn}} f(T) = \int_0^T \frac{1}{\tau_{syn}} e^{t/\tau_{syn}} (\alpha f + k_{F_i}(I_l - I_i - I_T)) dt . \tag{3.17}$$

Rearranging this equation we get:

$$f(T) = \int_0^T \frac{1}{\tau_{syn}} e^{-(T-t)/\tau_{syn}} (\alpha f + k_{F_i}(I_l - I_i - I_T))dt\,. \tag{3.18}$$

That is exactly Equation 3.13. Equation 3.14 is a simplified description of the dynamics of the cortical amplifier model.

Proportional amplifier case For the proportional amplifier, $\alpha < 1$ (see Section 3.2). We can rewrite eq. 3.14 as:

$$\frac{\tau_{syn}}{1-\alpha}\frac{df}{dt} = -f + \frac{k_{F_i}}{1-\alpha}(I_l - I_i - I_T)\,. \tag{3.19}$$

This equation describes a linear system with an impulse response of:

$$e^{-t/\frac{\tau_{syn}}{1-\alpha}} \tag{3.20}$$

The pyramid firing rate f settles to steady-state with a certain time constant, the network's time constant $\tau_{net} = \tau_{syn}/(1-\alpha)$. In conditions where there is amplification of the input, *i.e.,* when α is slightly smaller than 1, the network's time constant becomes much larger than τ_{syn}. We will use this equation in Section 4.5.

Hysteretic amplifier case For the hysteretic amplifier, $\alpha > 1$ (see Section 3.4). We can rewrite eq. 3.14 as:

$$\frac{\tau_{syn}}{\alpha-1}\frac{df}{dt} = f + \frac{k_{F_i}}{\alpha-1}(I_l - I_i - I_T)\,. \tag{3.21}$$

This equation describes a linear system with an impulse response of:

$$e^{t/\frac{\tau_{syn}}{\alpha-1}} \tag{3.22}$$

The pyramid firing rate f increases (or decreases, depending on the sign of $I_l - I_i - I_T$) exponentially with a certain time constant, the network's time constant $\tau_{net} = \tau_{syn}/(\alpha - 1)$. When α is only slightly larger than 1, the network's time constant becomes much larger than τ_{syn}. We will use this equation in Section 5.6.

3.6 A simplified nonlinear neuronal dynamical equation

an implicit equation for the dynamics of the nonlinear case In this section, we will try to understand how the nonlinear shape of the $F(f)$ changes the speed of the dynamics of the detailed model.

Starting from the equations:

$$f = F_i(I_{tot}) \tag{3.23}$$

where: F_i is f-I curve and I_{tot} is the total input current to the neuron. The current in steady-state is (valid only approximately: conductances interact nonlinearly):

$$I_{tot} = I_{rec}(f) + I_{l,i} \tag{3.24}$$

I_{rec}: current from the excitatory p-p connections; $I_{l,i}$: sum of LGN and smooth neuron current. This equation should hold also dynamically (note that $G^0_{pp}(t)$ - see Equation 3.9 - is a normalized function, such that $G^0_{pp} * f_0 = f_0$ where f_0 is a constant):

$$I_{tot} = I_{rec}(G^0_{pp} * f) + I_{l,i}(t) \tag{3.25}$$

By expanding I_{rec} to the first term of its Taylor series around $G^0_{pp} * f$ (derivative k_{rec}), one can see that the following equation is approximately equivalent to the previous

one:

$$I_{tot} = I_{rec}(G^0_{pp} * f + \frac{I_{l,i}(t)}{k_{rec}}) \tag{3.26}$$

Now, we take $\hat{I}_{l,i}(t)$ such that:

$$(G^0_{pp} * \hat{I}_{l,i})(t) = I_{l,i}(t) \tag{3.27}$$

This deconvolution can be done in the Fourier domain:

$$\hat{I}_{l,i}(\omega) = \tau_{syn}(\frac{1}{\tau_{syn}} + j\omega)I_{l,i}(\omega) \tag{3.28}$$

where $\hat{I}_{l,i}(\omega)$ is the Fourier transform of $\hat{I}_{l,i}(t)$, $I_{l,i}(\omega)$ is the Fourier transform of $I_{l,i}(t)$, and $1/(\tau_{syn}(1/\tau_{syn} + j\omega))$ is the Fourier transform of G^0_{pp}. Using the newly defined $\hat{I}_{l,i}(t)$ we get:

$$I_{tot} = I_{rec}(G^0_{pp} * (f + \frac{\hat{I}_{l,i}(t)}{k_{rec}})) \tag{3.29}$$

Since $F(f) = F_i(I_{rec}(f))$ we get:

$$f = F(G^0_{pp} * (f + \frac{\hat{I}_{l,i}(t)}{k_{rec}})) \tag{3.30}$$

Or:

$$F^{-1}(f) = G^0_{pp} * (f + \frac{\hat{I}_{l,i}(t)}{k_{rec}}) \tag{3.31}$$

As before (see equation 3.13) the corresponding differential equation is:

$$\tau_{syn}\frac{dF^{-1}(f)}{dt} = -F^{-1}(f) + f + \frac{\hat{I}_{l,i}(t)}{k_{rec}} \tag{3.32}$$

This equation can be transformed into an integral equation by integrating on both sides, from time 0, for which the system is assumed to be at rest (f=0), to time T,

which is an arbitrary time for which we would like to know the firing rate $f(T)$:

$$\int_0^T \frac{dF^{-1}(f)}{dt}dt = \frac{1}{\tau_{syn}}\int_0^T (f - (F^{-1}(f) - \frac{\hat{I}_{l,i}(t)}{k_{rec}}))dt \tag{3.33}$$

Since

$$\int_0^T \frac{dF^{-1}(f)}{dt}dt = F^{-1}(f(T)) - F^{-1}(0) \tag{3.34}$$

and if we define $F^{-1}(0)$ as f_{thr}, the firing rate threshold of the $F(f)$ curve, we can write the final equation as:

$$f(T) = F\left[f_{thr} + \frac{1}{\tau_{syn}}\int_0^T (f - (F^{-1}(f) - \frac{\hat{I}_{l,i}(t)}{k_{rec}}))dt\right] \tag{3.35}$$

f_{thr}: threshold of the $F(f)$; $F(f) = F_i(I_{rec})$

interpretation: area between f and $F(f)$ This equation gives us an understanding of the influence of the shape of $F(f)$ and the amount of input on the dynamics. We assume here that the initial slope of $F(f)$ is larger than 1, so that we are in the hysteretic amplifier case. The term:

$$f - (F^{-1}(f) - \frac{\hat{I}_{l,i}(t)}{k_{rec}}) \tag{3.36}$$

in Equation 3.35, is the distance between $f = f$ (line of slope 1) and the $F(f)$ curve translated by the amount of input. So the equation giving the firing reached is ($F(f)$ of) the $F(f)$ threshold plus the area between $f = f$ (line of slope 1) and the $F(f)$ curve translated by the amount of input, integrated over time. So the larger that area, the faster the dynamics. In particular, if the $F(f)$ is very concave (very steep initially then flattens out), the dynamics are faster than if the $F(f)$ is rather straight.

3.7 A simplified nonlinear dynamical model: halfway to the detailed models

This section describes a simple nonlinear dynamical model that reproduces many of the properties of the detailed models, and has been used extensively in this research project to gain insights into the canonical microcircuit's properties. We call this model DYNAMO (DYNAmical MOdel).

In this model, the detailed models are reduced to simulating only two "neurons," one pyramidal neuron and one smooth cell. The output of each simplified neuron is firing rate instead of spikes as in the detailed model, and represents the average firing rate of the corresponding neuron population in the detailed models. Input to the model is provided by the same LGN model as in the detailed models, but generation of Poisson spikes is turned off. Synapses in this model are implemented using the same transfer functions as in the detailed model, but the input to the synapses is firing rate instead of sums of spikes. From the resulting conductance change, an input current can be calculated using a lookup table for either the voltages in the compartments of the detailed model or the recurrent current function I_{rec}. Inhibitory current is calculated independently from excitatory current and assumed to sum linearly with excitation. From the total current calculated in this way, the firing rate is calculated using a lookup table for the current-discharge curve of the detailed model.

Other features of this model are as follows:

- the presence of the membrane and the membrane time constant of the detailed model are not mimicked in this model; these are rather minor determinants of the network model's dynamical behavior
- the presence of adaptation and the resulting variations in the f-I curve with time are not mimicked either.

We now describe the DYNAMO model neuron for the special case of one type of synaptic input. We will assume that this one synapse corresponds to the synapse from the neuron onto itself. In the full DYNAMO model, there are also synapses from the LGN and smooth neurons, implemented using the same synaptic filters as in the detailed models. Again, it is assumed that currents produced by the synapses sum linearly.

The DYNAMO model consists of a series of differential equations, equations and tables. The output from the DYNAMO model is produced by solving these equations in discrete time, as when solving a differential equation.

We start from the equations:

$$f = F_i(I_{tot}) \tag{3.37}$$

f: firing of the DYNAMO model neuron; F_i: f-I curve; I_{tot}: total input current to the neuron. The f-I curve from the detailed compartmental model is incorporated directly in the DYNAMO model to calculate its output firing rate at the current timestep. We can measure the f-I curve of the detailed compartmental model as a series of current-firing pairs of numbers. Keeping these in a table, we can interpolate linearly between them to get the firing for any input current. We will now describe how to obtain I_{tot} for DYNAMO.

In this simplified case, the total current to the neuron is just the synaptic current from the one synapse, the recurrent pyramidal synapse:

$$I_{tot} = I_{rec}(f, t) \tag{3.38}$$

I_{rec}: current from the connection of the DYNAMO model neuron to itself. The form of I_{rec} is:

$$I_{rec}(f, t) = G_{pp}(f, t)(V - E_{rev}) \tag{3.39}$$

G_{pp}: postsynaptic conductance for the synapse from the DYNAMO model neuron to itself; V: voltage of the DYNAMO model neuron; E_{rev}: reversal potential of the synapse. The reversal potential of the synapse is the same as in the detailed compartmental model. In general, I_{tot} is a nonlinear function. This equation can be calculated in two different ways. The functional form of $I_{rec}(f)$ for constant f has been measured for the detailed model. $G_{pp}(f,t)$ reduces to f for time-independent f. We can assume that the entire time-dependency of I_{rec} is in G_{pp}, calculate G_{pp} at each timestep, and find I_{rec} by using the steady recurrent function measured previously as a lookup table and the current value of G_{pp} as the f value in this lookup table.

An alternative way is to compute a voltage substitute in DYNAMO, using another lookup table. In the compartmental neuron, the average voltage in any compartment varies with firing rate quite a lot, because of the presence of the spiking. The higher the firing rate, the higher the voltage because each spiking event increases the average potential. It is important to take into account this voltage variation with firing rate, since it affects the amount of current flowing through the synapses. The voltage of the DYNAMO model neuron allows us to take into account that voltage variation with firing rate. We can measure the average voltage in any compartment from the detailed compartmental model as a series of voltage-firing rate pairs of numbers. Keeping these in a table, we can interpolate linearly between them to get the average voltage for any input firing rate. The procedure is then to use the firing rate calculated at the previous timestep for the DYNAMO model to calculate the model's voltage at the current timestep! We assume of course that the timestep is small enough so that the firing rate is not varying very much.

The last remaining variable that needs to be calculated is G_{pp}. It is calculated exactly as in the detailed model.

The postsynaptic conductance G_{pp}, for an arbitrary presynaptic firing rate function $f(t)$, is a scaling constant g_{pp} times the elementary synaptic function G^0_{pp} con-

volved with the DYNAMO model neuron firing rate $f(t)$:

$$G_{pp} = g_{pp} G^0_{pp} * f(t) \tag{3.40}$$

$f(t)$: firing rate of the DYNAMO model neuron as a function of time. g_{pp}: synaptic weight.

That concludes the description of the DYNAMO model. We will use this model in Section 7.3.2.

3.8 Summary

We have shown that amplification at equilibrium in the cortical amplifier model can be analyzed and understood through a series of steady-state characterizing functions. This analysis allowed us to pinpoint the difference between proportional and hysteretic amplifier models. Historically, in the course of this research project, these functions have been crucial for the design of the proportional amplifier model.

We have also developed simplified, linear differental equations for the dynamics of the models, which appear to show that the hysteretic and proportional amplifier models are very different. These equations will be important to understand the responses of the models to transient stimuli. However, we will see later (see Sections 4.8 and 4.5) that the dynamics of the proportional amplifier model are more similar to those of the hysteretic amplifier than suggested in this chapter, because of adaptation: the adapted current-discharge curve does not reflect the current-discharge curve of the proportional amplifier model during the initial portion of the response.

We also provide some insight into the influence of nonlinearities on the model's dynamics. Under some conditions, they shorten the time constant. These nonlinearities can be incorporated into a simplified dynamical model, also called DYNAMO.

Historically, in the course of this research project, this model has been important to develop intuition and understanding of the models, since it can be simulated numerically much faster than the detailed models and often gives comparable results.

Chapter 4

Direction selectivity through proportional amplification

4.1 Introduction

In this chapter, we investigate the response properties and functioning of the cortical amplifier model in one of its two parameter regimes, proportional amplification, in comparison to a strictly feedforward model.

As introduced in Chapter 1, the cortical amplifier model is a detailed simulation of a circuit that amplifies the geniculate input to cortex in the preferred direction, through excitatory intracortical connections, and cancels geniculate excitation in the null direction through inhibition. We refer you to that chapter for the context of the results presented here.

The detailed models and the simulation methods are described in Chapter 2. We describe there the geniculate model we used to provide input to cortex. We refer you to that chapter for these explanations.

The proportional amplification mode occurs in the presence of moderate posi-

tive feedback. We refer you to Chapter 3 for a detailed explanation about the two modes of operation, and to Chapter 5 for a treatment of the other mode, hysteretic amplification.

First, Section 4.2 gives an overview of the model's basic properties, showing that it indeed amplifies the input strongly, and that in the null direction the model's input conductance changes only slightly, in agreement with intracellular data. Sections 4.3 and 4.4 show the model's responses versus contrast and velocity. Section 4.5 derives some expressions for the proportional amplifier's dynamics and uses these to explain the shape of the velocity-response curve. Section 4.6 describes the outcome of some GABA-blocking experiments for the model that show remarkable aggreement with physiology and generate experimentally testable predictions. Section 4.7 does the same for a grating superposition test. Next, Section 4.8 make the point that adaptation is crucial to obtaining a sufficient response in the presence of the small spatial offset between pyramidal and smooth neurons that is necessary for direction selectivity. Finally, Section 4.9 discusses the significance of these results within the context of current knowledge about striate cortex.

4.2 Basic performance

The salient features of the cortical amplifier model's performance in the context of direction selectivity can be seen in Fig. 4.1, which shows the somatic transmembrane potential of a typical model pyramidal neuron during presentation of a bar moving in the preferred (left-to-right direction on Fig. 2.3) and null directions. The pyramidal cell is strongly direction-selective: it generates a burst of spikes in the preferred direction, but only a single spike in the null direction (given a spontaneous activity of 1.5 Hz, we expect 3 spikes to occur during this 2 second period). We conclude that the smooth-to-pyramidal weight is large enough relative to the LGN-to-pyramidal

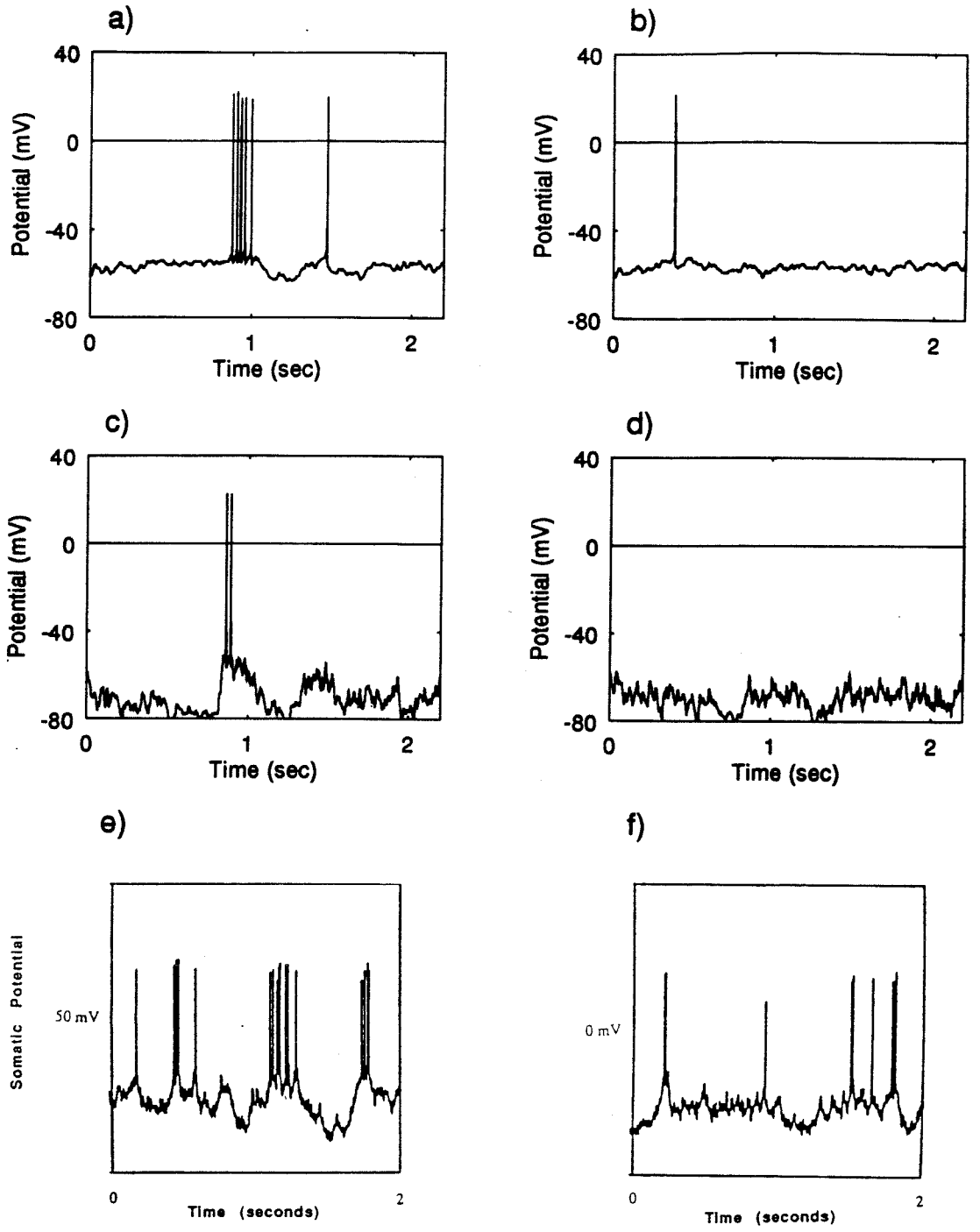

Figure 4.1: **Intracellular membrane potential in the preferred and null directions.** Somatic potential for a pyramidal neuron in the cortical amplifier model in the presence of a 70 % contrast bar moving at $2°/sec$ in the (**a**) preferred and (**b**) null direction. The same responses are shown in (**c**) and (**d**) for the feedforward model. Intracellular recordings from a neuron in primary visual cortex in the anesthetized cat (Douglas et al., 1991) during stimulation by a bar moving at $3°/sec$ in the (**e**) preferred and (**f**) null direction. Note in all conditions the presence of more spikes in the preferred direction than in the null direction. The variablity of the membrane potential is larger in the feedforward model (see Section 2.5.1).

weight so that the inhibition completely cancels LGN excitation in the null direction.

In the preferred direction the stimulus reaches the smooth neuron's receptive field after stimulating the pyramidal neurons, so that the spike discharge in the preferred direction is followed by pronounced hyperpolarization, as observed in intracellular recordings from cat visual cortex (Fig. 4.1e; Benevento et al., 1972; Creutzfeldt et al., 1974; Ferster, 1988; Douglas et al., 1991). Our simulations show that this hyperpolarization is not solely caused by inhibitory input from the smooth neurons. There are contributions also from the calcium-dependent potassium current that was activated during the spike discharge, and from the withdrawal of spontaneous LGN activity as the stimulus enters the LGN neurons' surround subfield.

During null stimulation, our cortical amplifier feedback model shows only moderate hyperpolarization (Fig. 4.1b), as observed in the recordings from cat cortex (Fig. 4.1f). Indeed, the smooth-to-pyramidal weight is relatively small. It can be that small without a reduction in direction selectivity because the LGN-to-pyramidal weight itself is small.

The intracellular response of the feedforward model shows very strong hyperpolarization both in the preferred and null directions (Fig. 4.1c and Fig. 4.1d), because the smooth-to-pyramidal weight is much larger. It has to be larger because the LGN-to-pyramidal weight is also larger.

The response of all 50 cortical neurons of the cortical amplifier model to the same stimulus is summarized in the raster plot of Fig. 4.2. For each trial, every horizontal row shows the spikes in one model neuron as dots, with one row for each of the 50 neurons in the model. Poststimulus time histograms (PSTHs) for pyramidal and smooth neurons in the cortical amplifier and feedforward models are shown in Fig. 4.3. All the pyramidal neurons show strong direction selectivity, while the smooth neurons respond equally in both directions. Some features of the direction selectivity mechanism are apparent from these plots. In the null direction the smooth cells receive

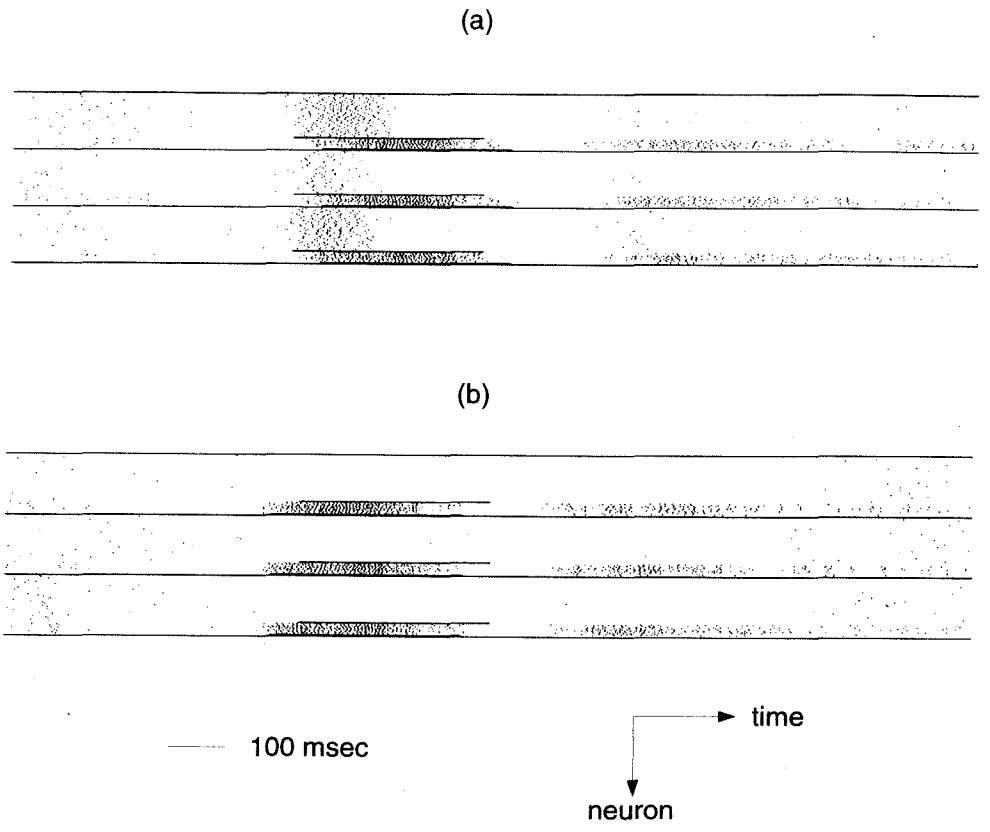

Figure 4.2: **Spike raster plots for the cortical amplifier.** Response of the pyramidal and smooth neuron population to a 70% contrast bar moving at $2^o/sec$ in **(a)** the preferred and **(b)** the null direction of motion. Three trials are shown for each direction. The first 40 rows in each trace indicate spiking activity in the pyramidal cells. The continuous bar just below these rows indicates when the stimulus is within the receptive fields of the LGN inputs to the pyramidal cells. The ten rows below the bar correspond to firing activity in the 10 interneurons. Note the strong direction selectivity of the pyramidal neurons, whereas the smooth neurons are not direction-selective. However, this is not an essential feature of our model. The spontaneous activity in the interneurons is approximately five times higher than the spontaneous activity in the pyramidal cells.

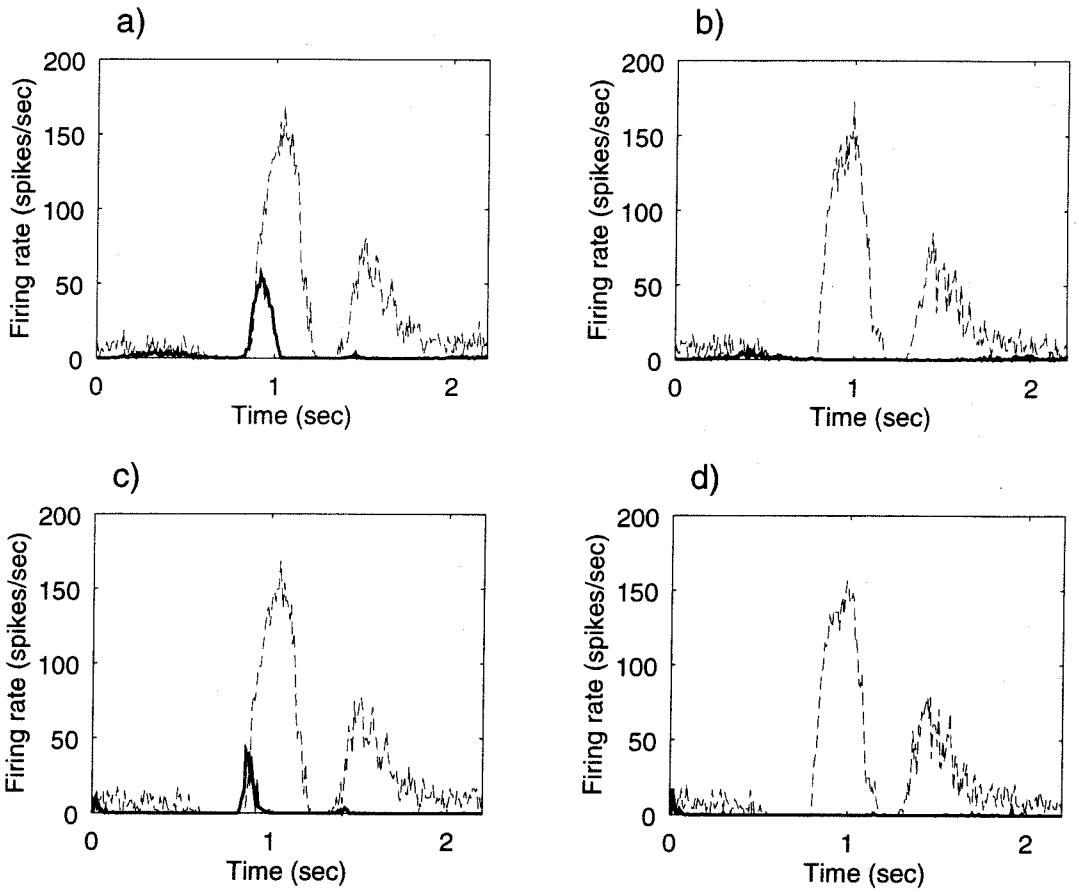

Figure 4.3: **PSTHs for the preferred and null direction.** The post-stimulus time histograms (PSTHs) for model neurons to a 70% contrast bar moving at $2°/sec$ in the preferred and null direction of motion. PSTHs are computed by summing together the discharge from all pyramidal or smooth neurons (see also Section 2.6). The PSTHs for the cortical amplifier model in the **(a)** preferred and in the **(b)** null direction (continuous: pyramidal neurons; dashed: smoooth neurons). The PSTHs for the feedforward model for **(c)** motion in the preferred and **(d)** in the null direction. Peak firing rates of the interneurons are two to three times higher than the peak firing rates of the pyramidal cells.

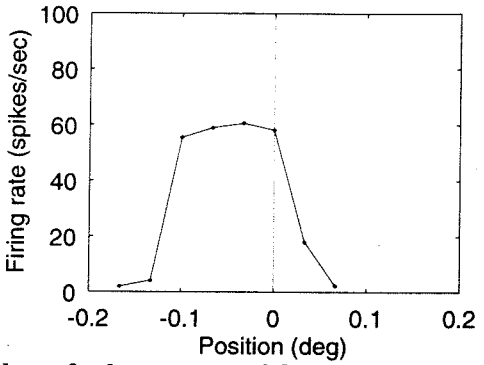

Figure 4.4: **Profile of the pyramidal neurons' excitatory subfield.** Peak response of the pyramidal neurons to a thin (2′) bar stimulus as a function of its position in their receptive field. Position 0^o is arbitrary, and corresponds to the center of the receptive field of the LGN neurons that are at the first spatial position (leftmost in Fig. 2.3). The width of the positive response is about 0.2^o.

LGN input before the pyramidal neurons because the LGN input to the smooth cells is spatially displaced with respect to that of the pyramidal cells: the spatial offset is 5′ and the bar speed is $2^o/sec$, corresponding to a pyramidal neuron delay of about 42 $msec$. Thus, in the null direction, the smooth cells are able to prevent any firing in the pyramidal cells. However, in the preferred direction the pyramidal neurons begin their discharge before the smooth cells and so the cortical amplification loop activates.

In the preferred direction, the pyramidal neurons stop firing before the stimulus leaves their receptive field, because of inhibitory input from the smooth neurons, combined with the effect of high threshold and calcium-dependent adaptation.

After discharging, the smooth neurons are suppressed when the stimulus enters their LGN neurons' surrounds. Subsequently, some discharge occurs due to rebound as the stimulus leaves the surrounds. There is little late discharge in the pyramidal neurons because they have a higher threshold.

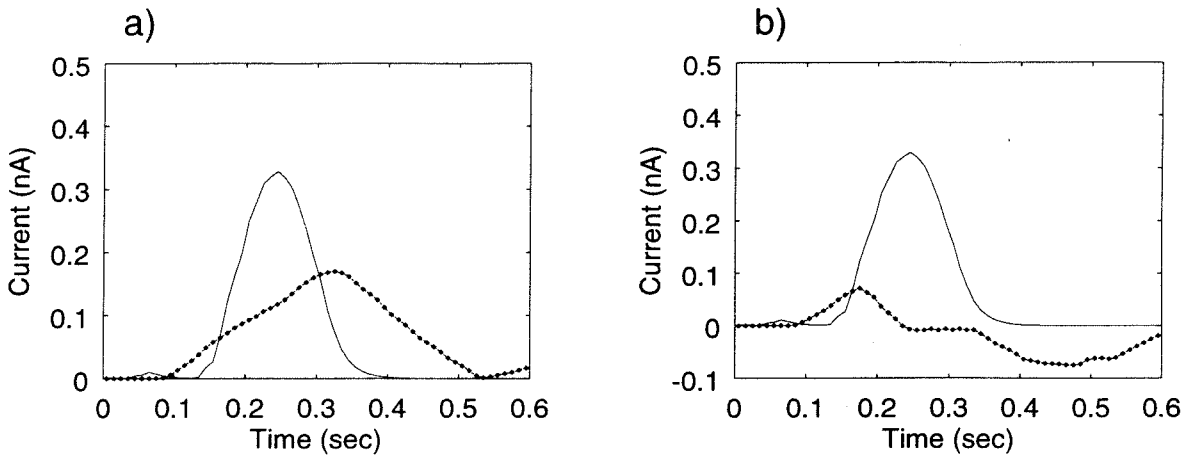

Figure 4.5: **Current amplification in the preferred direction in the cortical amplifier.** **(a)** Excitatory cortico-cortical current (solid line) compared to that arriving from the LGN afferents (dotted bold line), for a pyramidal neuron of the cortical amplifier model during stimulation by a 70% contrast bar moving at $2^o/sec$ in the preferred direction. The time course of the geniculate current is essentially given by the passage of the bar over the ON portion of the single subfield. **(b)** We here plot the same, excitatory cortico-cortical current (solid line) compared to the **net** input current (dotted bold line; see also Fig. 4.9d), defined as the difference between the excitatory current due to the geniculate input and the combined ($GABA_A$ plus $GABA_B$) inhibitory currents to the pyramidal neuron.

A receptive field profile can be measured for the model, by flashing a thin (2′) bar on and plotting the peak response to this stimulus as a function of its spatial position (Fig. 4.4). The width of the positive response is about 0.2^o; assuming that the inhibitory subfield corresponding to the action of the smooth neurons has a similar width, our estimate of the receptive field wavelength is 0.4^o. This is rather small compared to simple cell receptive field profiles (for instance, see Baker and Cynader, 1986).

High signal amplification is achieved within the canonical microcircuit. Fig. 4.5a compares the excitatory recurrent current to a pyramidal cell with the excitatory

current induced by the LGN afferents for a bar moving in the preferred direction. Clearly the dominating excitatory input during response originates from other cortical neurons rather than the LGN. The LGN-to-pyramidal synaptic weight is small; nevertheless, the pyramidal neurons discharge strongly because of the current contributed by the connections between the pyramidal neurons. However, the LGN current is not the input signal being amplified by the network of pyramidal neurons. Instead, the total input signal to the pyramidal neurons is the LGN input current minus the total inhibitory current contributed by all smooth neurons: the **net input current**. This current is shown together with the LGN current in Fig. 4.5b, for the same stimulus as Fig. 4.5a. Initially, the net input current is positive because in the preferred direction the LGN current precedes the inhibitory current. Then, the inhibitory current becomes larger than the LGN's, so the net current becomes negative. Eventually, the inhibitory current decays, as the stimulus leaves the receptive field of the inhibitory neurons. The real amplification factor achieved by the canonical microcircuit is much larger than suggested in Fig. 4.5a: it is about 4.7 in Fig. 4.5b.

In the weak LGN input lies the key to some very puzzling experimental findings. Direct measurements of somatic input conductance in cat area 17 neurons during stimulation by nonpreferred stimuli show very small conductance changes, less than 25% (Fig. 4.6c; Douglas et al., 1988, 1991; Pei et al., 1991; Ferster and Jagadeesh, 1992). Having a weak LGN input to the pyramidal neurons allows the network to be highly direction selective despite relatively weak inhibition. Such weak inhibition would not lead to large increases in the somatic input conductances during null direction stimulation. Indeed, in our simulations, the somatic input conductance only increased by at most 60% (Fig. 4.6a). In contrast, the feedforward network's conductance increased by over three times the baseline (Fig. 4.6b). The conductance changes in the cortical amplifier model argue in favor of the canonical microcircuit, and against the feedforward model based on a pure Barlow-Levick scheme.

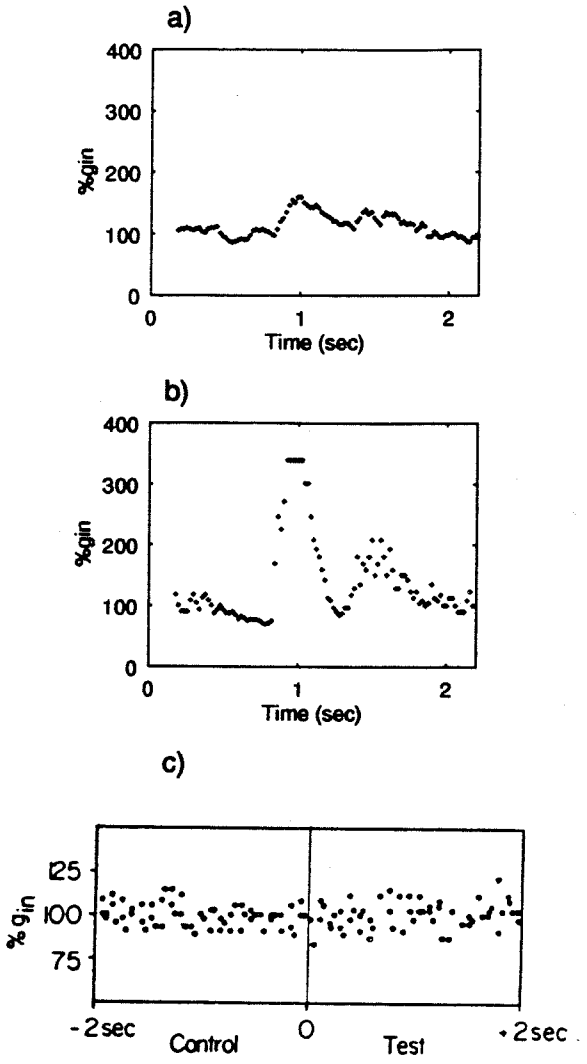

Figure 4.6: **Somatic conductance changes during null direction motion.** Shown is the percent change in somatic input conductance as a function of time for a direction-selective pyramidal neuron during stimulation by a bar moving in the null direction. The input conductance is computed by comparing the intracellular voltages in response to a bar stimulus with and without injecting a test long pulse of current (as discussed in Section 2.6). **(a)** Cortical amplifier model: the small excitatory input from the LGN afferents can be inhibited by a small inhibitory input, requiring only a moderate conductance increase. **(b)** A much larger conductance increase is required in the feedforward model due to the large LGN-mediated excitation. **(c)** Estimated conductance change in a layer 6 pyramidal cell in the anesthetized cat during null direction stimulation (from Douglas et al., 1988); $\%g_{in}$ is estimated from the decrement in membrane voltage evoked by hyperpolarizing current pulses ($20 - 30\ msec$, $0.1 - 0.5\ nA$). No significant conductance change occurs (the significance level is 25 % of baseline).

We have seen that the cortical amplifier is direction selective for one stimulus condition (a high contrast, moving bar). We will now explore more systematically how directionality depends on contrast and velocity.

4.3 Contrast dependence of response and directionality

For the cortical amplifier model, the contrast-response curve of pyramidal neurons in the preferred direction in response to a moving sinusoidal grating (Fig. 4.7b; see Section 2.6) has a threshold at about 0% contrast and is quite linear on a log-log scale with a slope of 0.62 (decade Hz/decade % contrast). Although physiologically there is much variability (Albrecht and Hamilton, 1982), these characteristics are consistent with physiological data (Dean, 1981; Holub and Morton-Gibson, 1981; Tolhurst et al., 1981a; Albrecht and Hamilton, 1982; Ohzawa et al., 1982; Albrecht and Geisler, 1991). The feedforward case's contrast-response function is quite similar to that of the cortical amplifier, despite small differences in threshold. The LGN contrast-response curve has a slope that is less than 1 on a log-log plot and compares well with physiological data in both retina and LGN showing a compressive nonlinearity (Shapley and Perry, 1986; Saul and Humphrey, 1990). The strength of the cortical amplifier's response decreases dramatically when the excitatory cortico-cortical connections are removed (Fig. 4.7h), demonstrating the extent to which they amplify the geniculate input.

The model pyramidal neurons respond very little in the null direction, and the direction index (see Section 2.6) is between 80 to 100% for most contrast values (Fig. 4.7e). The invariance of the direction index over a broad range of contrast is characteristic of visual cortical neurons (Fig. 4.7e; Dean, 1980; Orban, 1984; Li and

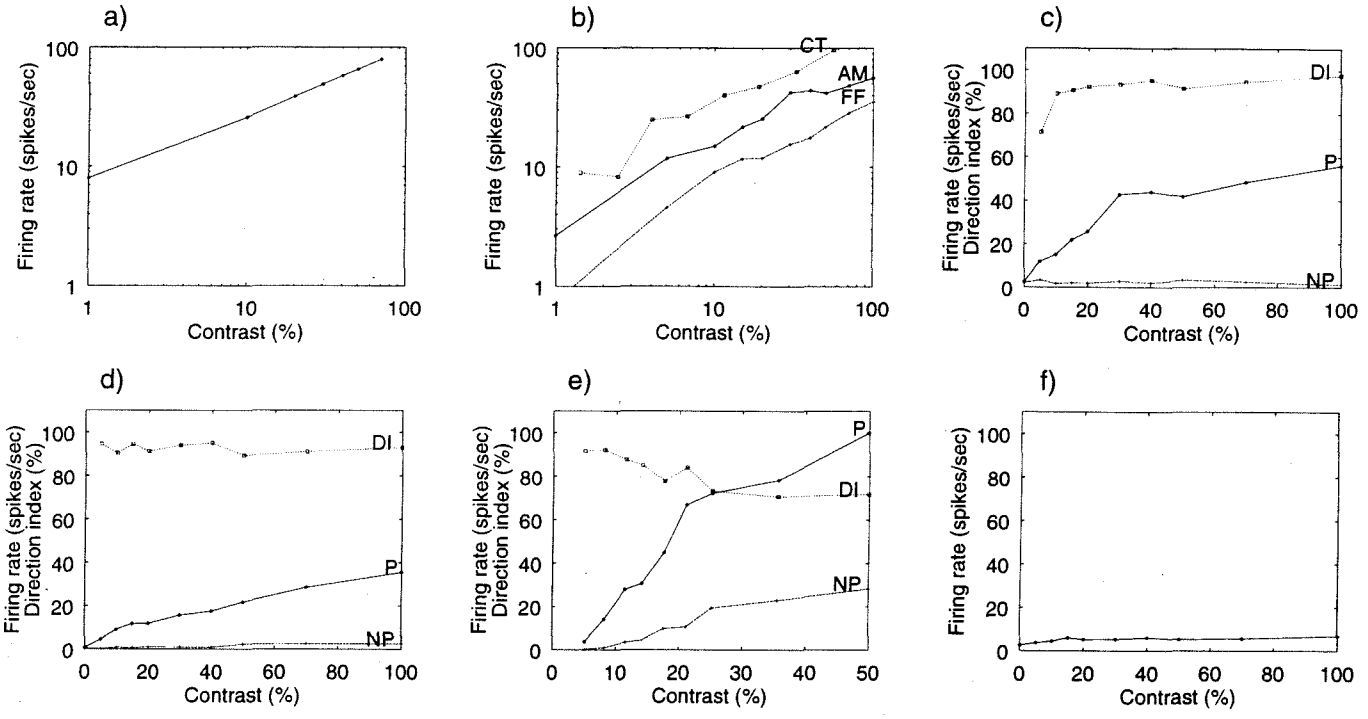

Figure 4.7: **Contrast-response curves.** Relationship between the visual contrast (eq. 2) of a moving sinusoidal grating (1 Hz, 1 c/deg) and the peak firing rate for different stages in our model, compared to physiological data. The peak firing rate is computed from post-stimulus time histograms summed over the entire population of pyramidal neurons (see Section 2.6). **(a)** Peak geniculate response given by the Victor (1987) model. **(b)** The amplitude of the first Fourier harmonic component from a cortical neuron in cat area 17 (label **CT**; adapted from Albrecht and Hamilton, 1982) compared to the response in the preferred direction for pyramidal neurons in the cortical amplifier (AM) and in the feedforward model (FF). The next three panels show the peak response in the preferred (P) and null direction (NP) of motion as well as the direction index ($DI = (P - NP)/P$; eq. 2.5) for pyramidal neurons in the **(c)** cortical amplifier or in the **(d)** feedforward model as well as **(e)** for a simple cell in cat area 17 (responding to a 2 Hz drifting sinusoidal grating; adapted from Tolhurst and Dean, 1991). Both models are direction selective over the full range of contrasts. **(f)** Peak response to motion in the preferred direction in the cortical amplifier model in the absence of any excitatory, cortico-cortical connections.

Creutzfeldt, 1984; Tolhurst and Dean, 1991). Over 20% of area 17 neurons (and in particular, area 17 simple cells) have direction indices at the optimal velocity between 80 and 100% (Albus, 1980; Berman et al., 1987; Gizzi et al., 1990; Reid et al., 1991; Tolhurst and Dean, 1991; DeAngelis et al., 1993; McLean and Palmer, 1994). Even the Mean Direction Index (MDI, see Section 2.6) is larger than 80% for at least 15% of neurons (Orban et al., 1981b, 1987; Orban, 1984; McLean et al., 1994).

4.4 Velocity dependence of response and directionality

A strong test of any model of direction-selective cells in area 17 is whether model neurons are *velocity low-pass*, as are 63% of area 17 cortical neurons (Fig. 4.8e; Orban et al., 1981a; Orban, 1984). These neurons respond very well to low velocities and little to velocities above $20^o/sec$. This property does not originate from LGN neurons, which have tuned, band-pass velocity-response curves with strong responses at high velocities (Fig. 4.8b; Dreher and Sanderson, 1973; Lee and Willshaw, 1978; Frishman et al., 1983; Orban et al., 1985; Gulyas et al., 1990). A further test is the extent to which direction selectivity persists over a wide range of velocities; indeed, velocity low-pass cells usually have a flat DI-velocity relationship (Orban et al., 1981b; Orban, 1984; Fig. 4.8f).

Model LGN neurons have physiologically plausible velocity-response curves (Fig. 4.8a), and the feedforward model's dependence on velocity (Fig. 4.8d) is similar, with the addition of a threshold, further reducing the peak response at low velocities.

In contrast, the cortical amplifier's velocity tuning curve (Fig. 4.8c) is similar to area 17 velocity low-pass neurons: its response drops off by only 35% of the maximum response (70 Hz) at very low velocities but by more than 50% for velocities above

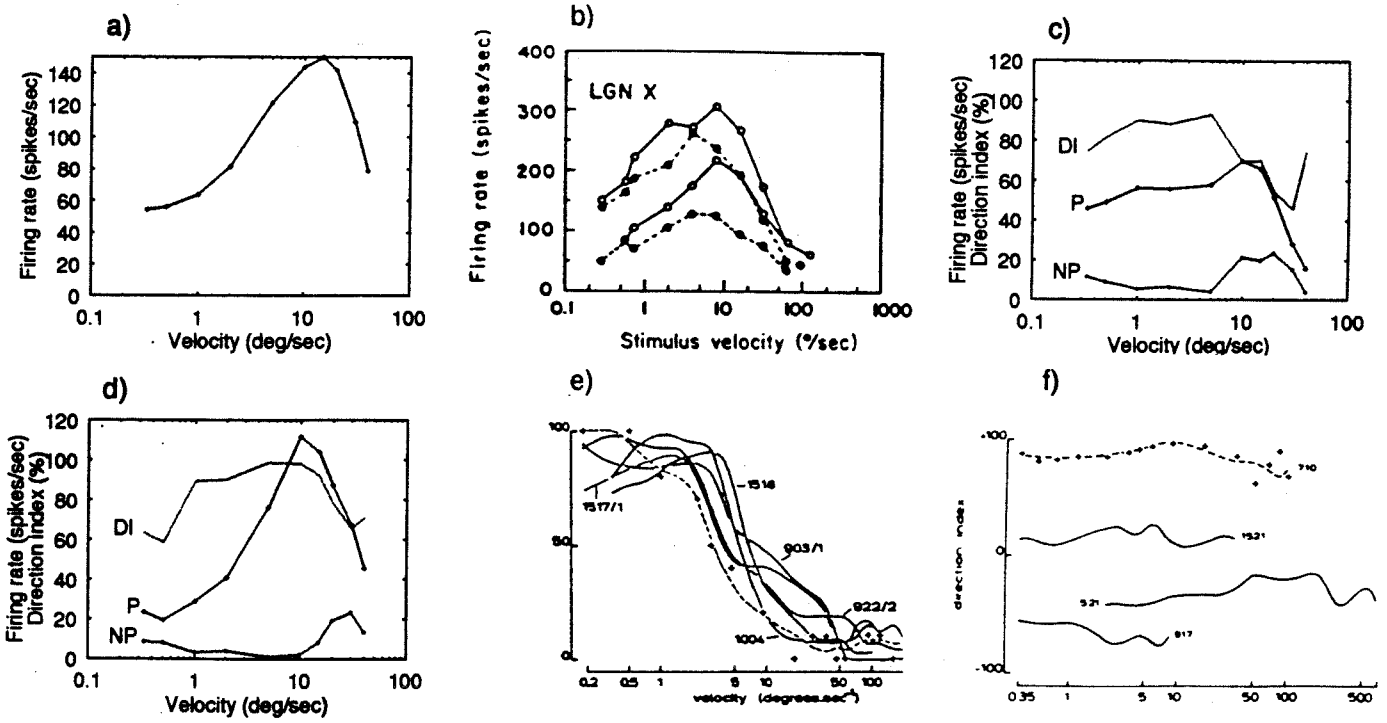

Figure 4.8: **Velocity-reponse curves.** Shown is the peak firing rate for a 70 % contrast bar as a function of its velocity (see Section 2.6) at different stages in our model, compared to physiological data. **(a)** LGN model peak response given by the Victor(1987) model. **(b)** Peak response of X geniculate cells in the adult, anesthetized cat (Frishman et al., 1983). The following two panels show the peak response in the preferred (P) and null direction (NP) of motion as well as the direction index ($DI = (P - NP)/P$; eq. 2.5) for pyramidal neurons in the **(c)** cortical amplifier or in the **(d)** feedforward model. Both feedforward and cortical amplifier models are direction selective over two orders of magnitude of speed. **(e)** Representative examples of velocity-response curves from velocity low-pass cells in cat visual cortex (Orban (1984), Fig. 8/5 C). **(f)** Examples of flat velocity-direction index (velocity-DI) curves from recordings in the adult cat (Orban, 1984 : Fig. 8/11 A). Note that by convention the DI is negative if the preferred direction had a downward component.

$20°/sec$. The response at the lowest velocity tested ($0.33°/sec$) is much larger than that at the highest velocity ($40°/sec$).

Similarly to velocity low-pass neurons, the cortical amplifier model's dependence of direction index (DI; see Section 2.6) on velocity is relatively flat over two orders of magnitude (Fig. 4.8c), reflecting the small response in the null direction at all velocities; this invariance depends on two varieties of GABA mediated inhibition, as explained in the following section. The Mean Direction Index (MDI; see eq. 2.6, Section 2.6) is 76%, indicating that the cell is direction-selective in Orban's (1984) nomenclature, rather than direction asymmetric. At high velocities, direction selectivity is less strong, which parallels physiological data showing that a majority of cortical neurons having a direction preference that is stable with temporal frequency lose part or all of their direction selectivity above 1 or 2 Hz (corresponding to 4 or $10°/sec$; Saul and Humphrey, 1992).

4.5 Analysis of the velocity-response curve

The feedback excitatory connections in the cortical amplifier model result in a response that decreases much less at low velocities than the LGN model's (Fig. 4.8). Furthermore, the response at high velocities ($10°/sec$ and above) is much diminished compared to the LGN neurons. Moving bars are transient stimuli, and these transformations are related to whether the network reaches equilibrium for bar stimulus with a given velocity, which depends in turn on the duration of the stimulus compared to the network's time constant. So we will now study the cortical network's dynamics. Using the linear approximation (eqs. 3.3 and 3.4 in Section 3.2) and neglecting the membrane time constant, we have seen in Section 3.5 that the system can be

described by the following differential equation (see eq. 3.19):

$$\frac{\tau_{syn}}{1-\alpha}\frac{df}{dt} = -f + \frac{k_{F_i}}{1-\alpha}(I_l - I_i - I_T) \tag{4.1}$$

where τ_{syn} is the decay time constant for the excitatory synaptic conductance change ($20\ msec$), k_{F_i}, the slope of F_i, I_l, the LGN input current, and I_i, the inhibitory input current.

According to this equation, the pyramid firing rate f settles to steady-state with a certain time constant, the network's time constant $\tau_{net} = \tau_{syn}/(1-\alpha)$. In conditions where there is amplification of the input, *i.e.,* when α is slightly smaller than 1, the network's time constant becomes much larger than τ_{syn}. This should be the case for the proportional amplifier model (see Fig. 3.1b).

Potentially, this very long time constant could explain the enhanced response of the cortical amplifier at low velocities, as in Maex and Orban (1992). However, Fig. 4.9a shows that for a constant current injection lasting 25 $msec$, the network already reaches the firing rate that it will eventually settle to (after adaptation is complete) if the input were sustained. In other words, for a stimulus duration of 25 $msec$ or more, the network's amplification, measured from its peak firing rate at that velocity, would be the same as for a sustained stimulus. We can therefore assume—for the purposes of the velocity-response curve—that $\tau_{net} \approx 25\ msec$, close to τ_{syn}. This short network time constant originates in the calcium-dependent adaptation in the pyramidal neurons (see Section 4.8). Indeed, the slope of the unadapted F_i is substantially larger than that of the adapted F_i (see Fig. 3.1a), so that initially α is larger than 1 (eq. 3.5). So the dynamics are similar to the hysteretic amplifier's (see Section 5.6). So there is faster growth of the firing rate during the initial portion of stimulus presentation, resulting in the short time constant demonstrated in Fig. 4.9a.

This initial time constant is too short to account for the sharp decrease in am-

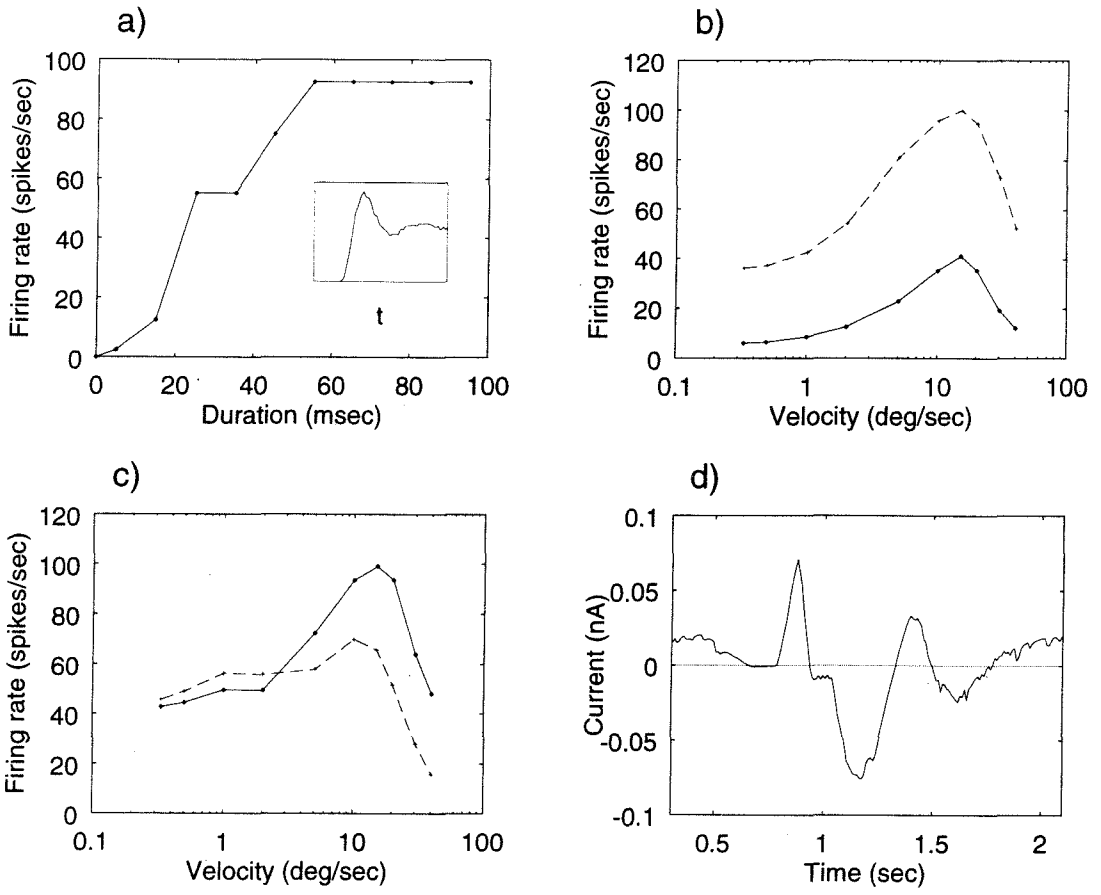

Figure 4.9: **Explaining the cortical amplifier's velocity-response curve. (a)** For a constant current injection of 0.1 nA into all pyramidal neurons, peak firing rate as a function of the duration of the stimulus. The inset shows the pyramidal firing rate as a function of time for the current injection. For 0.1 nA, the steady-state firing rate is 48 Hz (see Fig. 3.1c); that firing is reached already in 25 $msec$, so in that sense the time constant of the system τ_{net} is 25 $msec$. Notice that due to adaptation, the maintained firing rate of the system is lower than its peak firing rate. **(b)** Velocity-response curve obtained in the preferred direction when all recurrent synapses have been removed (continuous), compared to the LGN's velocity-response curve (dashed; see also Fig. 4.8a). **(c)** Comparison of the velocity-response curve for the cortical amplifier in the preferred direction (dashed; see also Fig. 4.8c) with an approximating curve (continuous) obtained by multiplying the firing rates in (b) (continuous) by the firing rate gain $G(f)$ from Fig. 3.1d. **(d)** The time-course of the net input current in a pyramidal neuron, defined as the geniculate current minus the total inhibitory current, for a 70% contrast bar moving at $2°/sec$ in the preferred direction (see also Fig. 4.5b).

plification between low velocities and a velocity of, say, $5^o/sec$. Fig. 4.9b plots the velocity-response curve obtained when the cortical amplifier's excitatory cortico-cortical connections were removed. The overall shape is very similar to the LGN's velocity-response curve after scaling and thresholding. The response at low velocities is very small. However, as can be seen in Fig. 3.1d, the firing rate gain $G(f)$ is much larger for small input firing rates than for large ones, due to nonlinearities in the Hodgkin and Huxley spike production mechanism and dendritic driving potential saturation. Consequently, the LGN input is more strongly amplified at low than at high velocities.

This argument can be made more quantitative. We multiplied the firing rates in the absence of excitatory feedback as a function of velocity (Fig. 4.9b) with $G(f)$ (Fig. 3.1d). This simple approximation (Fig. 4.9c) is remarkably accurate at $5^o/sec$ and lower velocities, explaining the strong responses to low speeds, despite changes by a factor of two in the geniculate firing rate between $0.33^o/sec$ and $5^o/sec$.

At speeds of $10^o/sec$ and above, the actual amplification is much lower than predicted (Fig. 4.9c). This reduction arises because the stimulus duration diminishes with velocity, and at some point is too short to allow buildup of excitation in the network.

It is important to realize here that stimulus duration is not the same as the dwell time of the stimulus within the center portion of an LGN cell. Because LGN inputs to the pyramidal and smooth neurons overlap spatially, inhibition in the preferred direction arises from the smooth neurons while there is still LGN input to the pyramidal neurons. Therefore, the stimulus duration should be estimated instead from the difference between the excitatory geniculate and total inhibitory currents, called net input current. Fig. 4.9d represents the net input current to a pyramidal neuron for a bar moving at $2^o/sec$ in the preferred direction. At rest, the LGN background activity is responsible for some positive net input current (about 0.02 nA). As the

stimulus enters the surround of the LGN neurons, their spontaneous response is inhibited, reducing the net input current to zero. When the stimulus enters the center portion of the LGN neurons, the net current quickly increases to about 0.075 nA. As the LGN input fields of the smooth neurons overlap with those of the pyramidal neurons, inhibitory current from the smooth neurons quickly reduces the net current to -0.08 nA. Subsequently, the net current first increases due to rebound when the stimulus leaves the pyramids' surround, then goes negative with rebound from the smooth neurons' surround, before reverting to its spontaneous background value.

Stimulus duration can be estimated from the largest positive phase of the net input current trace, and is on the order of $50-100$ $msec$. Since the stimulus duration is inversely proportional to velocity, at $10°/sec$ the duration is $10-20$ $msec$, which is slightly less than the system's $25msec$ time constant. This explains the reduced amplification at high velocities.

In summary, two processes are responsible for transforming the LGN's velocity-response curve into the cortical amplifier's. First, in contrast with Maex and Orban (1992), the elevated response at low velocities does not originate in the network's time constant being lengthened by the excitatory feedback; instead, it results from nonlinear amplification that is larger at low than at high LGN inputs. Secondly, the upper cutoff velocity is determined by the duration of the positive phase of the net input current and by the network's time constant, which in this case is only about 25 $msec$, due to calcium-dependent adaptation.

4.6 GABA blocking experiments

In the model, $GABA_A$ receptors give rise to short-latency, transient inhibition; in contrast, $GABA_B$ is associated with long-latency, prolonged inhibition (see Table 2.1). Paralleling these differences in dynamics, $GABA_A$ and $GABA_B$ are responsible for

model direction selectivity at different velocities. At low velocities, there is a large time difference in the onset of the LGN input to smooth and pyramidal neurons, and $GABA_B$ mediates the inhibition that vetoes the response in the null direction. At high velocities, the difference in time of onset is small, requiring short-latency $GABA_A$ inhibition for direction selectivity. Therefore, the model can be used to make specific predictions about the effect of blocking $GABA_A$ or $GABA_B$ or both. Fig. 4.10 illustrates how the cortical amplifier's velocity-response and DI curves transform under partial or complete block of inhibition, as in physiological experiments involving iontophoresis of antagonists (see for instance Sillito, 1977).

In the null direction, blocking $GABA_A$ receptors increases the response dramatically at high velocities, thereby abolishing direction selectivity (Fig. 4.10c). It has little effect at low velocities. Conversely, blocking $GABA_B$ receptors strongly increases the null response at low velocities—eliminating direction selectivity here—but very little at high velocities. As expected, blocking both varieties of inhibition abolishes direction selectivity at all velocities. These results can be contrasted with the outcome of physiological experiments, where direction selectivity diminishes strongly or disappears under $GABA_A$ blockade (Sillito, 1975, 1977; Wolf et al., 1986) but does not appear to be reduced by $GABA_B$ blockade (Baumfalk and Albus, 1988). The velocities at which the experiments were performed were not reported.

In the preferred direction, blocking $GABA_A$ results in a velocity-response curve that is velocity broadband (for the definition of velocity broadband see Orban, 1984) and quite similar to the LGN model's curve (Fig. 4.8a), except at low velocities. In particular, the response at velocities higher than $20°/sec$ is large, as in LGN neurons and unlike area 17 velocity low-pass neurons. $GABA_A$ feedforward inhibition is responsible for the upper velocity cutoff.

A variant of that experiment is to block both $GABA_A$ and $GABA_B$ receptors onto a single pyramidal cell and to measure direction selectivity in that particular

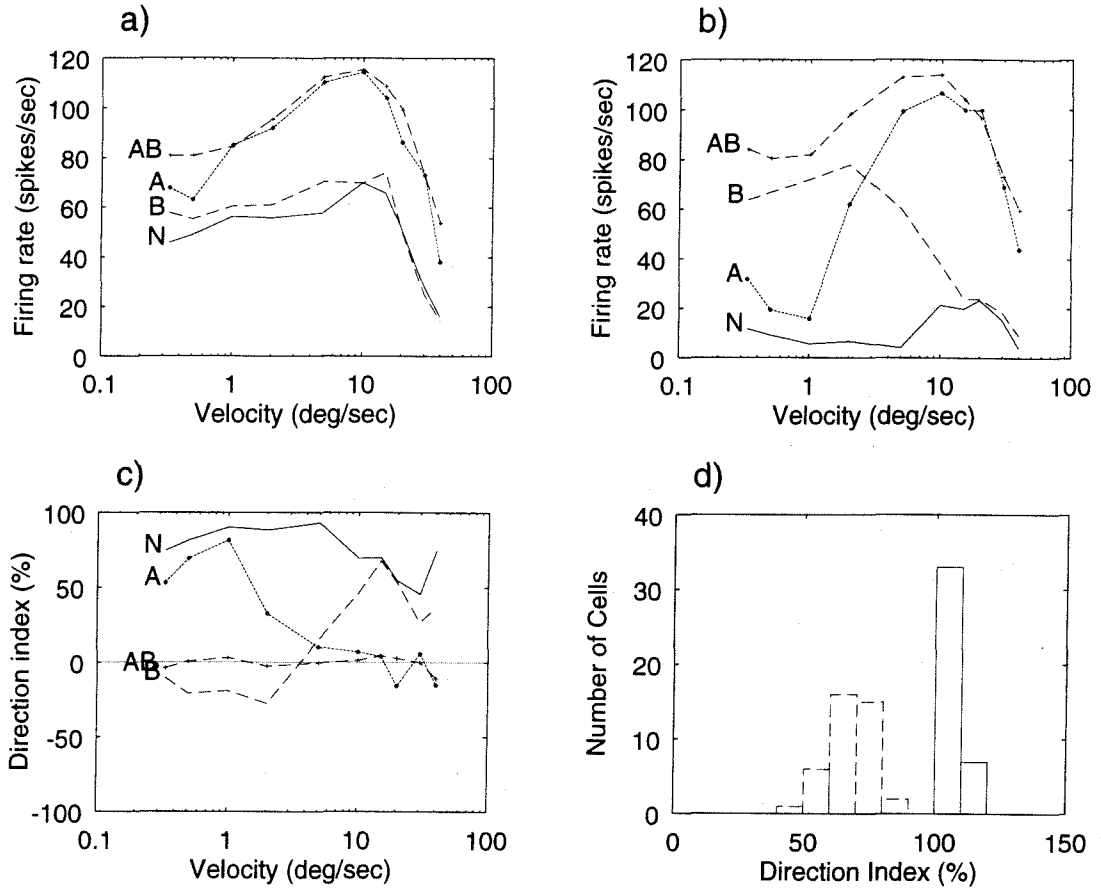

Figure 4.10: **Blocking inhibition and direction selectivity.** The first two panels show the peak firing rate for a 70% contrast bar as a function of velocity for motion in the **(a)** preferred and in the **(b)** null direction. The N curve indicates the normal response for the cortical amplifier. The peak firing rate increases when fast "shunting" $GABA_A$ inhibition is blocked (curve A). Removing only slow hyperpolarizing $GABA_B$ inhibition leads to curve B, while curve AB is obtained in the absence of any inhibition. The associated progressive loss in direction selectivity is documented for the pyramidal cells in **(c)**. Blocking fast $GABA_A$ inhibition leads primarily to a loss of DI at high speeds, while the blockade of $GABA_B$ inhibition primarily affects DI at low speeds. In these simulated experiments, inhibition to all cells was eliminated. In **(d)** we demonstrate the effect of blocking both $GABA_A$ and $GABA_B$ inhibition to a single pyramidal cell (see also Section 2.6). Such an experiment was carried out by Nelson et al. (1994) using GABA blockers intracellularly. DI was assessed with a 70% contrast bar. The average DI for all 40 pyramidal cells in the normal case (solid boxes) is $108\% \pm 2\%$. When blocking inhibition to a single pyramidal cell only, DI in that cell is reduced to $68\% \pm 8\%$ (dashed boxes; here carried out for each pyramidal cell in the network).

neuron before and after the block. Such an experiment can be repeated for each neuron in the cortical amplifier in turn, and the results plotted as histograms of the distribution of direction selectivity indices before and after blockade (see also Section 2.6; Fig. 4.10d). The response measure used in this case was the average number of spikes while the stimulus is in the neuron's receptive field; the neurons' firing rate was depressed below the spontaneous level in the null direction, resulting in direction selectivity indices larger than 100% for all neurons. Blocking inhibition in a single neuron gives strikingly different results from blocking inhibition in all neurons. Direction selectivity diminishes but is by no means abolished; similar results were obtained experimentally (Nelson et al., 1994).

The cortical amplifier model maintains direction selectivity down to velocities as low as $0.33^{o}/sec$ (see Fig. 4.8), in agreement with physiological data (Orban, 1984; Duysens et al., 1987; Saul and Humphrey, 1992). We have seen above that direction selectivity at low velocities depends on $GABA_B$; in addition, it depends on having a small spatial offset between the receptive fields of pyramidal and smooth neurons. We demonstrate this in Fig. 4.11. In this figure, we change the offset from one spacing between geniculate cells ($5'$) as in the current model, to two spacings ($10'$) and plot the response in the preferred and null direction, and the direction index, as a function of bar velocity. Direction selectivity at the lowest velocity is abolished.

There is a direct numerical relationship between this low velocity limit and offset and duration of $GABA_B$ inhibition. For motion at low velocities in the null direction, there is a time interval when the bar has left the smooth neurons' receptive field but is still stimulating the pyramidal neurons; since the spatial offset is $5'$, this interval lasts 250 $msec$ at $0.33^{o}/sec$, approximately equal to the duration of $GABA_B$ synaptic conductance changes in the model; larger spatial offsets or lower velocities would imply a loss of direction selectivity. In the model, the ratio of the spatial offset and $GABA_B$'s time constant will determine the lowest velocity for which direction

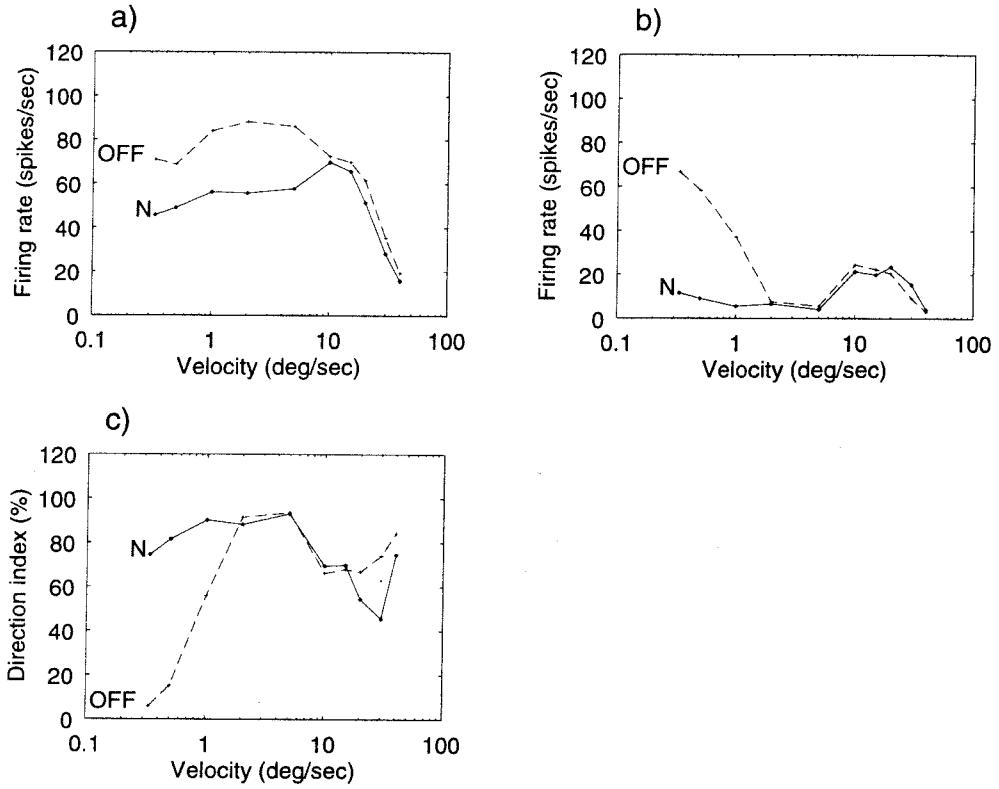

Figure 4.11: **Spatial offset and direction selectivity.** The first two panels show the peak firing rate in pyramidal neurons for a 70% contrast bar as a function of velocity for motion in the **(a)** preferred and in the **(b)** null direction. The N (continuous) curve indicates the response for the normal cortical amplifier. OFF (dashed) is the response in a modified cortical amplifier where the spatial offset between the receptive fields of pyramidal and smooth neurons has been doubled, from 5′ to 10′. The associated loss in direction selectivity at low velocities is documented in **(c)**.

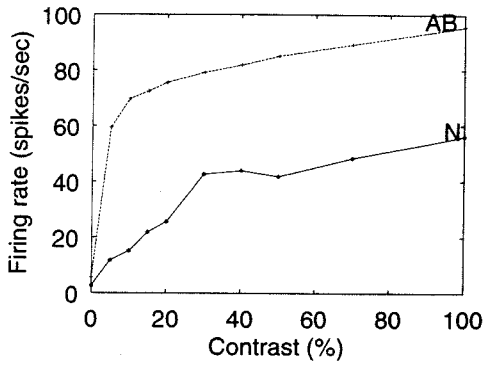

Figure 4.12: **Blocking inhibition and contrast-response curve.** This figure shows the peak firing rate for a moving sine grating (1 Hz, 1 c/deg) as a function of contrast for motion in the preferred direction, for the cortical amplifier model (N) and while blocking both $GABA_A$ and $GABA_B$ (AB). Blockade dramatically increases the initial gain of the contrast-response curve, as well as the firing rates at high contrast, but does not prevent saturation of the response.

selectivity is still observed.

In addition to its role in direction selectivity, inhibition has a strong influence on the contrast-response curve, too. Fig. 4.12 compares the response to contrast when blocking both $GABA_A$ and $GABA_B$ to the regular case (as in Fig. 4.7b). The initial gain of the contrast-response curve is very much increased by blockade. Although saturation still occurs under blockade, the model neurons discharge at far higher rates for saturating contrasts.

4.7 Linearity to superposition

Ferster and his colleagues (Jagadeesh et al., 1993) carried out an elegant set of intracellular experiments in direction-selective simple cells. They showed that the (somatic) membrane potential signal evoked by a drifting sinusoidal grating can be predicted

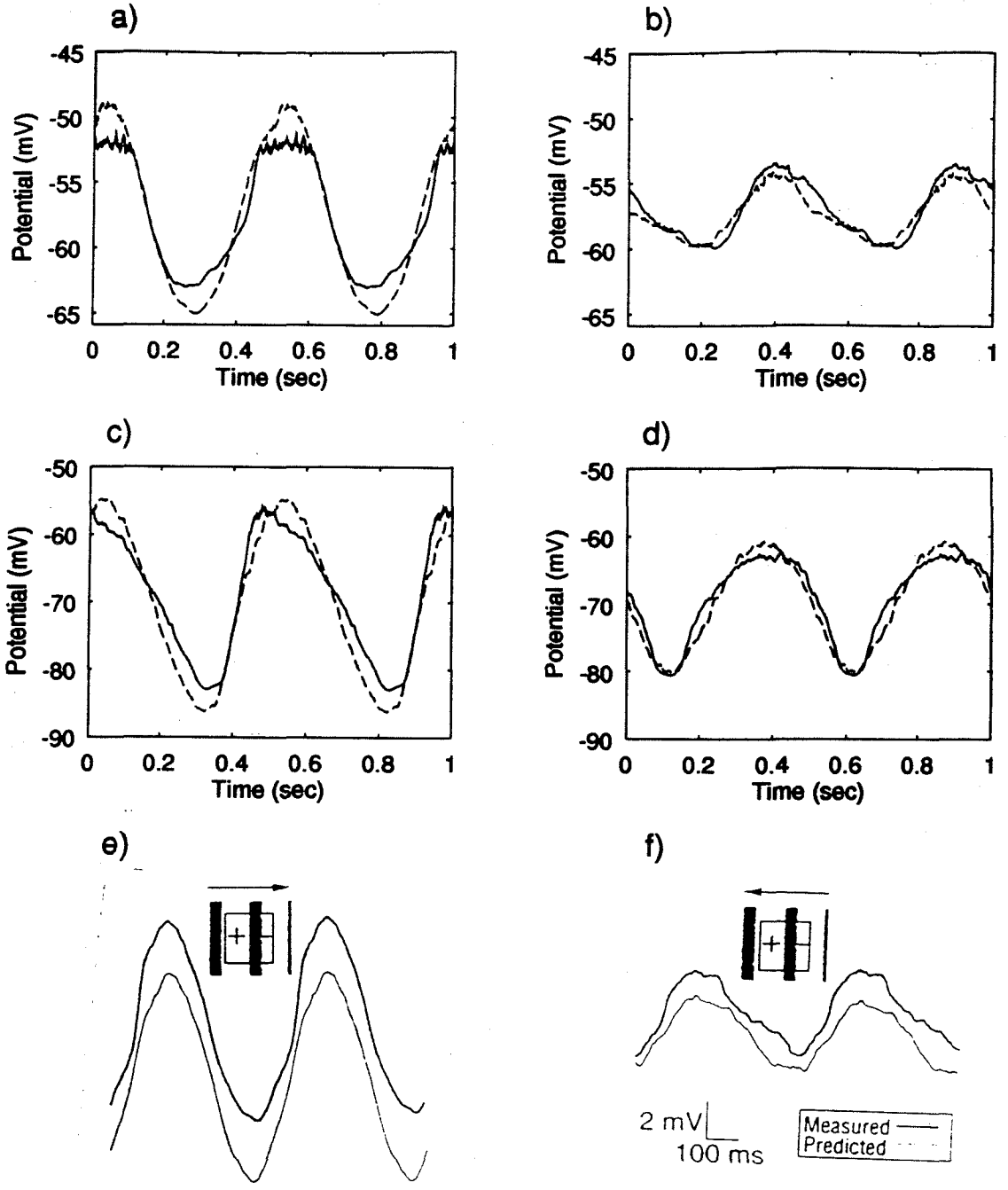

Figure 4.13: **Superposition test for the detailed models and cat cortex** The first four panels compare the modulations in membrane potential evoked (continuous) by a 1 *cycle/deg* sine wave grating, drifting in two directions at 2 *Hz* (2°/*sec*), and the response predicted (dashed) from summing stationary contrast-reversal gratings (see Section 2.6), for one cell in both cortical amplifier and feedforward models. Each trace is an average of the response to 57 grating cycles, and shows two copies of the average response to one grating cycle side by side. The last two panels compare evoked and predicted response for a simple cell in cat visual cortex (Jagadeesh et al., 1993). (**a**) Preferred and (**b**) null direction for the cortical amplifier model (100 % contrast gratings), (**c**) preferred and (**d**) null direction for the feedforward model (50 % contrast gratings), and (**e**) preferred and (**f**) null direction for the simple cell in cat visual cortex. Surprisingly, superposition holds for both feedforward and cortical amplifier networks, as in cat simple cells.

from the linear sum of responses to stationary contrast-reversal gratings at several spatial phases, seemingly implying a simple linear feedforward model of direction-selective simple cells. The reader is referred to Section 2.6 for a detailed description of this test.

In the preferred and null directions, the average membrane potentials could be predicted with an accuracy comparable to the experimental results (Fig. 4.13). There was no need to adjust any parameters specifically to obtain the fit. For the cortical amplifier, this result is surprising in view of the importance of amplification for the model's functioning.

The preferred direction of motion as well as the direction index measured from the modulations of the intracellular somatic membrane potential (see Section 2.6) could be predicted from the responses to the stationary gratings. The actual indices were 43.5% and 33.3% for the cortical amplifier and feedforward models respectively, while the predicted indices were 66.0% and 39.4%. The direction index measured intracellularly was much smaller than the direction index measured from the peak firing rate in both cortical amplifier (43.5% versus 93.2%) and feedforward models (33.3% versus 97.4%), as has been observed in cat visual cortex (Jagadeesh et al., 1993).

Since there are many nonlinearities in the cortical amplifier, an explanation of why that model passes the superposition test requires detailed analysis. The reader is referred to Chapter 6. In summary, nonlinearities in both feedforward and cortical amplifier models originating from half-wave rectification of LGN inputs cancel because of spatial summation in the cortical neurons and spatio-temporal summation through the superposition test. Nonlinearities originating from amplification in the positive phase of the input current to the pyramids are mitigated by current sinking during spike production.

4.8 Adaptation is crucial

Linear dynamics (Section 3.5) would predict a network time constant of $\tau_{net} = \tau_{syn}/(1-\alpha)$, where τ_{syn} is the time constant of the excitatory synapse (20 $msec$) and α is the initial slope of $F(f)$. Since the steady-state gain of the proportional amplifier is as large as 8 (see Section 3.2), τ_{net} might be as large as 160 $msec$. For direction selectivity at low velocities, a small spatial offset between pyramidal and smooth neurons is necessary (see Fig. 4.11); however, it also implies a short duration of the net input. For the 5′ spatial offset used in the model, the stimulus duration will be about 80 $msec$ for a grating moving at 1 deg/sec, which is the stimulus used for the contrast-response. Potentially, the network time constant is much larger than the stimulus duration, which could imply only small peak responses. However, we have seen in Section 4.5, Fig. 4.9, that the network's time constant is 25 $msec$. Indeed, adaptation is present in pyramidal cells (see Section 2.4), so that initially during the response pyramidal cells fire much more strongly; this is reflected in the slope of the unadapted F_i, which is substantially larger than that of the adapted F_i (see Fig. 3.1a). The result is that initially during response α is larger than 1 (eq. 3.5), so the dynamics are similar to the hysteretic amplifier's (see Section 5.6). There is growth of the firing rate during the initial portion of stimulus presentation according to an exponential with a positive exponent, much faster than an exponential with a negative exponent, resulting in the short time constant.

We can confirm directly that the response to transient stimuli is increased by the stronger discharge in the unadapted state (Fig. 4.14). We can accelerate the dynamics of calcium in the model, while maintaining the same equilibrium calcium concentrations. The result is that adaptation sets in much faster, so that the unadapted current-discharge curve already is partly adapted and so is shallower (Fig 4.14a), but the adapted current-discharge curve does not change (Fig 4.14b). Since the un-

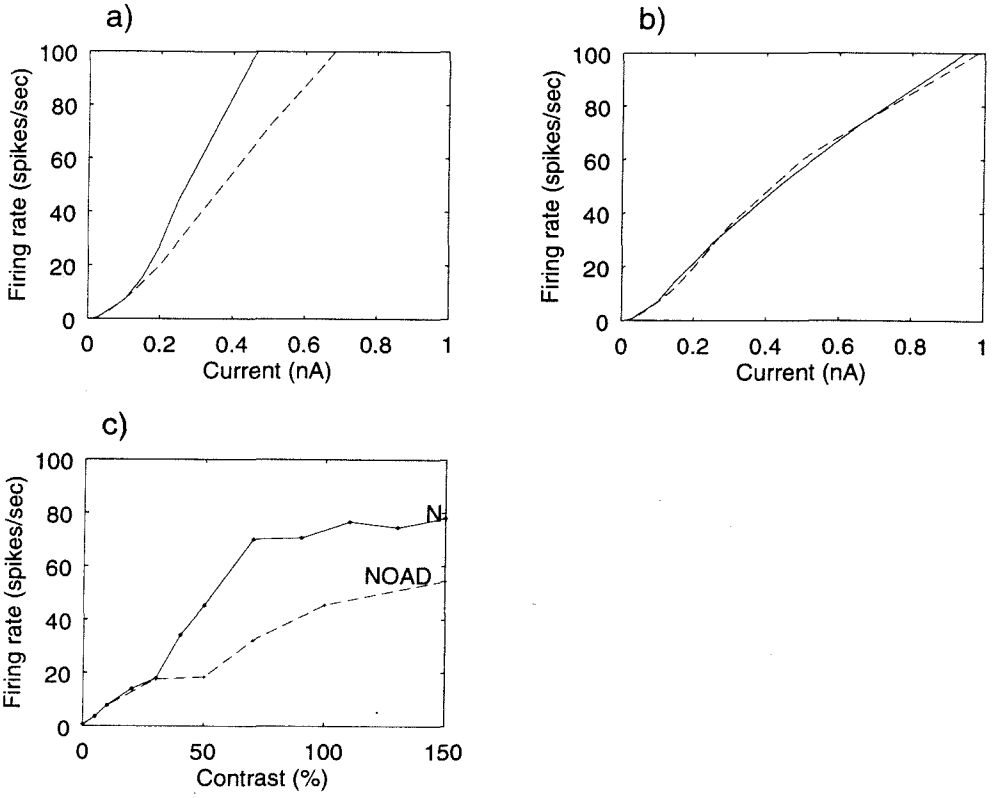

Figure 4.14: **Effect of adaptation on the contrast-response curve.** **(a)** Unadapted current-discharge curve (initial firing rate to a pulse of current) of a pyramidal neuron in two parameter conditions of the model: a condition similar to the normal proportional amplifier model (continuous) and a condition where the calcium dynamics were accelerated, from 50 *msec* to 10 *msec*, so that substantial adaptation was already present from the start of the response (dashed). **(b)** Adapted current-discharge curve for the same two parameter conditions as (a). They are nearly identical. **(c)** Contrast-response curves, to bars (2 *deg/sec*) for the two parameter conditions. Although the adapted current-discharge curves are the same, the contrast-response curves are quite different, showing that the response to transient stimuli is strongly influenced by the discharge behavior of the neurons before adaptation sets in.

adapted state is now shorter, we would expect that the responses to transient stimuli become smaller. Indeed, the contrast-response curve is more shallow, especially at or around 20 Hz, which corresponds to when the unadapted current-discharge curves of both cases start diverging. Note that we would expect an even larger decrease if adaptation was present from the very start of the response. Here, adaptation is not present until 10 $msec$ into the response.

4.9 Discussion

The *canonical microcircuit* (Fig. 1.1b) is the embodiment of compelling anatomical observations showing massive excitatory cortico-cortical feedback connections among spiny stellate and pyramidal cells in mammalian visual cortex (Berman et al., 1992; Peters and Payne, 1993; Ahmed et al., 1994; Peters et al., 1994). Physiological support derives primarily from intracellular recordings in response to electrical pulse stimulation of cortical afferents (Douglas and Martin, 1991) and from pharmacological blockade experiments (Grieve and Sillito, 1991). We have examined how such recurrent excitation provides a powerful computational principle in the operation of cortical circuits, within the context of a realistic simulation of the dynamics of a small set of cortical neurons, operating in the proportional amplifier mode (the hysteretic amplifier mode is studied in Chapter 5).

4.9.1 Basic mode of operation

The results described above provide a strong case in favor of the canonical microcircuit. As argued previously (Douglas et al., 1988), feedforward models of DS, such as the Barlow and Levick (1965) model, require large conductance changes in the null direction, greater than 100% (Fig. 4.6b). However, direct measurements of so-

matic input conductance in the null direction have only demonstrated surprisingly small conductance changes (Fig. 4.6a; Douglas et al., 1988, 1991; Pei et al., 1991; Ferster and Jagadeesh, 1992). In our detailed simulations, we find that the canonical microcircuit shows relatively small changes in conductance (Fig. 4.6c), confirming a previous report with much more simplified neurons (Douglas and Martin, 1991).

The recurrent feedback acts as a current amplifier (Fig. 4.5), enabling a comparatively weak geniculate input to be greatly amplified. In this view, DS arises through inhibition in the null direction combined with amplification of the signal in the preferred direction. Recurrent excitation together with feedforward inhibition realizes a selective cortical amplifier, which amplifies the direction-selective signal only. The result is strong DS at all contrasts and velocities for which there is a response.

This strong amplification does not prevent the cortical neurons from ceasing to respond once the visual input moves out of their receptive fields. Although slightly higher intracortical excitation would allow the network to function in a "hysteretic" mode of operation (Fig. 3.3b), even then inhibition would prevent the network from firing in the absence of stimulus. In the present simulations, the role of inhibition is to bound the overall level of excitation, to control the gain of the contrast-response curve and to impose direction selectivity.

The cortical amplifier's unique characteristics are strikingly highlighted by the persistence of DS in a neuron despite blocking both the neuron's $GABA_A$ and $GABA_B$ receptors (Fig. 4.10d). This is explained by noting that other cortical cells that retain their direction selectivity provide recurrent, excitatory connections to the fiducial neuron. Firm experimental support for this result (Nelson et al., 1994) provides a strong argument in favor of the canonical microcircuit.

The model's DS is relatively invariant with contrast (Fig. 4.7), as observed experimentally (Dean, 1980; Orban, 1984; Li and Creutzfeldt, 1984; Tolhurst and Dean, 1991). In the model, this invariance is dependent on a high enough setting of the

smooth-to-pyramidal $GABA_A$ and $GABA_B$ weights; but especially, it requires smooth neurons' thresholds that are low, to ensure inhibition in the null direction even at low contrasts.

The cortical amplifier model includes many nonlinear elements; nevertheless, it, like the feedforward model, behaves remarkably linearly to grating superposition (Fig. 4.13), similarly to simple cells in area 17 in the anesthetized cat. We discuss this result more in detail in Chapter 6. But the significance of these findings is also that linear summation contributes in our model to direction selectivity to sine wave gratings, in aggreement with physiological data (Reid et al., 1987, 1991; Albrecht and Geisler, 1991; DeAngelis et al., 1993; McLean and Palmer, 1994). Fig. 6.2 in Chapter 6 indicates also that the temporal phase of the response to a stationary grating varies linearly with spatial phase, as expected in a linear model of direction selectivity and measured in striate cortex.

4.9.2 Velocity dependence

Most area 17 cortical neurons are low-pass in velocity and temporal frequency. This behavior must be generated in cortex, since geniculate neurons show very different response properties (Dreher and Sanderson, 1973; Ikeda and Wright, 1975; Movshon et al., 1978; Lee and Willshaw, 1978; Derrington and Fuchs, 1979; Orban et al., 1981a, 1985, 1986; Frishman et al., 1983; Gulyas et al., 1990; Saul and Humphrey, 1992; Maex and Orban, 1992). Moreover, the membrane time constant of cortical neurons is too short to provide this low-pass filtering in a feedforward model (Wörgötter and Holt, 1991).

We confirm the validity of this argument, since the feedforward model's velocity-response is far from being low-pass (Fig. 4.8). In addition, we propose a specific mechanism for the strong response at low velocities, based on our simulations of the

canonical microcircuit. As shown in Section 4.5, the recurrent feedback connections have a far larger gain $G(f)$ at low than at high inputs (Fig. 3.1d), due to nonlinearities in the biophysics of our compartmental models. This nonlinear amplification is responsible for the strength of the model's response at low velocities, rather than a very long network time constant as in Maex and Orban (1992). The response at very low velocities depends much more on feedback strength than the response at higher velocities. A prediction is that experiments that reduce the amount of excitatory cortical feedback to a neuron, such as that done by Grieve and Sillito (1991), should affect neuronal responses preferentially at low velocities, and the velocity-response curve might no longer be low-pass in character (see Fig. 7.4c, Section 7.3.3).

$GABA_A$ feedforward inhibition is responsible for the velocity upper cutoff (Fig. 4.10) by shortening the stimulus duration at velocities above $20°/sec$, leading to a weak response despite the strong LGN input. That inhibition is responsible for the absence of response at high velocities has been hypothesized before (Goodwin and Henry, 1978; Duysens et al., 1985b). As in experimental observations (Duysens et al., 1985a), inhibition overlaps spatially with excitation in the model.

In our model, DS persists down to low velocities ($0.33°/sec$ here), as observed physiologically (Orban et al., 1981b; Orban, 1984; Duysens et al., 1987; Saul and Humphrey, 1992). The model predicts that the ratio of the optimal spatial displacement for DS (Baker and Cynader, 1986) and the $GABA_B$'s time constant should be approximately equal to the lowest direction-selective velocity (see Section 4.6). The optimal spatial displacement for DS corresponds approximately to the spatial displacement between pyramidal and smooth neurons (5′), a small fraction of the Gabor wavelength of a pyramidal neuron's receptive field profile (24′; see Fig. 4.4), as found in cortical neurons by Baker and Cynader (1986).

The small spatial offset in our model means that direction selectivity is generated by very local inhibition within the cortical microcircuitry. Besides being compatible

with the data of Baker and Cynader (1986), this small spatial offset is needed to obtain direction selectivity at the low velocities corresponding to experimental observations (Fig. 4.11), given the biophysical and experimental constraints on $GABA_B$ inhibition's time constant.

DS is relatively independent of velocity in velocity low-pass direction-selective neurons (Orban et al., 1981b; Duysens et al., 1987). In our model, rapid-onset inhibition mediated by $GABA_A$ contributes to DS above $2^o/sec$, while persistent inhibition mediated by $GABA_B$ is exclusively responsible for DS at lower velocities (Fig. 4.10). Indeed, these differential roles of $GABA_A$ and $GABA_B$ in DS lead to specific model predictions. In past experiments (Sillito, 1975, 1977; Baumfalk and Albus, 1988), the influence of velocity has not been tested.

4.10 Conclusions

From the early days of Hubel and Wiesel (1962) until today (e.g., Carandini and Heeger, 1994), it has always been assumed that geniculate input provides the dominant excitatory drive to striate cortex. From an anatomical point of view, given the small number of geniculate synapses on spiny stellate cells, it could be argued that the geniculate input only provides a minor fraction of the excitatory input, the majority originating in neighbouring and recurrently connected cortical cells. As we have shown here, such circuitry, embodied in the *Canonical Microcircuit*, can reproduce in a quantitative manner a host of experimental results pertaining to direction-selective cortical simple cells. Furthermore, our model makes specific predictions that can be tested using current experimental techniques.

Our efforts represent a starting point for explaining other receptive field properties of visual neurons, such as their orientation, disparity tuning, spatial or spatio-temporal separability, within the framework of massive recurrent excitation. Fur-

thermore, a similar network architecture could also be used to explain receptive field properties in other sensory cortical areas. The high degree of cortical interconnectivity raises the possibility that receptive field properties are much less determined by proper wiring of the incoming geniculate input than by collective computation in cortical networks. If true, this would imply that such static concepts as the "center of the receptive field" or the "optimal orientation" might be to a considerable extent dependent on the exact stimulus arrangement and behavioral state of the animal (Allman et al., 1985; Gulyas et al., 1987; Gilbert and Wiesel, 1990; Press et al., 1994; Sillito et al., 1994).

4.11 Summary

Nearly all models of direction selectivity (DS) in visual cortex are based on feedforward connection schemes, where geniculate input provides all excitatory synaptic input to both pyramidal and inhibitory neurons. Feedforward inhibition then suppresses feedforward excitation for non-optimal stimuli. Anatomically, however, the overwhelming majority of asymmetric, excitatory, synaptic contacts onto cortical cells is provided by other cortical neurons, as embodied in the *Canonical Microcircuit* of Douglas and Martin (1991). In this view, weak geniculate input is strongly amplified in the preferred direction by the action of intracortical excitatory connections, while in the null direction inhibition reduces geniculate-induced excitation. We investigate analytically and through biologically realistic computer simulations the functioning of a cortical network based on such circuitry. Here, the network was in the proportional amplification mode, which is present when positive feedback is moderate rather than strong.

The behavior of our network is compared to physiological data as well as to the behavior of a purely feedforward model of DS. Our model explains a number of puz-

zling features of direction-selective simple cells: the small somatic input conductance changes that have been measured experimentally during stimulation in the null direction, the persistence of DS while fully blocking inhibition in a single cell, and that cortical cells are velocity low-pass while their geniculate inputs are velocity tuned. Both model and cells in cat cortex are linear to grating superposition. Finally, we make specific predictions concerning the effect of selective blockade of cortical inhibition on the velocity-response curve.

Chapter 5

Direction selectivity through hysteretic amplification

5.1 Introduction

In this chapter, we investigate the response properties and functioning of the cortical amplifier model in one of its two parameter regimes, hysteretic amplification.

As introduced in Chapter 1, the cortical amplifier model is a circuit that amplifies the geniculate input to cortex in the preferred direction, through excitatory intracortical connections, and cancels geniculate excitation in the null direction through inhibition. We refer you to that chapter for the context of the results presented here.

The detailed model itself and the simulation methods are described in Chapter 2. We describe there the geniculate model we used to provide input to cortex. We refer you to that chapter for these explanations.

The hysteretic amplification mode occurs in the presence of strong positive feedback. We refer you to Chapter 3 for a detailed explanation about these two modes, and to Chapter 4 for a treatment of the other mode, proportional amplification.

First, Section 5.2 gives an overview of the model's basic properties, showing that it indeed amplifies the input strongly, and that in the null direction the model's input conductance changes only slightly, in agreement with intracellular data. Sections 5.3 and 5.4 show the model's responses versus contrast and velocity. Section 5.5 describes for the model the outcome of a linearity test using grating superposition that shows remarkable agreement with physiology. Experimentally testable predictions based on this linearity test are made in Chapter 6. Starting from the theory presented in Chapter 3, Section 5.6 derives simplified dynamics for the model and uses these to explain hysteresis to pulses of current and responses to visual stimuli. The simplified dynamics are also used in Section 5.7 to explain the shape of the contrast-response and velocity-response curves. Finally, Section 5.8 discusses the significance of these results within the context of current knowledge about striate cortex.

5.2 Basic performance

The salient features of the cortical amplifier model's performance in the context of direction selectivity can be seen in Fig. 5.1, which shows the somatic transmembrane potential of a typical model pyramidal neuron during presentation of a bar moving in the preferred (left-to-right direction on Fig. 2.3) and null directions. The pyramidal cell is strongly direction-selective: it generates a burst of spikes in the preferred direction, but none in the null direction. We conclude that the smooth-to-pyramidal weight is large enough relative to the LGN-to-pyramidal weight so that the inhibition completely cancels LGN excitation in the null direction.

In the preferred direction the stimulus reaches the smooth neuron's receptive field after stimulating the pyramidal neurons, so that the spike discharge in the preferred direction is followed by pronounced hyperpolarization, as observed in intracellular recordings from cat visual cortex (Fig. 5.1c; Benevento et al., 1972; Creutzfeldt et al.,

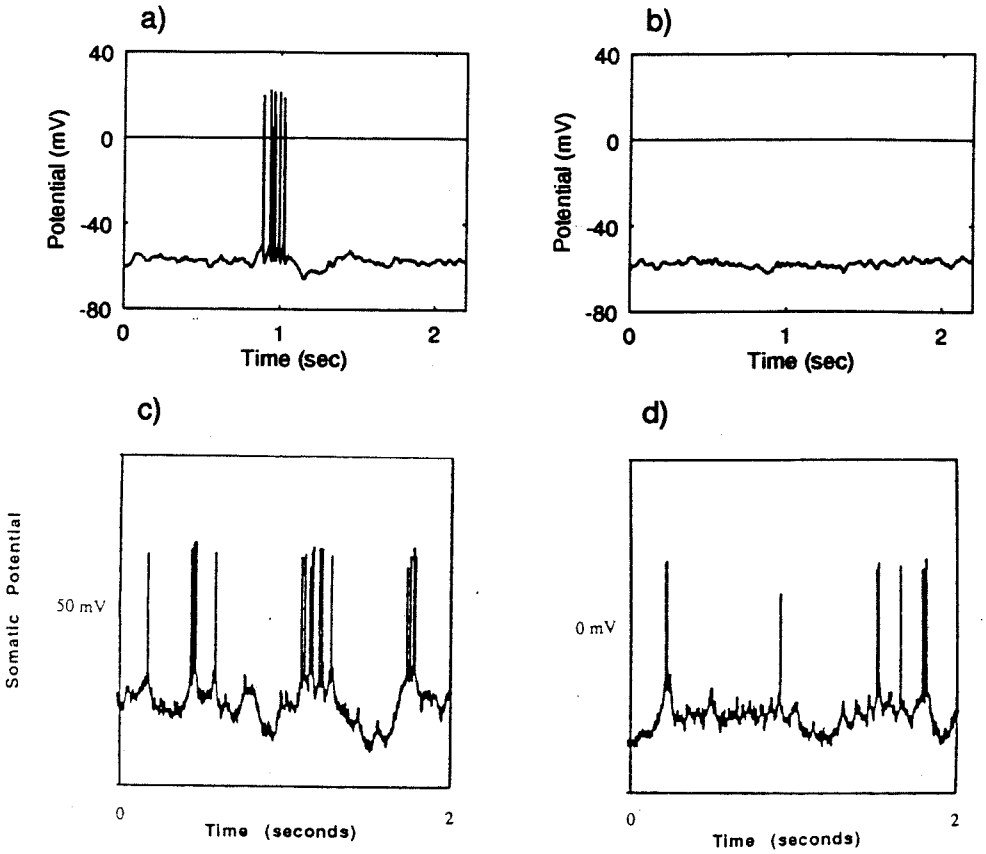

Figure 5.1: **Intracellular membrane potential in the preferred and null directions.** Somatic potential for a pyramidal neuron in the cortical amplifier model in the presence of a 70 % contrast bar moving at $2°/sec$ in the **(a)** preferred and **(b)** null direction. Intracellular recordings from a neuron in primary visual cortex in the anesthetized cat (Douglas et al., 1991) during stimulation by a bar moving at $3°/sec$ in the **(c)** preferred and **(d)** null direction. Note in all conditions the presence of more spikes in the preferred direction than in the null direction. The variablity of the membrane potential in the model originates from spike input from the LGN and the background synaptic noise and current noise.

1974; Ferster, 1988; Douglas et al., 1991). Conversely, during null stimulation, our cortical amplifier feedback model shows only moderate hyperpolarization (Fig. 5.1b), as observed in the recordings from cat cortex (Fig. 5.1d). Indeed, the smooth-to-pyramidal weight is relatively small. It can be that small without a reduction in direction selectivity because the LGN-to-pyramidal weight itself is small.

The response of 50 cortical neurons of the cortical amplifier model to the same stimulus is summarized in the raster plot of Fig. 5.2. For each trial, every horizontal row shows the spikes in one model neuron as dots, with one row for each of 50 model neurons; the first 40 rows are pyramidal neurons, while the last 10 rows are smooth neurons. All pyramidal neurons show strong direction selectivity, while the smooth neurons respond equally in both directions. Some features of the direction selectivity mechanism are apparent from these plots. In the null direction the smooth cells receive LGN input before the pyramidal neurons because the LGN input to the smooth cells is spatially displaced with respect to that of the pyramidal cells: the spatial offset is $5'$ and the bar speed is $2^{o}/sec$, corresponding to a pyramidal neuron delay of about 42 $msec$. Thus, in the null direction, the smooth cells are able to prevent any firing in the pyramidal cells. However, in the preferred direction the pyramidal neurons begin their discharge before the smooth cells and so the cortical amplification loop activates. However, inhibition soon develops, and the pyramidal neurons are silenced.

High signal amplification is achieved within the canonical microcircuit. Fig. 5.3a compares the excitatory recurrent current to a pyramidal cell with the excitatory current induced by the LGN afferents for a bar moving in the preferred direction. Clearly, the dominant excitatory input during response originates from other cortical neurons rather than the LGN. The LGN-to-pyramidal synaptic weight is relatively small; nevertheless, the pyramidal neurons discharge strongly because of the current contributed by the connections between the pyramidal neurons. However, the LGN current is not the input signal being amplified by the network of pyramidal neurons.

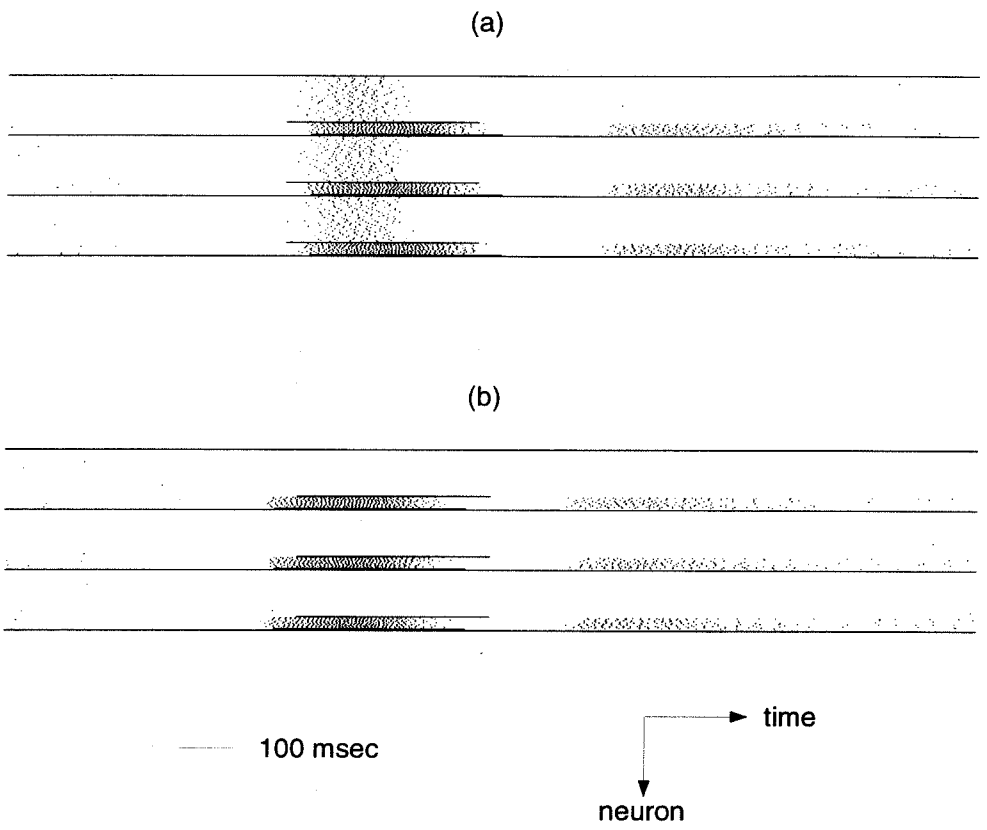

Figure 5.2: **Spike raster plots for the cortical amplifier.** Response of pyramidal and smooth neurons to a 70% contrast bar moving at $2^o/sec$ in **(a)** the preferred and **(b)** the null direction of motion. Three trials are shown for each direction. The first 40 rows in each trace indicate spiking activity in 40 pyramidal cells. The continuous bar just below these rows indicates when the stimulus is within the receptive fields of the LGN inputs to the pyramidal cells. The 10 rows below the bar correspond to firing activity in 10 smooth cells. Note the strong direction selectivity of the pyramidal neurons, whereas the smooth neurons are not direction-selective. There is spontaneous activity in the smooth cells, while it is essentially absent in the pyramids.

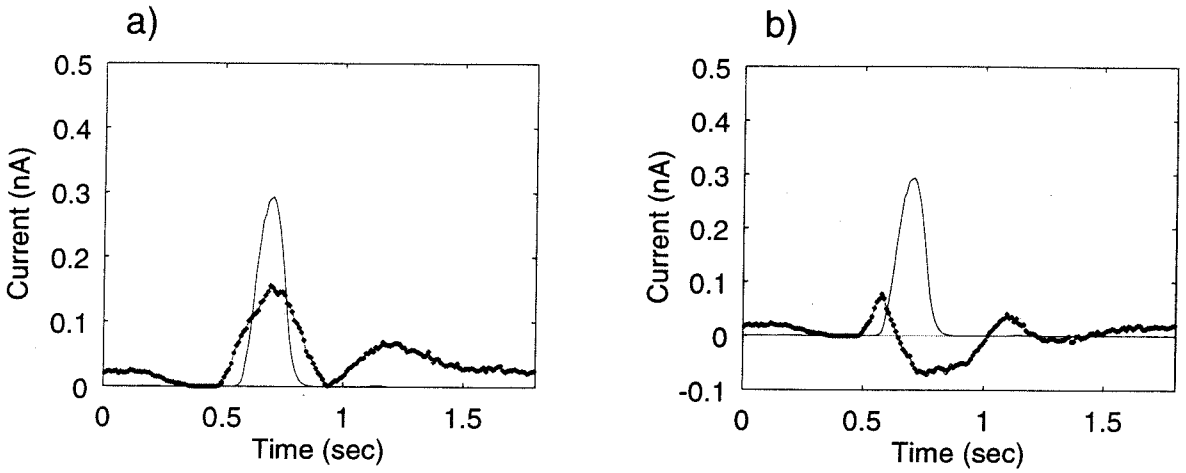

Figure 5.3: **Current amplification in the preferred direction in the cortical amplifier.** **(a)** Excitatory cortico-cortical current (light line) compared to that arriving from the LGN afferents (bold line), for a pyramidal neuron of the cortical amplifier model during stimulation by a 70% contrast bar moving at $2^o/sec$ in the preferred direction. The time course of the geniculate current is essentially given by the passage of the bar over the ON portion of the single subfield. The cortical current is larger than the geniculate current. **(b)** Same excitatory cortico-cortical current as (a)(light line) compared to the **net** input current (bold line), defined as the difference between the excitatory current due to the geniculate input and the combined ($GABA_A$ plus $GABA_B$) inhibitory currents to the pyramidal neuron. The net input current is strongly amplified by the intracortical connections, with a delay of about 150 msec.

Instead, the total input signal to the pyramidal neurons is the LGN input current minus the total inhibitory current contributed by all smooth neurons: the **net input current**. This current is shown together with the LGN current in Fig. 5.3b, for the same stimulus as Fig. 5.3a. At rest, the LGN background activity is responsible for some positive net input current (about 0.02 nA). As the stimulus enters the surround of the LGN neurons, their spontaneous response is inhibited, reducing the net input current to zero. When the stimulus enters the center portion of the LGN neurons, the net current quickly increases to about 0.075 nA. As the LGN input fields of the smooth neurons overlap with those of the pyramidal neurons, inhibitory current from the smooth neurons quickly reduces the net current to -0.08 nA. Subsequently, the net current first increases due to rebound when the stimulus leaves the pyramids' surround, then goes negative with rebound from the smooth neurons' surround, before reverting to its spontaneous background value. The real amplification factor achieved by the canonical microcircuit is much larger than suggested in Fig. 5.3a: it is about 3.9 in Fig. 5.3b. Inhibition is necessary for direction selectivity, but strongly reduces the input current even in the preferred direction; fortunately, amplification by the canonical microcircuit amplifies strongly the remaining input.

In the weak LGN input lies the key to some very puzzling experimental findings. Direct measurements of somatic input conductance in cat area 17 neurons during stimulation by nonpreferred stimuli show very small conductance changes, less than 25% (Douglas et al., 1988, 1991; Pei et al., 1991; Ferster and Jagadeesh, 1992). Having a weak LGN input to the pyramidal neurons allows the network to be highly direction selective despite relatively weak inhibition. Such weak inhibition does not lead to large increases in the somatic input conductances during null direction stimulation, as shown in Fig. 5.4 (the peak change is 60% over baseline). In contrast, a model that would not include excitatory cortical feedback would show much larger conductances changes in the null direction (see Section 4.2), and so is not compatible with this

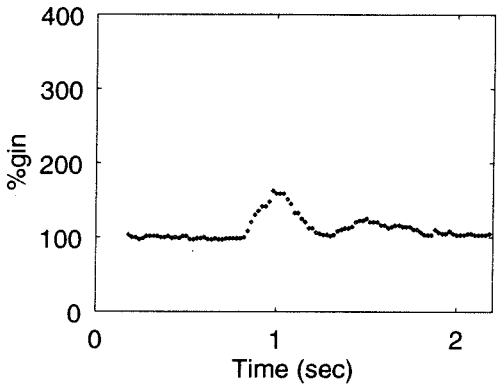

Figure 5.4: **Somatic conductance changes during null direction motion.** Shown is the percent change in somatic input conductance as a function of time for a direction-selective pyramidal neuron in the hysteretic amplifier model during stimulation by a bar moving in the null direction. The input conductance is computed as discussed in Section 2.6. The small excitatory input from the LGN afferents can be inhibited by a small inhibitory input, requiring only a moderate conductance increase, 60% over baseline. Experimental data shows no measurable changes in the input conductance. The cortical amplifier model is in much closer agreement to the experimental data than the feedforward model, where the input conductance increases several times over baseline (see Fig. 4.6).

experimental data.

We have seen that the cortical amplifier is direction selective for one stimulus condition (a high contrast, moving bar). We will now explore more systematically how directionality depends on contrast and velocity.

5.3 Contrast dependence of response and directionality

Fig. 5.5 shows contrast-response curves in the model for both LGN and pyramidal neurons. The LGN contrast-response curve (Panel 5.5a) has a slope that is less than 1 on a log-log plot and compares well with experimental data in retina and LGN showing a compressive nonlinearity (Shapley and Perry, 1986; Saul and Humphrey, 1990). Panel 5.5b compares the pyramidal response with a sample experimental contrast-response curve and reveals considerable agreement. Both have an initial portion that is relatively linear on a log-log scale with slopes that are much larger than the LGN's: they are 2.87 and 3.77 decade Hz/decade % contrast for the model and cortical neuron, respectively. Since these slopes are larger than one, the initial portions of both contrast-response curves increase faster than linearly. This expansivity is a general feature of neurons in visual cortex. Albrecht and Geisler (1991) have fitted the initial portion of neuronal contrast-response curves with a power function and have found an average exponent of 2.5, comparable to the model's slope.

The model contrast-response curves shows abrupt saturation following the curve's initial steep portion. This is a usual feature of contrast-response curves in primary visual cortex (Albrecht and Hamilton, 1982; Albrecht and Geisler, 1991), but it is not observed in both model and actual retinal and LGN neurons.

The model pyramidal neurons respond very little in the null direction, and the

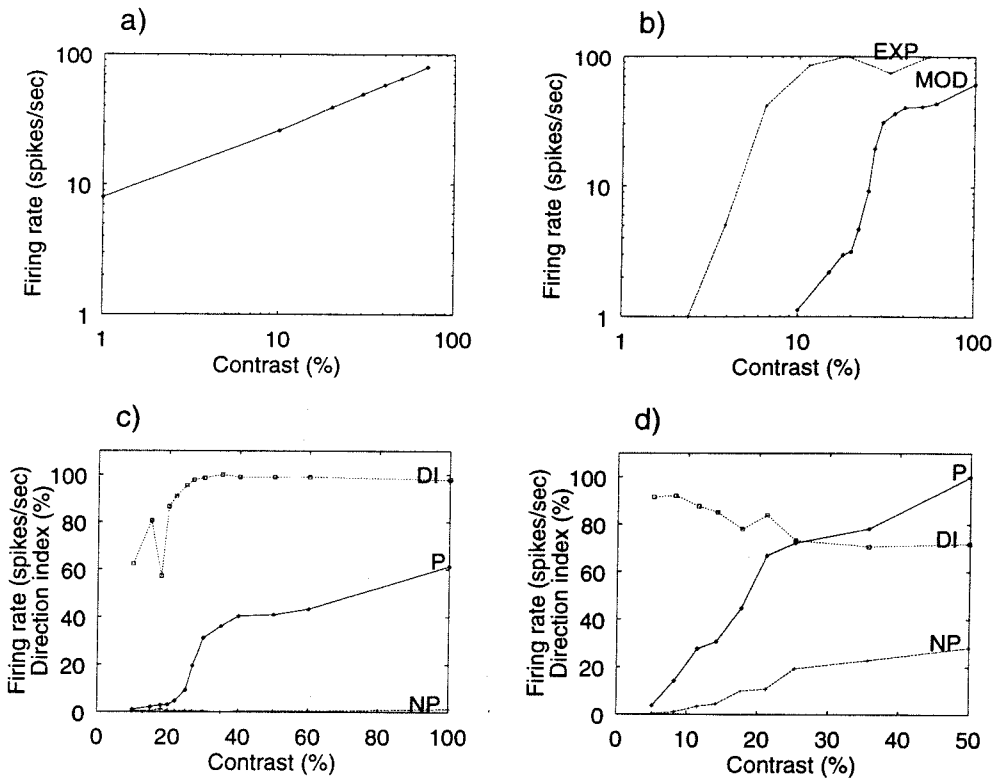

Figure 5.5: **Contrast-response curves.** Relationship between the visual contrast (eq. 2.2) of a moving sinusoidal grating (1 Hz, 1 c/deg) and the peak firing rate for different stages in our model, compared to physiological data (see Section 2.6). **(a)** Peak geniculate response given by the Victor (1987) model. **(b)** The amplitude of the first Fourier harmonic component from a cortical neuron in cat area 17 (label EXP; adapted from Albrecht and Hamilton, 1982) compared to the response in the preferred direction for pyramidal neurons in the cortical amplifier model (MOD). The next two panels show the response in the preferred (P) and null direction (NP) of motion as well as the direction index ($DI = (P - NP)/P$; eq. 2.5) for pyramidal neurons in the **(c)** cortical amplifier model as well as **(d)** for a simple cell in cat area 17 (responding to a 2 Hz drifting sinuosidal grating; adapted from Tolhurst and Dean, 1991). Both model and cat cortical neuron are direction selective over the full range of contrasts.

direction index is between 80 to 100% for nearly all contrast values (Fig. 5.5e). The invariance of the direction index over a broad range of contrast is characteristic of visual cortical neurons (Fig. 5.5e; Dean, 1980; Orban, 1984; Li and Creutzfeldt, 1984; Tolhurst and Dean, 1991). Over 20% of area 17 neurons (and in particular, area 17 simple cells) have direction indices at the optimal velocity between 80 and 100% (Albus, 1980; Berman et al., 1987; Gizzi et al., 1990; Reid et al., 1991; Tolhurst and Dean, 1991; DeAngelis et al., 1993; McLean and Palmer, 1994).

5.4 Velocity dependence of response and directionality

A strong test of any model of direction-selective cells in area 17 is whether model neurons are *velocity low-pass*, as are 63% of area 17 cortical neurons (Fig. 5.6e; Orban et al., 1981a; Orban, 1984). These neurons respond very well to low velocities and little to velocities above $20^{o}/sec$. This property does not originate from LGN neurons, which have tuned, band-pass velocity-response curves with strong responses at high velocities (Fig. 5.6b; Dreher and Sanderson, 1973; Lee and Willshaw, 1978; Frishman et al., 1983; Orban et al., 1985; Gulyas et al., 1990). A further test is the extent to which direction selectivity persists over a wide range of velocities; indeed, velocity low-pass cells usually have a flat DI-velocity relationship (Orban et al., 1981b; Orban, 1984).

Model LGN neurons have physiologically plausible velocity-response curves (Fig. 5.6a). In contrast, the cortical amplifier's velocity-response curve is very different (Fig. 5.6c), but is similar to area 17 velocity low-pass neurons: its response barely shows any decrease at very low velocities, but drops off by more than 50% for velocities above $20^{o}/sec$.

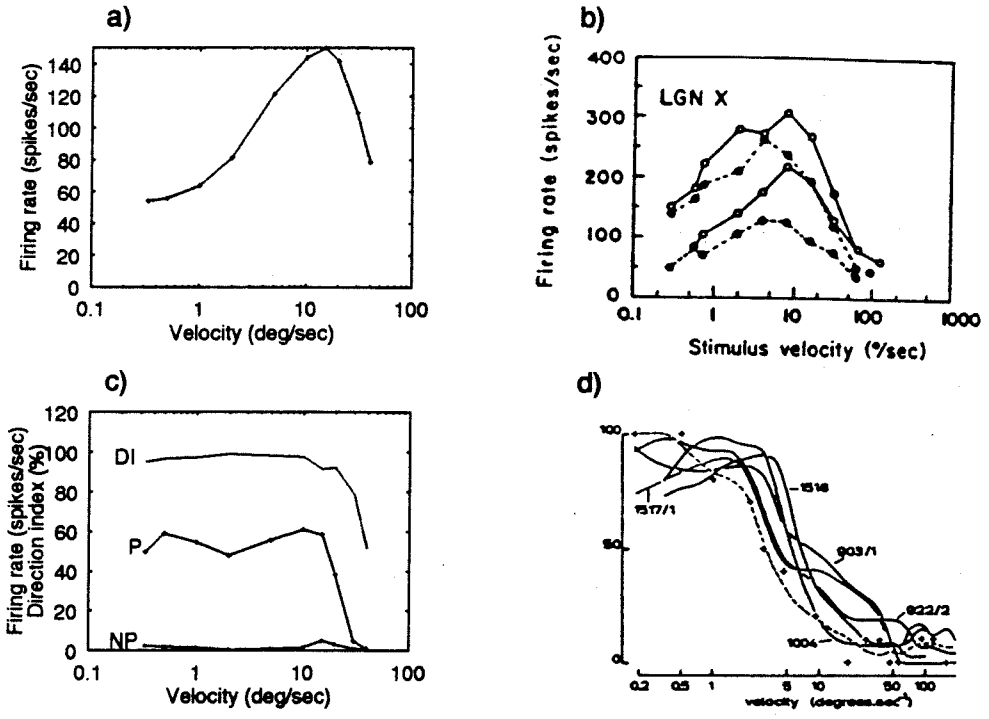

Figure 5.6: **Velocity-reponse curves.** Shown is the peak firing rate for a 70 % contrast bar as a function of its velocity at different stages in our model, compared to physiological data. **(a)** LGN model peak response given by the Victor(1987) model. **(b)** Peak response of X geniculate cells in the adult, anesthetized cat (Frishman et al., 1983). **(c)** Peak response in the preferred (P) and null direction (NP) of motion as well as the direction index ($DI = (P - NP)/P$; eq. 5) for pyramidal neurons in the cortical amplifier model. Model neurons are direction selective over two orders of magnitude of speed. **(d)** Representative examples of velocity-response curves from velocity low-pass cells in cat visual cortex (Orban, 1984, Fig. 8/5 C).

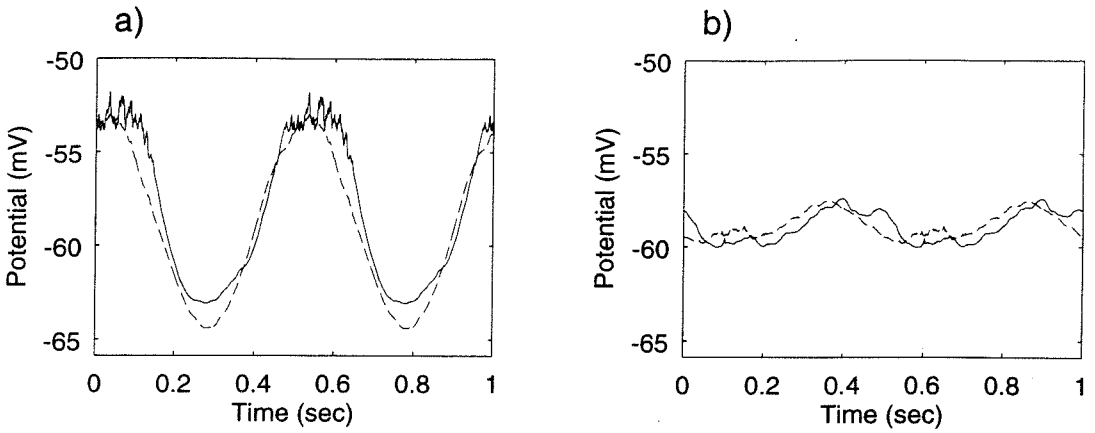

Figure 5.7: **Grating superposition test.** Comparison between the modulations in membrane potential evoked (continuous) by 1 *cycle/deg*, 70% contrast sine wave grating, drifting in two directions at 2 *Hz* ($2^o/sec$), and the response predicted (dashed) from summing stationary contrast-reversal gratings, for one cell in the cortical amplifier model. Each trace is an average of the response to 57 grating cycles, and shows two copies of the average response to one grating cycle side by side. **(a)** Preferred and **(b)** null direction. Superposition holds, as in cat simple cells (Jagadeesh et al., 1993).

Similarly to velocity low-pass neurons, the cortical amplifier model's dependence of direction index (DI; see Section 2.6) on velocity is relatively flat over two orders of magnitude, reflecting the small response in the null direction at all velocities. The Mean Direction Index (MDI; see eq. 2.6, Section 2.6) is 95.7%. This invariance depends on the presence of both transient ($GABA_A$) and sustained ($GABA_B$) inhibition, and on the small spatial offset between pyramidal and inhibitory neurons, as discussed in detail in Chapter 4; $GABA_A$ and $GABA_B$ are responsible for direction selectivity at high and low velocities, respectively.

5.5 Linearity to superposition

Ferster and his colleagues (Jagadeesh et al., 1993) carried out an elegant set of intracellular experiments in direction-selective simple cells. They showed that the (somatic) membrane potential signal evoked by a drifting sinusoidal grating can be predicted

from the linear sum of responses to stationary contrast-reversal gratings at several spatial phases, seemingly implying a simple linear feedforward model of direction-selective simple cells. The reader is referred to Section 2.6 for a detailed description of this test.

In the preferred and null directions, the average membrane potentials could be predicted with an accuracy comparable to the experimental results (Fig. 5.7; see Jagadeesh et al., 1993). Furthermore, there was no need to adjust any parameters specifically to obtain the fit. This result is surprising in view of the importance of amplification for the model's functioning, and the nonlinearity of this amplification (see Discussion); Chapter 6 explains in detail why the linearity test holds despite nonlinear amplification.

5.6 Simplified dynamics: response through hysteresis

We now seek to understand the shape of the contrast-response and velocity-response curves of pyramidal cells in the model. Both curves are very different from those of model LGN neurons. In Section 3.4 we have examined the steady-state responses of the hysteretic amplifier, and have found that its action is nonlinear amplification. However, moving bars and gratings are transient stimuli; to understand the response curves, we must understand how reaching the equilibrium firing depends on the contrast or velocity of a bar or grating. This depends for instance on the duration of the stimulus compared to the network's time constant. So we will now study the cortical network's dynamics and responses to transient stimuli.

A good starting point for understanding the hysteretic amplifier's response to transient stimuli is the response sequence shown in Fig. 3.2. We can understand the

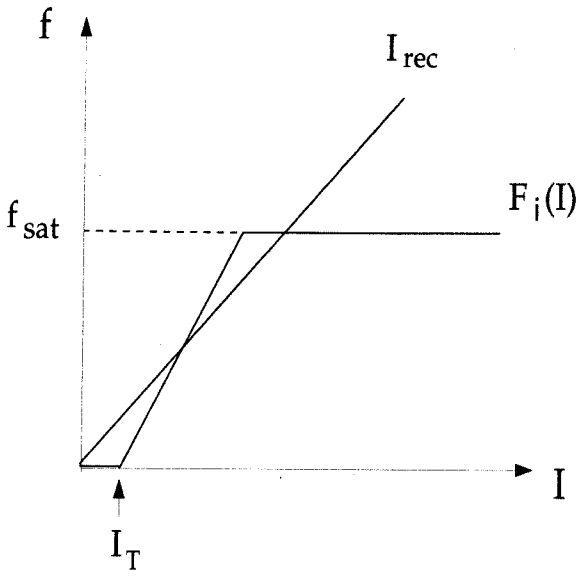

Figure 5.8: **Simplified representation of the cortical amplifier model.** By using a linear recurrent current function I_{rec} and a current-discharge curve F_i that has a threshold I_T, then is linear up to saturation at a firing rate f_{sat}, we can obtain a situation that is similar to the cortical amplifier model, where there are two equilibrium firing rates or attractors in the absence of any input, one at 0 Hz, the other at a high firing rate, in this case f_{sat}.

dynamics analytically by considering a simplified system with F_i and I_{rec} functions that are similar to the cortical amplifier model's (Fig. 5.8). In this system, I_{rec} is linear, while F_i is linear up to saturation, corresponding to the equations:

$$F_i(I) = \begin{cases} 0 & I < I_T \\ k_{F_i}(I - I_T) & I_T < I < I_{sat} \\ f_{sat} & I > I_{sat} \end{cases} \tag{5.1}$$

and

$$I_{rec}(f) = k_{rec} f \,. \tag{5.2}$$

As mentioned in Section 3.4, and to mimick the condition depicted in Panel 3.3b, we have the additional constraint in the hysteretic amplifier model:

$$k_{F_i} > \frac{1}{k_{rec}} \tag{5.3}$$

Neglecting the membrane time constant, the system can be described by the following differential equation as long as $0 < f < f_{sat}$ (see Section 3.5):

$$\tau_{syn} \frac{df}{dt} = (\alpha - 1) f + k_{F_i}(I_l - I_i - I_T) \tag{5.4}$$

where τ_{syn} is the decay time constant for the excitatory synaptic conductance change (20 $msec$), $\alpha = k_{F_i} k_{rec}$ is the slope of the $F(f)$ corresponding to F_i and I_{rec} (see eq. 3.1), I_l and I_i, the (possibly time-dependent) LGN and inhibitory currents. As soon as $f = f_{sat}$, eq. 5.4 is valid only if the right-hand side is negative. Otherwise, df/dt is 0. Similarly, if $f = 0$, the equation is valid only if the right-hand side is positive; otherwise, df/dt is 0 again. Note that α is greater than one, given equation 5.3.

We can now examine the responses of such a system to a sequence of inputs similar to that shown in Fig. 3.2; since the simplified model is similar to the cortical

amplifier model, its responses will be similar, too, and will explain the detailed model's behavior. As in Fig. 3.2, we assume initially that the system is at rest: $f = 0$. Since initially there is no input ($I_l = 0$, $I_i = 0$) and the threshold is positive nonzero ($I_T > 0$), the right-hand side of eq. 5.4 is negative and the network's firing remains 0. This observation explains why the cortical amplifier model does not always discharge at a high rate in the absence of any input.

As soon as a constant positive suprathreshold input is given, *i.e.*:

$$I_l > I_T\,, \tag{5.5}$$

the right-hand side becomes positive; since the coefficient in front of f is positive, the impulse response of the system is an exponential with a positive exponent (see Section 3.5):

$$e^{t/\tau_{net}}\,, \tag{5.6}$$

where $\tau_{net} = \tau_{syn}/(\alpha - 1)$. So the response to a constant input will be an exponential with a positive exponent; for an input starting at $t = 0$:

$$f = k_{F_i}(I_l - I_T)\tau_{net}e^{t/\tau_{net}}\,. \tag{5.7}$$

If the input is presented long enough, the system reaches f_{sat}, and remains at this firing rate.

If the positive input is now withdrawn ($I_l = 0$), the right-hand side of the equation does not become negative, again since the coefficient in front of f is positive. So the firing rate does not decrease; instead the system stays at f_{sat} ! This is the explanation for the hysteretic behavior of the cortical amplifier: firing persists despite withdrawal of the input that initially caused the firing.

However, if we now present a constant negative input large enough for the right-

hand side to become negative, *i.e.*:

$$k_{F_i}|I_i + I_T| > (\alpha - 1)f\,, \tag{5.8}$$

the firing rate will decrease according to an exponential with the same positive exponent as previously, until the discharge rate reaches 0. If we bring the input back to 0, the right-hand side of eq. 5.4 stays negative and the firing rate remains 0. Although the network will generally keep discharging after a positive input, applying inhibition resets the system to a low firing rate.

We conclude that the simplified system described by eqs. 5.1, 5.2, and 5.4 explains the cortical amplifier's hysteretic behavior as presented in Fig. 3.2. Hysteresis comes from the switching between two separate attractors (equilibrium firing rates) in the cortical amplifier model, one at 0 Hz, the other at a high firing rate. Switching from the lower to the upper occurs in the presence of a large enough positive input, while the converse results from a large enough negative input.

The cortical amplifier's responses to visual stimuli rely on principles similar to those illustrated in Fig. 3.2. At a first glance, it is puzzling that the model's discharge does not persist after withdrawal of a visual stimulus, such as the bar moving in the preferred direction shown in Fig. 5.2. However, excitatory input from the LGN is followed by inhibition from the smooth neurons, as shown previously for a bar in Fig. 5.3b, before reverting to its spontaneous background value. Clearly, a short pulse of LGN input is followed by a pulse of inhibition, similarly to Fig. 3.2. Therefore, as in that figure the initial excitation nudges the cortical network to its high firing attractor, and the subsequent inhibition resets the network to its low firing attractor. Furthermore, hysteresis can be observed directly in the response to the moving bar. Indeed, the pyramids' response does not start decreasing as soon as the net input current starts decreasing. Instead, it is still increasing, and only decreases when the

net input current becomes substantially negative.

Note, however, that although the principles underlying both simplified and detailed models are similar, there are also differences. In the simplified model the slope of $F(f)$ is constant (equal to α) and larger than 1, while in the detailed model the slope varies and is only initially larger than 1 (Fig. 3.4b). Therefore, the approach to the upper attractor follows an exponential with a positive exponent only initially. Closer to the attractor, the dynamics slow down substantially, as can be seen in Fig. 3.2.

5.7 Analysis of the contrast-response and velocity-response curves

The contrast-response curve has a sigmoid shape with a steep maximum slope, followed by quite abrupt saturation. In contrast, the LGN input increases much more proportionally to contrast (Fig. 5.5b). We can understand these differences in terms of the hysteretic behavior of the cortical amplifier model.

The peak firing rate will not increase much with contrast as long as the LGN's synaptic input current is smaller than the threshold of the current-discharge curve. As soon as the contrast is large enough for that limit to be exceeded, the network switches quickly to the high firing rate attractor, according to an exponential with a positive exponent (eq. 5.7), resulting in the steep slope observed in the contrast-response curve. The positive exponent even explains the expansivity in the initial portion of that slope; indeed, increasing contrast also increases the duration when the net input current (see Fig. 5.3) is larger than the threshold of the current-discharge curve (I_T), increasing the duration of exponential growth of firing rate, and therefore increasing the peak firing rate in the contrast-response curve exponentially too.

At high contrasts, the system reaches the upper attractor at the peak discharge. The attractor's firing rate will not change much with the input strength, because the slope of the transfer function $F(f)$ is small at the attractor (Fig. 3.4b). This results in the relatively small slope of the contrast-response curve at high contrasts. This is also reflected in the shallow slope of the steady-state response as a function of the constant input current (Fig. 3.4c).

Between the two shallow portions of the curve, the slope is rather steep. However, there is a small but sizable range of contrasts for which the system's response is intermediate. So, although the response is not strictly proportional to contrast, for an interval of contrasts the response is graded. This relative gradedness depends on the dynamics of switching from lower to upper attractors. If the dynamics were very fast, compared to the time available for switching, as soon as a given contrast results in a suprathreshold LGN input current, the network would switch to the upper attractor; the peak response would never be in the range intermediate between the two attractors. The gradedness depends on the time constant of these dynamics being rather similar in value to the time available for switching. The time that is available for the network to switch is the period from when the input is suprathreshold (eq. 5.5) to when inhibition is large enough to reset the network (eq. 5.8). Assuming that these two values are close to 0, this period is approximately equal to the time interval from when the stimulus enters the receptive field of the pyramids to when it enters that of the smooth cells. Given that the spatial offset between the two cortical neuron groups is 5′, this duration will be about 80 *msec* for a grating moving at 1 deg/sec, which is the stimulus used for the contrast-response. The time constant of the network dynamics is $\tau_{syn}/(\alpha - 1)$; the average slope α of the $F(f)$ curve over the first four points in Fig. 3.4b is 1.16, so that an estimate of the network's initial time constant is 120 *msec*. It is not very different from the duration available for switching, explaining that the slope of contrast-response curve is not too steep, but

that nevertheless within the limited time available the network's firing nears that of the upper attractor.

We conclude that we explain the three segments observed in the contrast-response curve: the initial slow increase below threshold, the steep rise, and the shallow portion when the high rate attractor is reached.

The most striking aspect of the velocity-response curve is the constancy of the peak response at low and intermediate velocities. This constancy occurs despite large variations in firing rates of the LGN input (Fig. 5.6). As for the contrast-response curve, this constancy is explained by the existence of an attractor with a high firing rate. As long as the attractor firing rate is reached, the input will not have much of an influence on the network's discharge rate. However, the duration of the net current's positive phase is inversely proportional to velocity, and at high velocities the input does not last long enough, and the system does not reach the higher attractor. So the constancy of peak firing rate disappears at higher velocities.

Invariance of the response with velocity is also enhanced by the increased duration of the LGN input at low velocities. Although the LGN input decreases with decreasing velocity, the network has no trouble reaching the high firing attractor because of the increased duration.

5.8 Discussion

The *canonical microcircuit* (Fig. 1.1b) embodies compelling anatomical observations showing massive excitatory cortico-cortical feedback connections among spiny stellate and pyramidal cells in mammalian visual cortex (Berman et al., 1992; Peters and Payne, 1993; Ahmed et al., 1994; Peters et al., 1994). Physiological support derives primarily from intracellular recordings in response to electrical pulse stimulation of cortical afferents (Douglas and Martin, 1991) and from pharmacological

blockade experiments (Grieve and Sillito, 1991). The role of the present chapter is to examine some of the computational principles underlying the operation of this recurrent excitation and its implications on response properties of cortical circuits, within the context of a realistic simulation of the dynamics of a small set of cortical neurons, operating in the hysteretic amplification mode. We have called this model the *hysteretic amplifier* model.

Indeed, there are two operating modes of this cortical amplifier circuit, depending on parameter values. In the first mode, the pyramidal neurons' response increases proportionally to the stimulus strength over a substantial range of contrasts, before saturating. We examine in Chapter 4 operation in this mode, which we call *proportional amplification.* In the second mode, the response increases much faster over a narrow range of contrasts, then saturates. We study this parameter regime in detail in this chapter.

Analytically, one can define a steady-state transfer function for the network of pyramidal neurons ($F(f)$, see eq. 3.1). In the proportional amplification mode, the transfer function has a slope (corresponding to α in the linear case, see eq. 5.4) that is less than 1. However, for the model presented in this chapter, the slope at low firing rates is larger than 1 (Fig. 3.4); then, there are two attractors or equilibrium firing rates without any input to this system, one with a firing rate at or close to 0 Hz, the other with a high firing rate (Figs. 3.3b and 5.8). Since the slope of the transfer function $F(f)$ is the product of the current-discharge curve's slope and the recurrent current function's slope (equation 3.1), if we increase the steepness of either of these functions in a model that is in the proportional amplification mode, we will transform it into the present model. In particular, increasing the strength of the connection between the pyramidal neurons will increase the slope of the recurrent current function.

The existence of the high rate attractor has a strong influence on the response

properties of the model. The steep slope in the contrast-response curve corresponds to when the network is switching quickly between the two attractors. Even the expansivity in the initial portion of that steep rise results from the dynamics. Saturation at high contrasts corresponds to when the network has reached the attractor firing rate, which does not depend very strongly on the input. Constancy of response with velocity up to high velocities also occurs because of the attractor.

It is striking that these features of contrast-response and velocity-response curves have all been clearly observed experimentally in primary visual cortex and have not been explained previously in a single consistent framework. An explanation is clearly needed since these properties are not present in retinal and LGN neurons. In a purely feedforward model, where excitatory synaptic input comes only from the LGN, none of these properties can be explained (Chapter 4). Although Albrecht and Geisler (1991) base their predictions of direction indices on expansivity of the contrast-response curve, similarly to DeAngelis et al. (1993) and Heeger (1993), a detailed explanation for its origins has not yet been proposed. Saturation at high contrasts is a prominent feature of most neurons, and several explanations have been advanced, including a contrast-set gain control mechanism (see for instance Albrecht and Geisler, 1991; Heeger, 1992). The velocity-response curves of most area 17 cortical neurons are velocity low-pass and often show remarkable constancy at low velocities (Orban et al., 1981a; Orban, 1984). Local excitatory cortical feedback operating in the mode described in this paper straightforwardly explains these properties in a unified framework. Especially, the shape of the contrast-response curves seen in cortex appears very suggestive of this mode of operation. Furthermore, massive local excitatory connections are prominent in cortex. The present model is consistent with the linearity test of Jagadeesh et al. (1993). We show also that a model based on excitatory feedback explains the small changes in conductance demonstrated in direction-selective cortical neurons in the null direction (Douglas et al., 1988; Berman et al., 1991; Pei

et al., 1991; Ferster and Jagadeesh, 1992), as well as the persistence of direction selectivity in experiments where inhibition is blocked in a single neuron (Nelson et al., 1994). Taken as a whole, these are strong arguments in favor of the present model.

A particularly intriguing aspect of the model is the possible occurrence of hysteresis when the model switches between two attractors. Hysteresis is characterized by the persistence of a high discharge rate despite withdrawal of the initial stimulus, as the network remains at the upper attractor (Fig. 3.2). This has not been observed in primary visual cortex. However, we have noted that for a moving stimulus the excitatory discharge is always followed by activation of the smooth cells, and inhibition resets the network to the lower attractor. Furthermore, withdrawing a stimulus flashed on in an ON subfield of a simple cell in primary visual cortex results in inhibition, most likely originating from activation of the OFF system and feedforward inhibition in cortex, and would reset the network. We conclude that attractor dynamics could very well underlie cortical information processing, even though hysteresis has not been observed experimentally.

Our model's behavior parallels observations and proposals relating to short-term memory in infero-temporal cortex. Fuster and colleagues have observed in this portion of visual cortex patterns of persistent firing during memory tasks (Fuster and Jervey, 1980, 1982; Fuster, 1990). Models of these phenomena have been proposed, also based on intracortical excitatory feedback and attractor dynamics (Zipser et al., 1993; Amit et al., 1994).

Experiments have shown that saturation of contrast-response curves is not related to hard saturation of the neuron's spike mechanism. Indeed, when spatial frequency or direction of motion are varied (Albrecht and Hamilton, 1982; Tolhurst and Dean, 1991), the shape of the contrast-response curves remain invariant while the saturation firing rate varies. The present model is in principle consistent with these findings. Indeed, the spike mechanisms of neurons in the model are not saturated at the at-

tractor frequency (Fig. 3.4). Furthermore, the attractor firing rate depends directly on the recurrent current, and could be modulated by changing the effective strength of connections by inhibition (Heeger, 1992) or any other mechanism. In Section 7.3, we show that changing the inhibition or feedback strength by small amounts in the present model can lead to changes in the saturation firing rate of the contrast-response curve.

We conclude that the canonical microcircuit's local excitatory connections can explain a range of cortical properties when combined with attractor dynamics. In such models, hysteresis is theoretically possible, but is not observed for visual stimuli because excitation is followed after stimulus withdrawal by inhibition that resets the network to a low firing rate.

5.9 Summary

Almost all models of orientation and direction selectivity in visual cortex are based on feedforward connection schemes, where geniculate input provides all excitation to both pyramidal and inhibitory neurons. The latter neurons then suppress the response of the former for non-optimal stimuli. However, anatomical studies show that up to 90% of the excitatory synaptic input onto any cortical cell is provided by other cortical cells. The massive excitatory feedback nature of cortical circuits is embedded in the *canonical microcircuit* of Douglas and Martin (1991). We here investigate analytically and through biologically realistic simulations the functioning of a detailed model of this circuitry, operating in a *hysteretic* mode. In the model, weak geniculate input is dramatically amplified by local intracortical excitation, while inhibition has a dual role: (i) to prevent the early geniculate-induced excitation in the null direction and (ii) to restrain excitation and ensure that the neurons fire only when the stimulus is in their receptive-field. The model relies on the presence of an attractor at a high

firing rate; strong discharge occurs when the network switches to this attractor. This paper complements the previous chapter that describes a similar model operating in the *proportional amplification* mode. The present mode of operation is compatible with several important findings from that chapter. In addition, response invariance with velocity that has been observed in velocity low-pass neurons can be explained by the presence of the attractor. The model also allows us to understand the origin of expansive and compressive nonlinearities in the contrast-response curve of striate cortical neurons. Surprisingly, the model postulates that hysteresis is latent in striate visual cortex and underlies some aspects of the responses, paralleling recent proposals for short-term memory.

Chapter 6

Linearity to grating superposition does not imply linearity of the underlying biophysics

6.1 Introduction

This chapter is about the intracellular grating superposition test of linearity used by Jagadeesh et al. (1993) on direction-selective cells. We provide a detailed explanation of the cortical amplifier model's linearity to this test and explore the test's methodology.

A fundamental question about information processing in primary visual cortex is whether simple cells sum their spatial and temporal inputs linearly. Many experiments have attempted to answer this question (Ferster, 1987; Jones and Palmer, 1987; Ferster and Jagadeesh, 1992; McLean and Palmer, 1994; see Shapley and Lennie, 1985 for a review), with some focusing on linearity of direction selectivity (Palmer and Davis, 1981; Reid et al., 1987, 1991; Albrecht and Geisler, 1991; DeAngelis et

al., 1993; McLean et al., 1994). An especially detailed investigation has tested in direction-selective simple cells the linearity of modulations in intracellular potential induced by gratings (Jagadeesh et al., 1993), and has concluded that the mechanism of direction selectivity is linear summation of synaptic potentials without any need for nonlinear processes.

This conclusion seems at odds with the existence of nonlinear processes in dendritic trees, such as synaptic nonlinearities and voltage-dependent mechanisms (see Mel, 1994 for a review), which could substantially enhance the computational power of a single neuron. Furthermore, strict linearity would require elaborate processes to compensate exactly for the many stages of half-wave rectification (in the retina and lateral geniculate nucleus - LGN) prior to integration of inputs in cortex.

Such linearity would also appear to argue against the cortical amplification process embodied in the *Canonical Microcircuit* of neocortex (for a description, see Chapter 1). Amplification must be nonlinear, since it requires action potentials in the cortical neurons, and so occurs only if the membrane potential exceeds a certain threshold voltage; thresholding is inherently nonlinear.

In this chapter, we evaluate whether these nonlinearities are incompatible with the data of Jagadeesh et al. (1993), through detailed computer simulations of the cortical amplifier model (here in the proportional amplification mode, but the same holds for the hysteretic amplifier), and the feedforward model, a strictly feedforward version of this model.

As introduced in Chapter 1, the cortical amplifier model is a detailed simulation of a circuit that amplifies the geniculate input to cortex in the preferred direction, through excitatory intracortical connections, and cancels geniculate excitation in the null direction through inhibition. We refer you to that chapter for the context of this model.

The proportional amplification mode occurs in the presence of moderate positive

feedback. We refer you to Chapter 3 for a detailed explanation about the two modes of operation, and to Chapters 4 and 5 for a thorough description of response properties and functioning in both modes.

The proportional amplifier and feedforward models themselves and the simulation methods are described in Chapter 2. We describe there the geniculate model we used to provide input to cortex. We refer you to that chapter for these explanations.

The linearity test of Jagadeesh et al. (1993) is based on intracellular experiments in direction-selective simple cells. They showed that the (somatic) membrane potential signal evoked by a drifting sinusoidal grating can be predicted from the linear sum of responses to stationary contrast-reversal gratings at several spatial phases. The reader is referred to Section 2.6 for a detailed description of this test.

We find that both detailed models conform to the linearity test mentioned above (Jagadeesh et al., 1993). To understand why these models satisfy the linearity test, despite the nonlinearities present in the biophysics, we introduce and simulate a series of simplified models that capture the essential nonlinearities of the detailed models. In addition, we introduce a modified grating superposition test that detects the models' nonlinearity. Our results challenge the interpretation that the observations of Jagadeesh et al. (1993) reflect the fundamental linearity of neuronal operations, rather than system and stimulus related properties.

6.1.1 Guided tour

Section 6.2 demonstrates the models' linearity to grating superposition in more detail than previously (see Sections 4.7 and 5.5). Next, Section 6.3 shows the nonlinearities present in the feedforward model and explains linearity to grating superposition in that model, through a series of simplified representations. Section 6.4 is about why the proportional and hysteretic amplifiers satisfy grating superposition. Next, Section 6.5

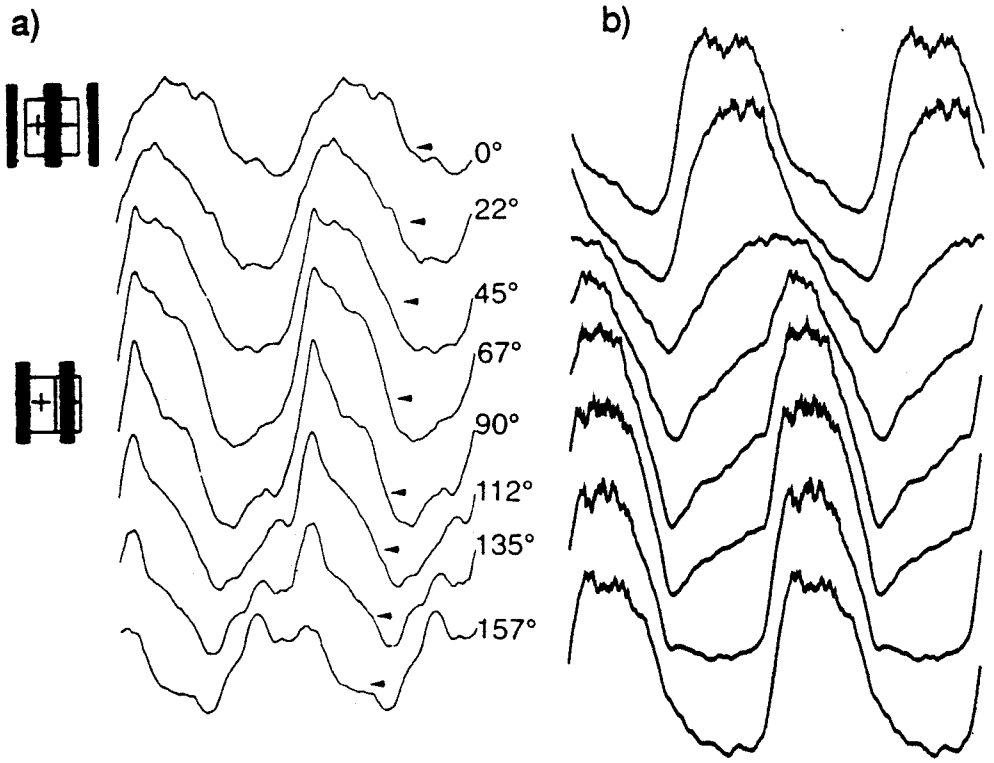

Figure 6.1: **Responses to stationary gratings** Fluctuations in membrane potential evoked by a 100 % contrast, 1 *cycle/deg*, 2 *Hz* contrast-reversal stationary sine wave grating, presented at eight different spatial phases, for **(a)** a neuron in cat visual cortex (data from Jagadeesh et al., 1993) and **(b)** a pyramidal neuron in the cortical amplifier model. Responses were averaged over 57 grating cycles, and each trace shows two copies of the average response to one grating cycle side by side (see Section 2.6).

presents a modified grating superposition test and predicts that linearity of simple cells in cortex will break down under this test. Finally, Section 6.6 discusses the significance of these results within the context of related research about neurons in visual cortex.

6.2 Superposition holds for the detailed models

The responses to stationary gratings at the eight spatial phases for the cortical amplifier model are compared to the experimental results (Jagadeesh et al., 1993) in

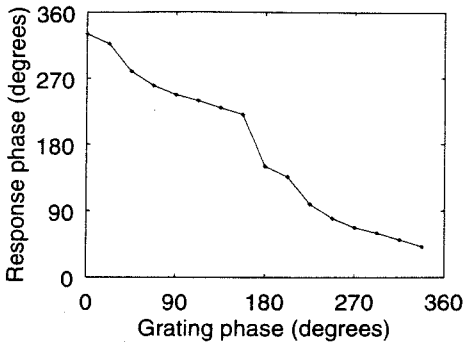

Figure 6.2: **Temporal phase of the responses to stationary gratings.** Phase of the first Fourier component of the fluctuations in membrane potential evoked by a 100% contrast, 1 *cycle/deg*, 2 *Hz* contrast-reversal stationary sine wave grating, presented at eight different spatial phases, as a function of the spatial phase of the grating, for a pyramidal neuron in the cortical amplifier model. The stimulus and response phases vary only over 180 degrees, so the graph was extended by duplication over the remaining 180 degrees of the full cycle.

Fig. 6.1. The feedforward model's responses to stationary gratings are similar. In both cases, the response was a periodic fluctuation of the intracellular membrane potential at the same temporal frequency as the stimulus. There are strong similarities in shape between the model and the data. For instance, compare the 6th trace from the top (112^o) in both panels. But most importantly, the temporal phase of the response depends on spatial phase, showing in the model a phase lag that increased linearly with spatial phase (Fig. 6.2). Such phase shifts have been found in direction-selective simple cells and have been proposed as the basic mechanism of direction selectivity in these cells (Hamilton et al., 1989; Saul and Humphrey, 1990; Reid et al., 1991; Albrecht and Geisler, 1991; DeAngelis et al., 1993; Heeger, 1993; McLean et al., 1994). Indeed, Fig. 4.13, from Chapter 4, shows that both models' responses to moving gratings are direction-selective, paralleling the results of Jagadeesh et al. (1993) for neurons in cat visual cortex: the amplitude of the periodic modulation is larger in the preferred than in the null direction.

Surprisingly, however, the preferred and null direction responses could be predicted (by linear summation of responses to stationary gratings, see Section 2.6) for

both feedforward and cortical amplifier models with an accuracy comparable to the experimental results, with no parameters needing to be adjusted specifically to reproduce this result. The preferred direction of motion as well as the direction index measured from the modulations of the intracellular somatic membrane potential could be predicted from the responses to the stationary gratings. The actual indices were 43.5% and 33.3% for the cortical amplifier and feedforward models respectively, while the predicted indices were 66.0% and 39.4%. The direction index measured intracellularly was much smaller than the direction index measured from the peak firing rate in both cortical amplifier (43.5% versus 93.2%) and feedforward models (33.3% versus 97.4%), as has been observed in cat visual cortex (Jagadeesh et al., 1993).

What makes this result surprising is that model pyramidal cells have many nonlinearities, particularly in the cortical amplifier model, as we will see in the next sections. However, we will provide an explanation for the apparent linearity of the models in spite of these nonlinearities, first for the feedforward model, then for the cortical amplifier model.

6.3 Explaining superposition for the feedforward model

In this section, we first give a simple, general overview of the feedforward model's nonlinearities and explanation for superposition in the feedforward model. Next, we construct a representation of the feedforward model using a series of simplified, formal models, to demonstrate the nonlinearities and superposition in more detail, too.

Nonlinearities in the feedforward model originate mainly from half-wave rectification in the LGN: LGN ON neurons only fire during the positive phase of the sinusoidal input. Although we do not model LGN OFF cells, eliminating half-wave rectification

totally with LGN OFF cells would require very precise balancing, which may not be biologically plausible. This half-wave rectification gives rise to half-rectified excitatory LGN current and half-rectified inhibitory current to the pyramidal neurons.

These nonlinearities produce higher-order Fourier components in the responses to stationary and moving gratings. For the linear, 1st Fourier components of the gratings superposition holds trivially as for sinusoids, from equation 2.7. In other words, the sum of the fundamentals of the responses to stationary gratings is equal to the fundamental of the response to a moving grating. However, as soon as there are nonlinear, higher-order Fourier components, superposition does generally not hold.

However, in a sum with many temporally offset waveforms, higher harmonics cancel, as we will see later. The response to moving gratings is predicted using such a sum. A similar phenomenon occurs for the actual response to moving gratings. Indeed, each model pyramidal and smooth cell gets input from five spatially diplaced LGN subunits. For a moving grating, the spatial displacement results in temporal phase offsets between subunit responses. The total response is again the sum of several (this time five) nonlinear, temporally offset waveforms. Since the higher harmonics cancel for both actual and predicted responses to moving gratings, leaving only the 0th and 1st Fourier components, superposition holds trivially.

That this is indeed happening can be seen directly from the responses of the models and those of the neuron in cat cortex. The waveforms of the responses to stationary gratings are highly nonlinear (Fig. 6.1), while the predicted and actual responses to moving gratings are quite sinusoidal (Fig. 4.13).

We now demonstrate that higher-order Fourier components indeed cancel in sums of temporally offset nonlinear waveforms. Let us show this for the sum of equation 2.8, in the case where the model's response ($R(x)$, see equation 2.8) is a simple half-wave

rectification:

$$R(x) = \rho_{1/2}(x) = \begin{cases} x & \text{if } x > 0 \\ 0 & \text{otherwise} \end{cases} . \tag{6.1}$$

We evaluate equation 2.8 for $x = 0$:

$$\frac{1}{4}\sum_{n=0}^{7} sin(n\frac{\pi}{8})\rho_{1/2}\left[sin(t + \frac{\pi}{2} + n\frac{\pi}{8})\right] . \tag{6.2}$$

Now, we approximate a half-wave rectified sinusoid by the first three terms in its Fourier series:

$$\rho_{1/2}[sin(t)] \cong \frac{1}{\pi} + \frac{1}{2}sin(t) - \frac{2}{3\pi}cos(2t) . \tag{6.3}$$

In the following, we discard the higher-order terms. We now introduce this approximation into the previous equation for the predicted response to a moving grating:

$$\frac{1}{4}\sum_{n=0}^{7}\left[sin(n\frac{\pi}{8})\frac{1}{\pi} + sin(n\frac{\pi}{8})\frac{1}{2}sin(t + \frac{\pi}{2} + n\frac{\pi}{8}) - sin(n\frac{\pi}{8})\frac{2}{3\pi}cos(2t + \pi + n\frac{\pi}{4})\right] . \tag{6.4}$$

Keeping in mind our goal of demonstrating that the sum of equation 2.8 is nearly sinusoidal with respect to time, we note that the first two terms in this equation are compatible with this notion. The first term is simply a constant with respect to time. The second term is sinusoidal. The third term, however, adds a higher harmonic to the predicted response, that may render it nonsinusoidal. However, we will see later numerically that the sum over n of this term is actually very small. We can also demonstrate analytically a similar result by discarding the spatial phase term, $sin(n\frac{\pi}{8})$, and evaluating the sum:

$$\sum_{n=0}^{7} cos(2t + \pi + n\frac{\pi}{4}) . \tag{6.5}$$

It can be rewritten as:

$$\sum_{n=0}^{3} \left[cos(2t + \pi + n\frac{\pi}{4}) + cos(2t + n\frac{\pi}{4}) \right] . \tag{6.6}$$

Each of these pairs of terms is 0, because of the π phase offset. Second-order components cancel due to summation of waveforms with temporal offsets of $\frac{\pi}{2}$. More generally, sinusoids with widely different temporal phases cancel out in sums, and although in the sum of the first Fourier component the phase differences are at most π, in the sums of higher components phases are spread out over the entire 2π range. Although we only considered half-wave rectification here, this argument should hold at least in part for most nonlinearities.

In conclusion, Fourier components of order higher than 1 in the responses to stationary gratings average out in the superposition sum, resulting in a predicted response to the moving gratings that is similar to that of a linear system, almost sinusoidal. A similar phenomenon occurs for the actual response to moving gratings, resulting in superposition.

After giving this general argument, we now present simplified models that approximate the functioning of the feedforward model and examine more in detail this model's nonlinearities and how closely superposition holds. In the following analysis, instead of using a single neuron model that produces action potentials, neurons have a graded output that can be identified both as voltage and spiking rate. In fact, the network has only two neurons, one pyramidal cell and one smooth neuron.

We call $F_s(t)$ the voltage output of our model pyramidal neuron for a certain stimulus s. The stimulus can be a sine wave grating moving in the preferred $(+)$ or null $(-)$ directions:

$$s(x,t) = s_{mov\pm}(x,t) = sin(kx \mp t)\,, \tag{6.7}$$

where x is spatial position, t time and k spatial frequency (assuming that the temporal

frequency is 1 Hz); or a stationary contrast-reversal sine wave grating at several spatial phases (n=0,..,7):

$$s(x,t) = s_{rev,n}(x,t) = sin(kx + n\frac{\pi}{8})sin(t)\,. \tag{6.8}$$

In this notation we can write conveniently the two equations expressing sine wave gratings moving in the preferred (+) or null (−) directions in terms of the superposition of eight contrast-reversal sine wave gratings:

$$s_{mov\pm}(x,t) = \frac{1}{4}\sum_{n=0}^{7} s_{rev,n}(x,\, t + \frac{\pi}{2} \pm n\frac{\pi}{8})\,. \tag{6.9}$$

We now construct a representation of the feedforward model using three simplified models that each build on the previous one by adding an important feature of the feedforward model. The first simplified model only includes half-wave rectification in the LGN, without direction selectivity or any other cortical processing. The model pyramidal neuron receives excitatory synaptic current from a half-wave rectified LGN neuron, and the waveform of the pyramidal neuron's voltage is similar to that current's waveform. So, assuming a neuron centered at spatial position $x_0 = 0$, the first approximation to the feedforward model's voltage output is:

$$F_s^{(1)}(t) = \rho_{1/2}[s(x_0,t)]\,. \tag{6.10}$$

Fig. 6.3 shows this model's response to the stationary gratings and to a moving grating, as well as the predicted response to the moving grating, based on superposition. Although the responses to the individual stationary gratings are half-wave rectified, the predicted voltage to the moving grating is close to a full sinusoid. The prediction for this model actually evaluates numerically equation 6.2. This equation is approximated by equation 6.4. That the result is close to a full sinusoid means that

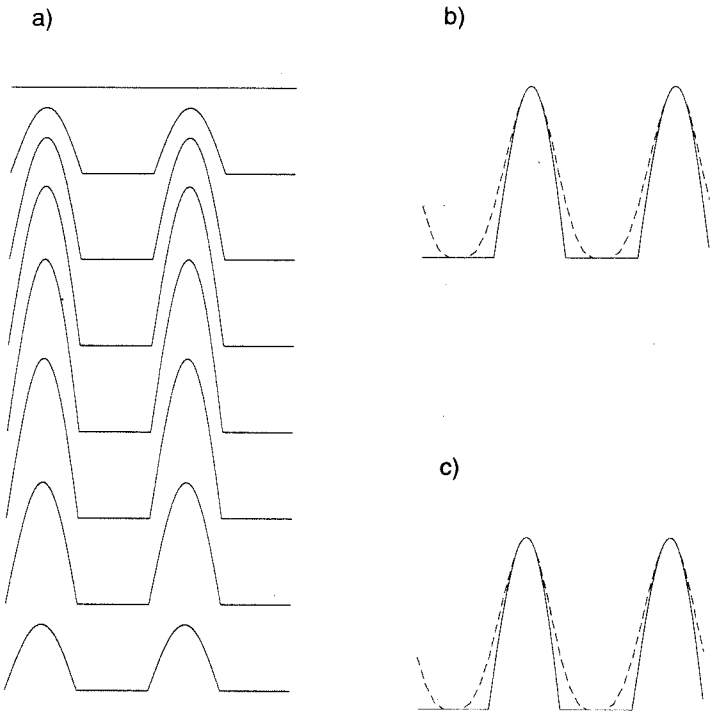

Figure 6.3: **Superposition test for the first simplified model.** Responses of a simplified model ($F_s^{(1)}(t)$, see equation 6.10), which approximates the voltage output of the detailed feedforward model; it is an approximation that includes only the effect of half-rectification in LGN input to the pyramidal neurons. Shows the responses to two grating cycles. **(a)** Responses to stationary contrast-reversal sine wave gratings at eight different spatial positions (from top to bottom $n = 0$ to $n = 7$; see equation 6.8). **(b)** Response to a moving grating (+ direction, shown with continuous line; see equation 6.7) compared with the response predicted from summing stationary gratings (dashed). Superposition holds only very approximately, because of the rectification nonlinearity.

the sum over the second Fourier component in that equation is very small. So we confirm the statement made above, that higher-order harmonics cancel out in sums with temporal phase offsets. However, the response to the moving grating is half-wave rectified and so does not match the prediction well, as expected from nonlinear processing in the presence of only one spatial subunit.

The next most basic operation in the detailed model is inhibition, mediated by $GABA_A$ and $GABA_B$ processes, and responsible for direction selectivity. To a first approximation, the smooth neuron's firing rate output is also given by half-wave rectification of the stimulus, but at a spatially displaced location. The spatial offset is $5' = 1/12°$. Denote $x_n = n/12°$. The smooth neuron's firing rate for stimulus s is then:

$$\rho_{1/2}[s(x_1, t)]\,. \tag{6.11}$$

The transformation giving the $GABA_A$ and $GABA_B$ synaptic current from the smooth neuron's firing rate is a filtering operation. Its impulse response γ_{AB} is determined by the functions, weights and time constants of the detailed model (see Section 2.5). Adding inhibition to our first simplified model $F_s^{(1)}(t)$ by convolving the smooth neuron's firing rate with γ_{AB} gives the second simplified model:

$$F_s^{(2)}(t) = \rho_{1/2}[s(x_0, t)] - \gamma_{AB} * \rho_{1/2}[s(x_1, t)]\,. \tag{6.12}$$

We show in Fig. 6.4 this model's response to the stationary and moving gratings, as well as the predicted response to the moving gratings, based on superposition. The model is direction-selective. Again, the predicted voltage traces are quite sinusoidal, although the responses to stationary gratings have a very complicated, temporally nonlinear shape, due to the combination of rectification in the LGN currents to pyramidal and smooth neurons. However, the responses to moving stimuli show higher-order Fourier components and do not match the predictions well.

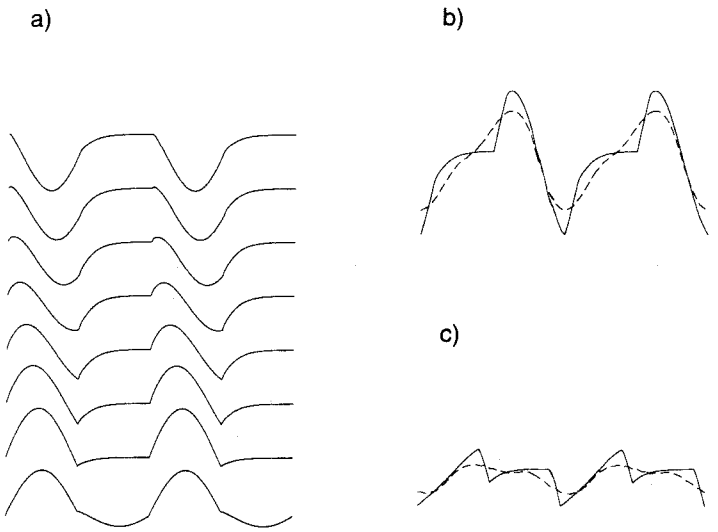

Figure 6.4: **Superposition test for the second simplified model.** Responses of a simplified model ($F_s^{(2)}(t)$, see equation 6.12), which approximates the voltage output of the detailed feedforward model; it is an approximation that includes the effects of half-rectification in the LGN and $GABA_A$ and $GABA_B$ inhibition (including rectification in the LGN inputs to the smooth neuron). Shows the responses to two grating cycles, for gratings with spatial frequency $k = 2\pi$. **(a)** Responses to stationary contrast-reversal sine wave gratings at eight different spatial positions (from top to bottom $n = 0$ to $n = 7$; see equation 6.8). **(b)** Response to a grating moving in the preferred direction (continuous) compared with the response predicted from summing stationary gratings (dashed). **(c)** Response to a grating moving in the null direction (continuous) compared with the response predicted from summing stationary gratings (dashed). In both directions of motion, superposition holds only very approximately, because of the rectification nonlinearities.

There is another important property of the detailed model that has not been taken into account in the simplified models. Both pyramidal and smooth neurons receive input from LGN neurons at five spatial positions, instead of one. The five inputs to the smooth neurons are displaced by $1/12°$ from the inputs to the pyramidal neurons. Incorporating this arrangement in the previous simplified model gives the third simplified model:

$$F_s^{(3)}(t) = \sum_{n=0}^{4} \rho_{1/2}[s(x_n, t)] - \sum_{n=1}^{5} \gamma_{AB} * \rho_{1/2}[s(x_n, t)]\,. \tag{6.13}$$

The actual and predicted responses are shown in Fig. 6.5. The predicted voltage traces are highly sinusoidal, despite the presence of higher-order Fourier components in the individual responses to stationary stimuli. But in addition, the responses to moving stimuli are highly sinusoidal, and match the predictions very well. Indeed, as discussed previously, summation of the subunit responses results in cancellation of higher harmonics.

In summary, by breaking down the feedforward model into some of its basic components, half-wave rectification, $GABA_A$ and $GABA_B$ inhibition, and summation of spatial subunits, we note important sources of nonlinearity in the feedforward model. However, we can explain the success of the superposition test by noting that higher-order Fourier components average out in sums of terms with various temporal phases.

6.4 Influence of the cortical amplifier's feedback connections

Both cortical amplifier and feedforward models are based on rather similar mechanisms, so their nonlinearities arise from some of the same sources: half-wave rectification in both excitatory and inhibitory currents. However, excitatory intracortical

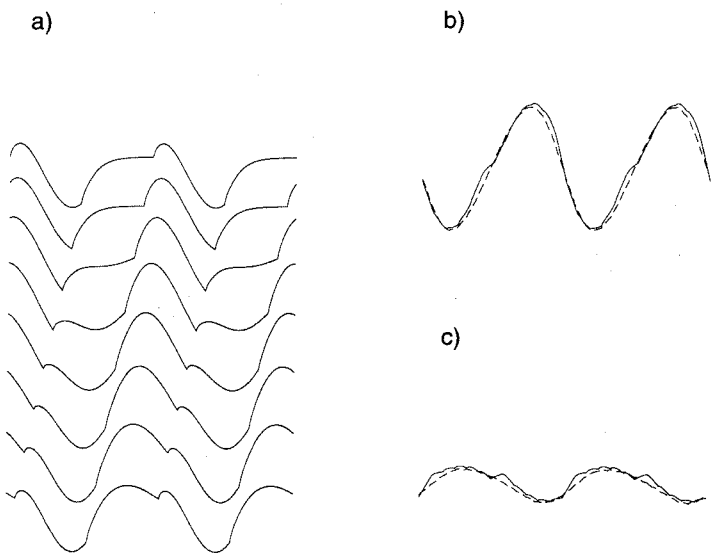

Figure 6.5: **Superposition test for the third simplified model.** Responses of a simplified model ($F_s^{(3)}(t)$, see equation 6.13), which approximates the voltage output of the detailed feedforward model; it is an approximation that includes the effects of half-rectification in the LGN, $GABA_A$ and $GABA_B$ inhibition (including rectification in the LGN inputs to the smooth neuron), and spatial summation of LGN inputs in the cortical neurons. Shows the responses to two grating cycles, for gratings with spatial frequency $k = 2\pi$. **(a)** Responses to stationary contrast-reversal sine wave gratings at 8 different spatial positions (from top to bottom $n = 0$ to $n = 7$; see equation 6.8). **(b)** Response to a grating moving in the preferred direction (continuous) compared with the response predicted from summing stationary gratings (dashed line). **(c)** Response to a grating moving in the null direction (continuous) compared with the response predicted from summing stationary gratings (dashed). For both directions of motion, superposition holds well, because of cancellation of the nonlinearities through summation.

connections (also called feedback connections) are an additional source of nonlinearity in the cortical amplifier. Indeed, amplification occurs only when the pyramidal neurons are spiking, which requires that the membrane voltage exceeds the spiking threshold. As a first step, to underscore the apparent paradox, we show using a simplified model that because of this nonlinearity the superposition test should not hold for the cortical amplifier model. Since the superposition test still holds, as we have seen above, we explain thereafter why the simple model does not apply and why the superposition test holds.

To model the effects of the canonical microcircuit's amplification, we modify one of the models presented in the previous section ($F_s^{(3)}(t)$), by multiplying the voltage by a constant factor, say 4 (see Section 4.2 for a justification of this value), if the output is larger than 0:

$$F_s^{(4)}(t) = \begin{cases} 4F_s^{(3)}(t) & \text{if } F_s^{(3)}(t) > 0 \\ F_s^{(3)}(t) & \text{otherwise} \end{cases} . \tag{6.14}$$

Fig. 6.6 presents this model's responses to stationary and moving gratings, as well as the predicted responses. Superposition does not hold. Indeed, for stationary contrast-reversal sine wave gratings the feedback current is half-wave rectified, so in the waveform of the response the positive phase will be in general much larger than the negative phase. For a grating moving in the null direction, the response will be approximately the same as in the $F_s^{(3)}(t)$ model, given the high degree of direction selectivity of the neuron that we chose to model. For the $F_s^{(3)}(t)$ model, the sum of responses to stationary gratings added up with appropriate phases to the response in the null direction. For the $F_s^{(4)}(t)$ model, waveforms to stationary gratings are different, with a much larger positive phase. The sum is not going to add up to the same response in the null direction. Clearly even the average value of that sum is not

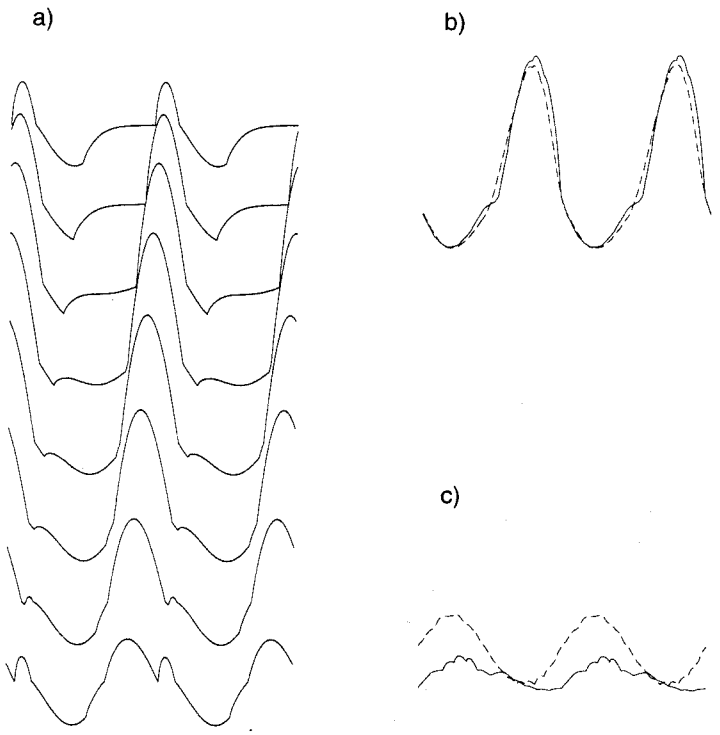

Figure 6.6: **Superposition test for a simplified model of the cortical amplifier.** The simplified model $F_s^{(4)}(t)$ (see equation 6.14) is an approximation that includes the effects of half-rectification in the LGN, $GABA_A$ and $GABA_B$ inhibition (including rectification in the LGN inputs to the smooth neuron), spatial summation of LGN inputs in the cortical neurons, as well as amplification by the excitatory loop. Shows the responses to two grating cycles, for gratings with spatial frequency $k = 2\pi$. **(a)** Responses to stationary contrast-reversal sine wave gratings at eight different spatial positions (from top to bottom $n = 0$ to $n = 7$; see equation 6.8). **(b)** Response to a grating moving in the preferred direction (continuous) compared with the response predicted from summing stationary gratings (dashed). **(c)** Response to a grating moving in the null direction (continuous) compared with the response predicted from summing stationary gratings (dashed). Although superposition holds well in the preferred direction, it does not hold in the null direction, because of nonlinear amplification that operates for stationary gratings and for gratings moving in the preferred, but not in the null direction.

going to be the same anymore.

We have shown that amplification by the canonical microcircuit should result in significant nonlinearity to grating superposition. However, such is not the case in the detailed cortical amplifier model (see Fig. 4.13a and b). We now explain why the $F_s^{(4)}(t)$ model is not an appropriate description of the cortical amplifier. Understanding this will then allow us, surprisingly, to reduce the cortical amplifier model back to the simplified model without amplification, $F_s^{(3)}(t)$.

The $F_s^{(4)}(t)$ model is not appropriate because in the detailed model action potentials occur during the positive phase of the average voltage trace. Although these action potentials are stripped by the median filter mentioned above, and so at a first glance do not seem to affect the average voltage trace, they create a maximum voltage, the spike initiation threshold, that will never be exceeded. While the membrane is at this maximum voltage, any additional current will not translate into an increase in average voltage. Instead, the current will result in an action potential, and after the spike the voltage will be brought back below the spike threshold; once the spike is stripped by the median filter, it is as if the current had never been present. Current is "sunk" in the action potentials (Bernander et al., 1994), and $F_s^{(4)}(t)$ does not take into account the sinking of this current.

The amount of current sunk can be revealed by blocking the currents responsible for the action potentials (fast sodium Na and delayed rectifier potassium K_{DR}; see Section 2.4) in only one pyramidal neuron and recording the average membrane potential in that cell. Compared with the unblocked case (Fig. 6.7a), the voltage is much larger in the positive phase of the response. The current sunk that the $F_s^{(4)}(t)$ model does not take into account is large. So, while the simplified analysis describes well the net current in the cortical amplifier case, it falls short of predicting the corresponding voltage in the positive phase of the response.

It is not surprising, therefore, that $F_s^{(4)}(t)$'s prediction that linear superposition

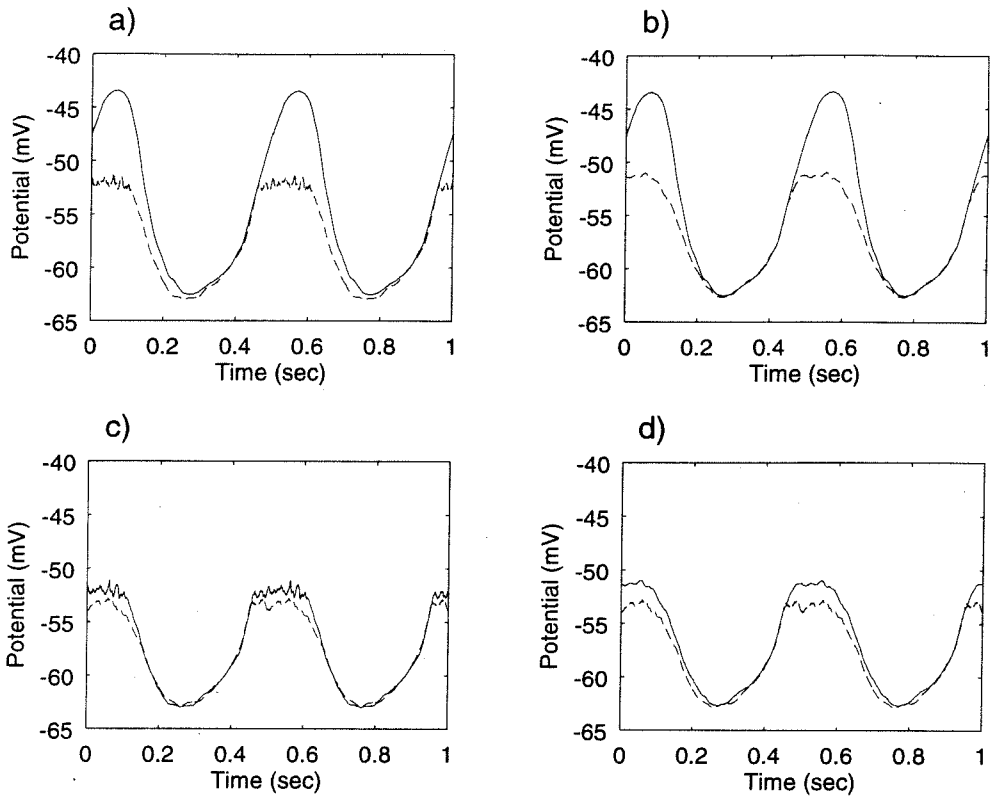

Figure 6.7: **Analysis of the cortical amplifier's intracellular response.** Modulations in membrane potential evoked in one model neuron by a 100% contrast, 1 *cycle/deg* sine wave grating, drifting in the preferred direction at 2 *Hz*. **(a)** Cortical amplifier (dashed); after blocking the action potentials (by removing fast sodium and delayed rectifier potassium currents) in the fiducial cell (continuous). A large current is sunk in the action potentials. **(b)** After blocking action potentials in the fiducial cell (continuous); after in addition removing all feedback excitatory connections (dashed). There is a large feedback current during the positive phase of the response. **(c)** Cortical amplifier (continuous); after removing all feedback excitatory connections (dashed). Most of the feedback current gets sunk in the action potentials. **(d)** After removing all feedback excitatory connections in the cortical amplifier model (dashed); after in addition blocking action potentials in the fiducial cell (continuous). Little LGN current is sunk in the action potentials. We conclude that for the purpose of predicting the intracellular response, we can reduce the cortical amplifier to the feedforward model.

should not hold, is not borne out by the detailed cortical amplifier model. However, this does not explain the detailed model's linearity to grating superposition. The explanation is that most excitatory intracortical current is sunk before affecting the voltage, while the LGN current remains essentially intact, as we will see shortly. In other words, surprisingly, we can reduce the cortical amplifier model to the feedforward model, for the purposes of predicting the average voltage. We have already seen that linearity holds for the simplified feedforward case $F_s^{(3)}(t)$.

The large feedback current can be demonstrated by blocking action potentials in the fiducial cell only and comparing the potentials with and without excitatory cortical connections (Fig. 6.7b). That most of this current is sunk in the action potentials can be seen by comparing the average potentials in the unblocked case with and without cortical feedback (Fig. 6.7c). They are very similar.

After removing all excitatory feedback in the cortical amplifier case, we can compare the average membrane potential with and without blocking the currents responsible for the action potentials (Fig. 6.7d): little LGN current is sunk in the action potentials. That is because for the contrasts used in the test, which are just large enough to produce strong firing in the pyramidal neurons, the LGN input by itself would result in only very few spikes in the pyramidal neurons, bringing them barely above threshold. However, there is some sinking even in this case, meaning that the average membrane potential reaches its maximum. This observation explains that nearly all excitatory cortical current is sunk, since this current occurs when pyramidal neurons are spiking even without cortical feedback, and so have already reached their maximum potential.

So the excitatory intracortical current has very little effect on the membrane potential. In addition, only a small portion of the LGN current is sunk in the action potentials. We conclude that, surprisingly, $F_s^{(3)}(t)$ can be used to model the cortical amplifier's membrane potential.

6.5 Superposition test using only two stationary gratings

Jagadeesh et al. (1993) used eight stationary gratings in their superposition test. However, a moving grating can be written as sum of two stationary gratings only:

$$sin(kx \pm \omega t) = sin(kx + n\frac{\pi}{8}) \cdot sin(\omega t + \frac{\pi}{2} \mp n\frac{\pi}{8}) + sin(kx + n\frac{\pi}{8} + \frac{\pi}{2}) \cdot sin(\omega t + \frac{\pi}{2} \mp n\frac{\pi}{8} \mp \frac{\pi}{2}). \tag{6.15}$$

This equation is valid for any of $n = 0, .., 3$. It allows us to formulate a modified superposition test that uses only the responses to two stationary gratings to predict the responses to moving gratings. The cortical amplifier's actual response to a grating moving in the null direction is compared in Fig. 6.8a-d to the four predictions ($n = 0, .., 3$) from this superposition test. The outcome of the eight grating superposition test is shown in Fig. 6.8e for comparison. Although with two gratings the prediction's 1st Fourier component is the same as that of the evoked response, the overall shape of the prediction is very different due to discrepancies in higher-order components. The average mean square error is 0.64 mV^2 for the prediction with eight gratings and 1.95 mV^2 for those with two gratings. Since there is little noise in the two grating prediction (Fig. 6.8f), noise due to less averaging is not by itself the cause of the mismatch.

Rather, it originates in the large nonlinear components in the responses to stationary gratings (see Fig. 6.1). As we noted above (see equation 6.6), the second Fourier components cancel in sums of nonlinear waveforms with temporal offsets of $\frac{\pi}{2}$, and so they will cancel partially even for the two grating superposition sum. However, cancelling higher-order components require more terms in the sum. For instance, cancelling the fourth Fourier component will require in addition terms with temporal offsets of $\frac{\pi}{4}$.

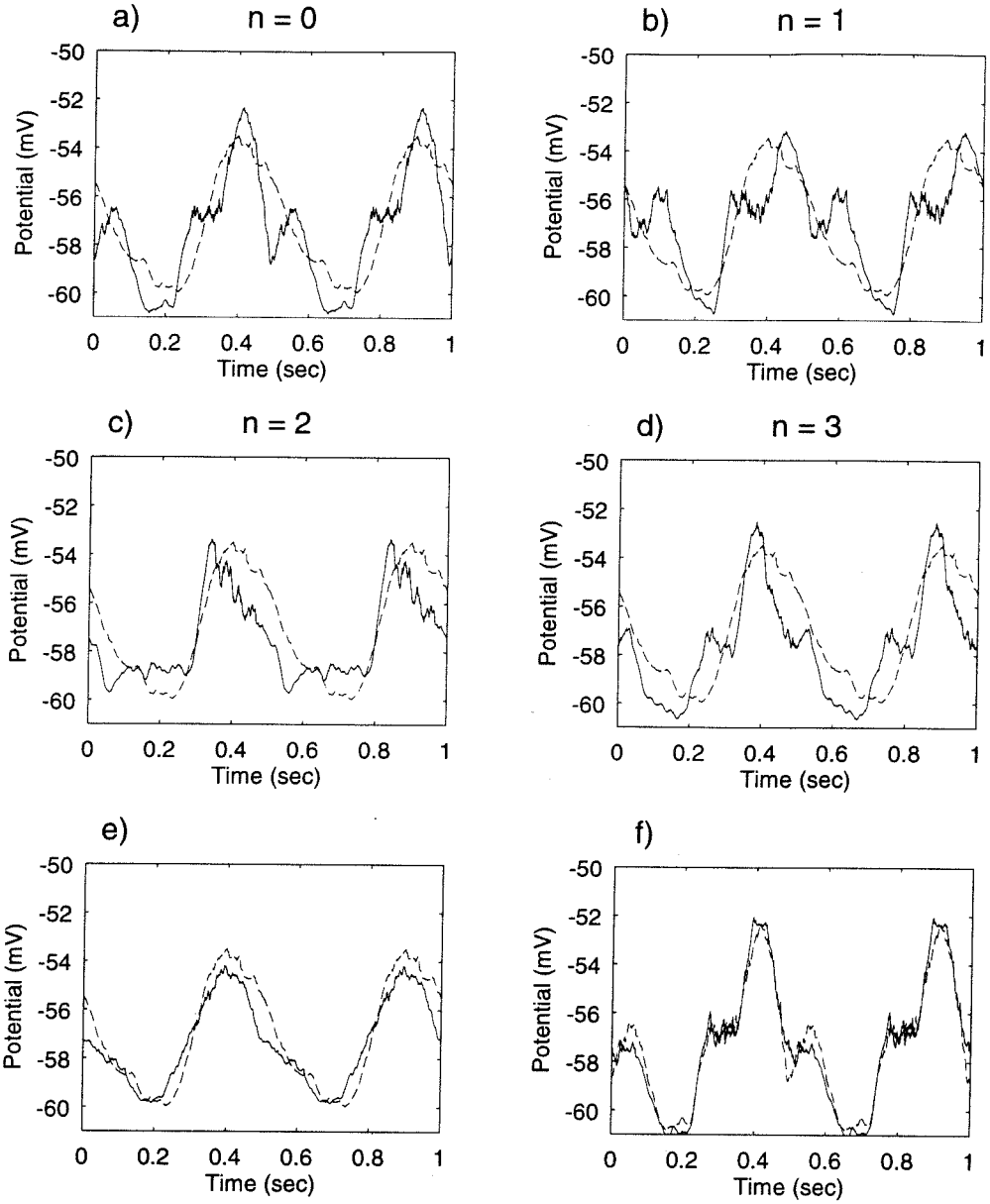

Figure 6.8: **Superposition test using only two stationary gratings.** The first four panels **(a,b,c,d)** compare the modulations in membrane potential evoked (dashed) by a 100% contrast, 1 *cycle/deg* sine wave grating, drifting in the null direction at 2 Hz, and the response predicted (continuous) from summing four different pairs ($n = 0, .., 3$ in equation 6.15) of stationary contrast-reversal gratings, for one cell in the cortical amplifier model. Each trace results from averaging the responses to 57 grating cycles. **(e)** Compares the modulation evoked (dashed) in the null direction and the response predicted (continuous) from summing eight stationary gratings (as in Fig. 4.13b) : the prediction is much more accurate when summing eight stationary gratings. **(f)** Compares the prediction for $n = 0$ (dashed) with the same prediction, but from a run with a different random seed (continuous): there is little noise in the prediction that uses two stationary gratings. We conclude that linearity to superposition holds only under narrowly defined conditions.

The two grating superposition test detects the model's nonlinearity, and its outcome is consistent with our explanation of why the eight grating superposition test holds. We conclude that full linearity to grating superposition cannot be inferred from the eight grating superposition test.

6.6 Discussion

Jagadeesh et al. (1993) have proposed that their experimental results showing linearity to grating superposition argue strongly against nonlinear processing in direction-selective cortical cells. In addition, we note that linearity of these cells would require a precise mechanism in cortex to compensate for half-wave rectification in the retina and LGN. However, we argue that determining if a given nonlinear model can truly be ruled out by these results has to be done directly by performing the same grating superposition test on model neurons. The role of the present chapter is to evaluate the test's sensitivity by applying it to two models of direction selectivity that include substantial nonlinear processing, one based on a scheme originally proposed by Barlow and Levick (1965), the feedforward model, and the other one based on the canonical microcircuit, the cortical amplifier model. The model's responses to stationary gratings are very similar to experimental results in overall shape, and their temporal phase varies linearly with the gratings' spatial phase, as observed experimentally. For both models, the fluctuations in membrane potential evoked by moving sine wave gratings were well predicted by linear summation of stationary contrast-reversal sine wave gratings, paralleling the results of Jagadeesh et al. (1993) for neurons in cat visual cortex.

Using simplified models, we have demonstrated that indeed substantial nonlinearities are present in these models: half-wave rectified thalamic input, half-wave rectified firing pattern of inhibition, and amplification with a threshold using the

canonical microcircuit. So superposition for these models is unexpected. However, we have provided an explanation for our observations, again using these simplified models. We have noticed that summing nonlinear waveforms with temporal phase offsets will result in partial cancellation of the higher harmonics, leaving mostly the zeroth and first Fourier components. This cancellation occurs when the responses to stationary gratings are summed to perform the superposition test, resulting in a predicted waveform that is highly sinusoidal. It occurs also within the model neurons for moving grating stimuli, because inputs from LGN neurons at many spatial offsets are summed in the pyramidal neurons. The remaining contributions to the responses are sinusoids, and for sinusoids superposition holds trivially. Nonlinear amplification in the cortical amplifier model requires a separate explanation. The feedback current occurs at a moment in the cycle when the pyramidal neurons are already firing in response to the LGN input, even only moderately, so that the average potential is already close to its maximum (the spiking threshold). So the feedback current is sunk in the spike mechanism of the neurons, and does not influence the average membrane potential. It is very striking that withdrawing this large current results in very little change in the average potential (Fig. 6.7), and contrasts dramatically with the effect of withdrawing the feedback current on peak firing rates: they drop to near-zero values (see Fig. 4.7). That this large current is not reflected in the average intracellular potential demonstrates that its measure is not a substitute for counting action potentials.

While our simplified models do not address directly the issue of whether Jagadeesh et al.'s results argue against nonlinear synaptic mechanisms, such as silent or shunting inhibition (Torre and Poggio, 1978; Koch and Poggio, 1985; Koch et al., 1990), the feedforward model does. For this model (see Section 4.2), there are large inhibitory conductance changes in the null direction, mostly mediated by $GABA_A$ through chloride channels, and the reversal potential for chloride is $-75mV$, close to the average

potential in the null direction (Fig 4.13d), so shunting inhibition is occurring; nevertheless, there is linearity to superposition. So this test cannot detect the presence of shunting inhibition, either.

It is surprising that such an elaborate test of linearity is not able to detect the presence of these substantial nonlinearities. We have shown that a superposition test that uses two stationary gratings only yields a far different result, demonstrating the models' nonlinearity. So linearity to grating superposition itself is very relative. We conclude that linearity tests that require much averaging and use grating stimuli can be misleading. More generally, it is important to evaluate rigorously physiological experiments by directly testing their methodology through detailed modeling.

6.7 Summary

Jagadeesh et al. (1993) studied the linearity of direction selectivity in simple cells using an intracellular grating superposition test and concluded that the mechanism of direction selectivity is linear summation of synaptic potentials without any need for nonlinear processes. The role of the present chapter is to evaluate whether this linearity test can rule out nonlinear models by testing through detailed computer simulations two models of direction selectivity that include substantial nonlinear processing, one based on a feedforward scheme and the other featuring nonlinear amplification through excitatory cortical feedback. We demonstrate that substantial nonlinearities are present in these models, including shunting inhibition in the feedforward model. However, we find that both models are linear according to the grating superposition test. We explain these surprising results, again using the simplified models. First, we notice that summing nonlinear waveforms with temporal phase offsets will result in partial cancellation of the higher harmonics, leaving mostly the zeroth and first Fourier components. This cancellation occurs when the responses to stationary grat-

ings are summed to perform the superposition test, resulting in a predicted waveform that is highly sinusoidal. It occurs also within the model neurons for moving grating stimuli, because pyramidal neurons receive inputs from LGN neurons at many spatial offsets. The only remaining contributions to the responses are sinusoids, and for sinusoids superposition holds trivially. Surprisingly, we show that action potentials absorb the excitatory feedback current completely, so that the membrane potential is identical with or without excitatory intracortical connections, and nonlinear amplification does not interfere with superposition. Finally, the models make the testable prediction that linearity breaks down when tested with superposition of two gratings, instead of eight as in Jagadeesh et al. (1993). We conclude that linearity tests that require much averaging and use grating stimuli can be misleading and that detailed modeling is crucial for the interpretation of physiological experiments.

Chapter 7

Methodological Considerations

7.1 Introductory remarks

In this chapter, we discuss methodological considerations about our models and simulations. For any model of visual cortex, a large number of assumptions must be made. These assumptions reflect both the limits of current scientific knowledge, and current computational limits. It is not feasible to model a network of neurons that each has thousands of compartments such as in Bernander (1993). But even the present model stretched probably beyond some practical limits. Indeed, the simulations discussed here involve numerical solutions to a large number (about 1000 in the proportional amplifier, about 16 times more in the hysteteretic amplifier) coupled partial differential equations, with a sizable fraction thereof nonlinear, including about 140 cellular and network parameters. For instance, producing Fig. 5.7 (see Chapter 6) required about two weeks of SPARCstation 10 CPU time. Indeed, in the hysteretic amplifier model, the computational problem was exacerbated by a noise amplification process described later in this chapter. This problem necessitated large increases in the number of neurons in the network.

Making this computational problem much worse is the challenge of identifying a regime in this high-dimensional parameter space that **(1)** was compatible with the available experimental literature on synaptic inputs and single cell properties and **(2)** that reproduced the known response curves. This search for "optimal" parameters provided major impetus for simplifying our model through assumptions presented in this chapter.

Indeed, this parameter search problem is quite acute, because the model is strongly sensitive to certain parameters, for instance neuron threshold and weight of the connection between pyramids. We will see in this chapter the extent to which this parameter sensitivity restricts the range of optimal parameter values.

Section 7.2 discusses the general assumptions made in the models. Section 7.3 discusses parameter dependency of the models. Parameters discussed include neuron threshold, shape of the network transfer function, feedback strength, and inhibition strength. Section 7.4 presents the noise amplification process in the hysteretic amplifier model, a problem that provided much of the impetus behind the analysis in Chapter 3.

7.2 Assumptions

Both morphology and physiology of our model neurons were derived from experimentally recorded neurons. Nevertheless, these neurons were extensively simplified so as to remain within the practical limitations of large scale digital simulations (Wilson and Bower, 1989; Bush and Sejnowski, 1993); in particular, model cells only had three or four compartments, which did not allow modeling of nonlinear synaptic interactions or local membrane nonlinearities such as dendritic spikes. At the moment, we do not have any direct evidence that these phenomena are important to understand the properties considered in this paper. Furthermore, because of a lack of quantita-

tive data about the strength and distribution of NMDA synapses in visual cortex, we omitted any voltage-dependent synaptic transmission in our network.

The general results reported in this paper were generally not critically dependent on any particular parameter. There are a few spectacular exceptions, that are discussed in Section 7.3. The primary exception is the parameter α, corresponding to the slope of the $F(f)$ curve. Stability of the proportional amplifier model requires $\alpha < 1$ (see eq. 3.6, Section 3.2). In particular, this meant that the weight controlling the strength of the cortico-cortical feedback strongly affects the slope of the contrast-response curve.

We modeled a patch of cortex as if it were a small (50-800) group of direction-selective neurons that are fully interconnected with each other and that are not connected to any neurons outside the group. From what we know about the weak columnar organization of direction selectivity (Payne et al., 1980; Tolhurst et al., 1981b; Berman et al., 1987) and the high divergence and convergence of cortical networks, including long-range connections (Gilbert and Wiesel, 1983; Martin, 1984; Martin and Somogyi, 1985; Gabbott et al., 1987; White, 1989; Braitenberg and Schüz, 1991; Ahmed et al., 1994), these assumptions are unlikely to be true. However, they represent a valid starting point for grasping the cortical network's function. Also, neurons with similar response properties are likely to be more strongly connected, due to Hebbian mechanisms operating in cortex (Miller, 1992; Bliss and Collingridge, 1993).

In order to facilitate our task, the smooth neurons received only feedforward input, thereby rendering them insensitive to the direction of motion (Fig. 4.3). However, identified smooth (basket) cells in visual cortex are known to share direction selectivity and other receptive field properties with their excitatory neighbors (Martin et al., 1983). As mentioned in Section 2.5, we have verified in a simpler cortical amplifier model (with continuous firing rates) that inhibitory interneurons can have direction preference too.

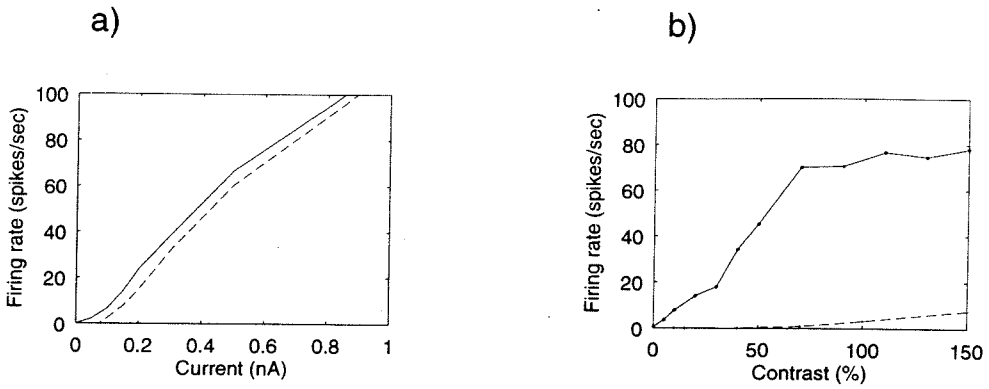

Figure 7.1: **Dependence of the contrast-response curve on the threshold of the pyramids' current-discharge curve.** **(a)** Current-discharge curve of the pyramidal neurons in a parameter condition similar to the proportional amplifier (continuous) and current-discharge curve in an otherwise identical parameter condition where the amplitude of excitatory synaptic noise events was reduced (dashed); the corresponding reduction in the total current injected by these events was 50 pA on the average. **(b)** Contrast-response curves corresponding to the two cases shown in panel (a), to moving gratings (1 Hz, 1 c/deg). Increasing the threshold of the current-discharge curve by only 50 pA results in a very large reduction in the response over the whole range of contrasts.

7.3 Parameter dependence

7.3.1 Dependence on neuron threshold

In the model, responses depend exquisitely on the neurons' thresholds. Indeed, the net input is very small (Fig. 4.5b, Section 4.2), so that any increase in threshold will cut the suprathreshold input substantially. The decrease in net input will be amplified, resulting in a large drop in the response.

This phenomenon is illustrated in Fig. 7.1 for the contrast-response curve. An increase in the threshold of all pyramidal neurons of only 50 pA causes the response to drop almost to 0 Hz.

When the threshold is diminished by just 10 pA for all pyramidal neurons in

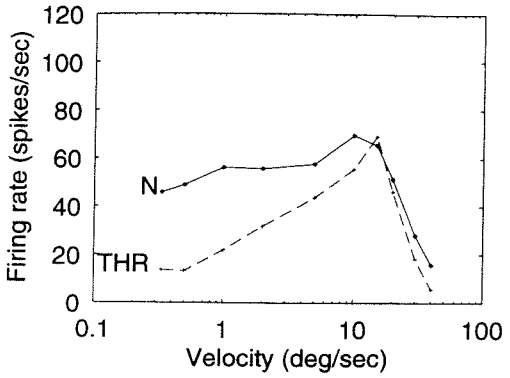

Figure 7.2: **Dependence of the velocity-response curve on the threshold of the pyramids' current-discharge curve.** Velocity-response curves to moving bars (2 *deg/sec*) for the normal proportional amplifier (N, continuous), and when the threshold of all pyramidal neurons has been increased by injection of 10 *pA* of negative DC current. Increasing the threshold of the current-discharge curve by only 10 *pA* results in a large reduction in the response, especially at low velocities.

the cortical amplifier model, the response diminishes by a factor of 3 at low velocities (Fig. 7.2). Indeed, the input is especially small at low velocities (Fig. 4.8 in Section 4.4). Also, amplification is largest at low velocities (Section 4.5).

Clearly, obtaining the desired value of the threshold required extensive fine-tuning of the parameters. The resulting parameter condition was very sensitive to any modification in one of the currents that can influence the threshold.

7.3.2 Shape of the network transfer function

Small differences in the shape of the network transfer function $F(f)$ (for a definition, see Section 3.2) can also result in large differences in the contrast-response curve. Fig. 7.3 shows an instance of this sensitivity. A linearized $F(f)$ is quite linear indeed, but the corresponding contrast-response curve is much shallower than the linear case. The contrast-response curves were obtained for the same LGN inputs as in the detailed model, but the neurons were simulated average firing rate neurons (one pyramidal and

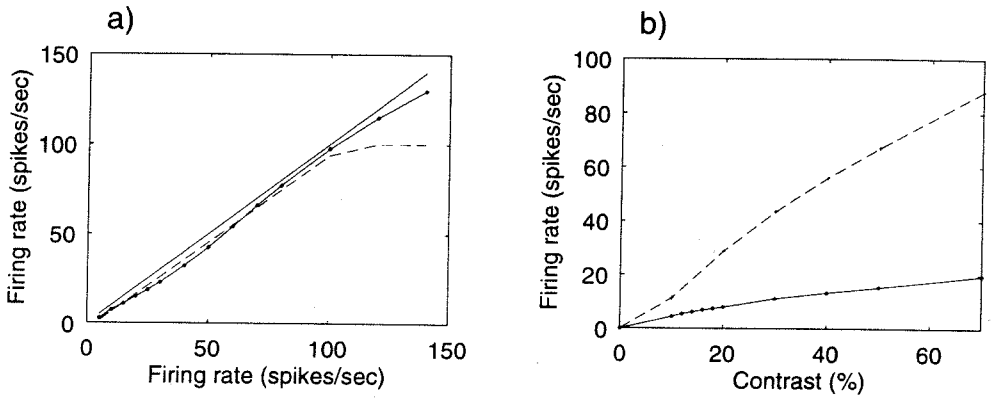

Figure 7.3: **Dependence of the contrast-response curve on the shape of the network transfer function** $F(f)$. This figures shows **(a)** two different network transfer functions and **(b)** the corresponding contrast-response curves for bars that are generated using the corresponding average rate dynamical model (DYNAMO; see Section 3.7). The first case (dashed) has an $F(f)$ that is linear up to saturation with slope very close to 1. In the second case (continuous), $F(f)$ is computed from a recurrent current function I_{rec} that is similar to that of the proportional amplifier (see Fig. 3.1a, Section 3.2), and a current-discharge function F_i that was measured from a pyramid in a cortical amplifier model whose parameters were optimized with the goal of linearizing $F(f)$. Although the resulting $F(f)$ is quite linear, the small deviations from linearity are enough to result in very different contrast-response curves. In the case that is only approximately linear, the response is small.

one smooth) with the corresponding $F(f)$ curves (see Section 3.7).

7.3.3 Feedback strength

The gain of the proportional amplifier is $\frac{1}{1-\alpha}$, where α is the slope of the $F(f)$ curve in the linear case (eq. 3.6, Section 3.2). Since α is already close to 1, the gain (and the response) should be very sensitive to the exact value of α. For the hysteretic amplifier, the slope of $F(f)$ is very close to 1, and if diminished it might become less than 1 and transform into the proportional amplifier model. Again, the response should be very sensitive to this parameter.

Increasing the strength of the feedback excitation between pyramidal neurons will increase the slope of the recurrent current curve I_{rec}, and α, too. Fig. 7.4 depicts the effect of decreasing this connection weight by 5% on the contrast-response and velocity-response curves. The hysteretic amplifier's contrast-response changes very substantially, and becomes much more linear, as in the proportional amplifier model. For bars moving at 2 deg/sec, the proportional amplifier's contrast-response curve is not much affected. But at low velocities the response shows a large decrease. The selective action at low velocities is explained by the much larger gain (and larger α) at those velocities (see Section 4.5).

7.3.4 Inhibition strength

Inhibition shortens the duration of the stimulus by cutting off the LGN input (see Fig. 4.5b, Section 4.2). Increasing inhibition by 20% should shorten the stimulus duration and decrease the response if it is limited by the network dynamics. There is a strong effect in the hysteretic amplifier's contrast-response curve, but no significant change for the proportional amplifier (Fig. 7.5a and b). In this figure, we increased only $GABA_A$ inhibition for the proportional amplifier, and not $GABA_B$, but the

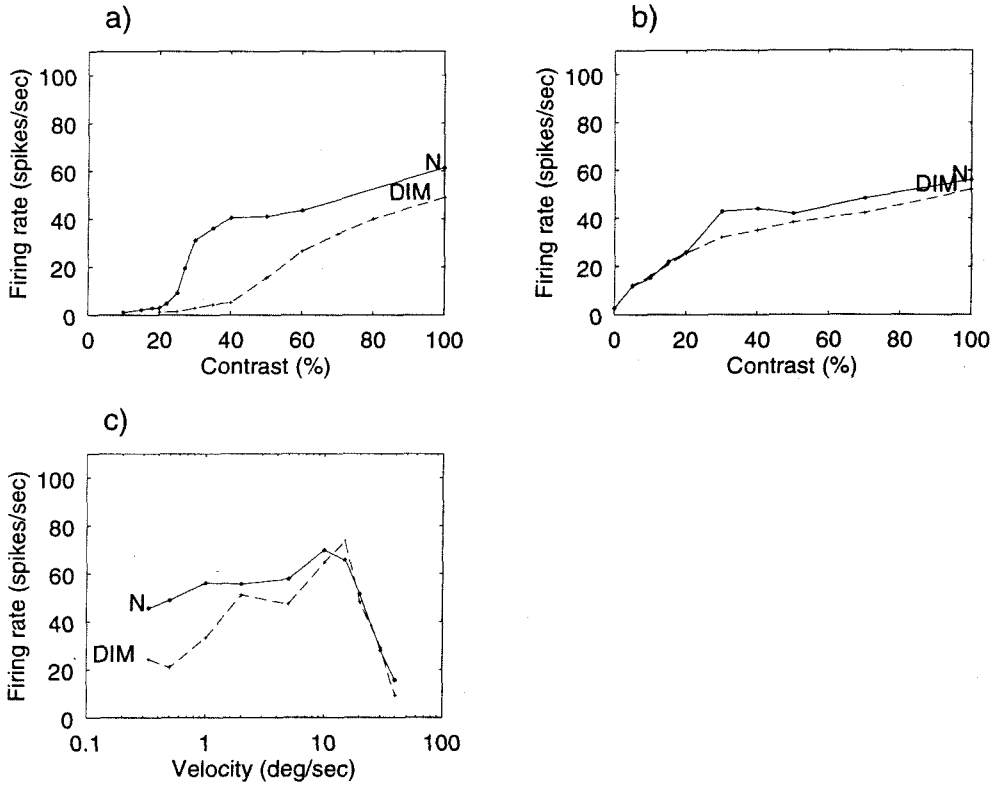

Figure 7.4: **Dependence of the contrast-response and velocity-response curves on feedback strength.** **(a)** Contrast-response curve to moving gratings (1 Hz, 1 c/deg) for the normal hysteretic amplifier (N, continuous) and when the strength of the excitatory connection between pyramidal cells has been diminished by 5% (DIM, dashed). **(b)** Same as (a) but for the proportional amplifier. **(c)** Same as (b) but velocity-response curve to bars (2 deg/sec) instead of contrast-response curve. The hysteretic amplifier shows the largest decrease in firing rate, but in the proportional amplifier the response diminishes very substantially at low velocities.

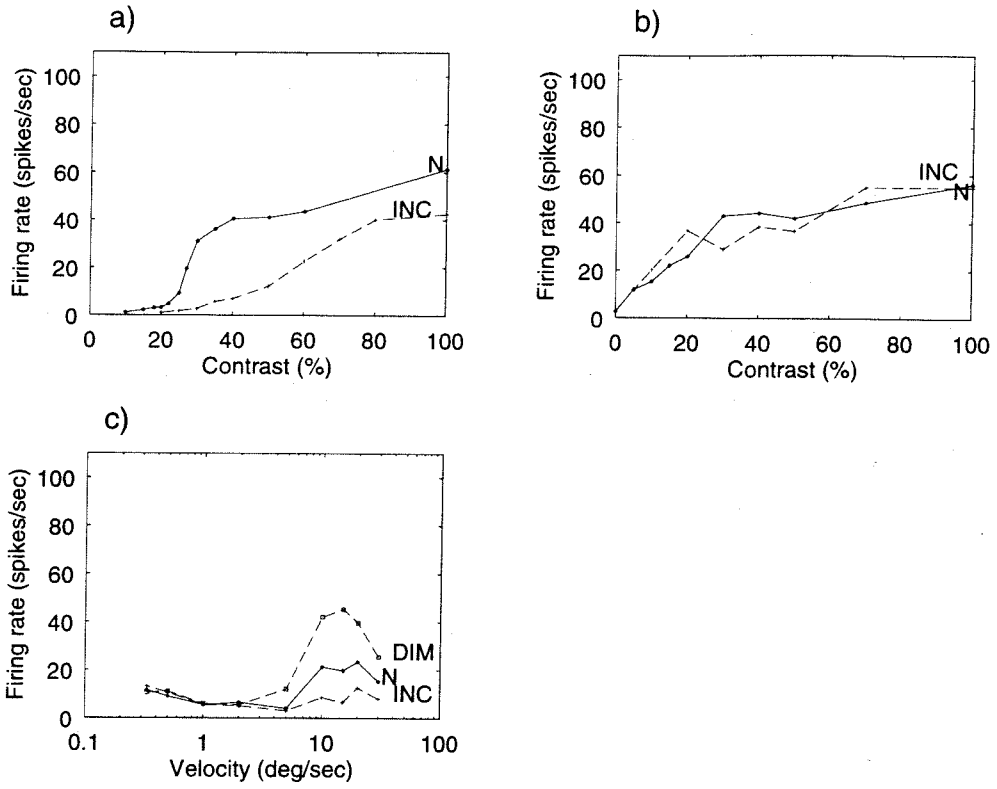

Figure 7.5: **Dependence of the contrast-response and velocity-response curves on inhibition strength.** **(a)** Contrast-response curve to moving gratings (1 Hz, 1 c/deg) for the normal hysteretic amplifier (N, continuous) and when the strength of both $GABA_A$ and $GABA_B$ inibition are increased by 20% (INC, dashed). **(b)** Same as (a) but for the proportional amplifier, and only $GABA_A$ inhibition is diminished. **(c)** Velocity-response curve to bars (2 deg/sec) for the proportional amplifier (N), when $GABA_A$ inhibition only is increased by 20% (INC), or decreased by 20% (DIM). There are very subtantial changes in the contrast-response curve for the hysteretic amplifier, and at high velocities for the proportional amplifier, showing strong parameter sensitivity.

difference can probably not be attributed to that. Indeed, $GABA_B$'s onset is delayed and so it probably does not influence stimulus duration much. Rather, the difference can probably be attributed to the hysteretic amplifier's higher threshold, which can be noticed by comparing Fig. 7.5a and b; the higher threshold results in a shorter stimulus duration, so that the response tends to be more strongly limited by the dynamics.

Inhibition is also responsible for direction selectivity by cancelling out the LGN input in the null direction. Increasing or decreasing $GABA_A$ inhibition should change the responses in the null direction, especially at high velocities. We note just that in the velocity-response curve for the proportional amplifier model (Fig. 7.5c). The changes in firing rate are substantial, showing strong parameter sensitivity.

7.4 Bimodality: why 800 neurons in the hysteretic amplifier

When simulating the hysteretic amplifier, 800 cortical neurons and 1248 LGN neurons were needed, compared to only 50 cortical neurons and 65 LGN neurons for the proportional amplifier. If 50 cortical and 65 LGN neurons are used in the hysteretic amplifier, the responses show a surprising phenomenon. We show a raster plot (see Sections 4.2 and 5.2 for explanations about this plotting format) with several trials (Fig. 7.6a) and analyze the peak firing rates for each trial in Fig. 7.7a. Here, each data point plots the peak firing rate of the compound Post-Stimulus Time Histogram (PSTH), generated from all pyramidal neurons in the model (see Section 2.6), for a moving bar (2 *deg/sec*) as function of the bar's contrast, for each of many trials at a given contrast. The distribution of the peak firing rates per trial is clearly bimodal, showing firing rates that are almost exclusively either very low or very high.

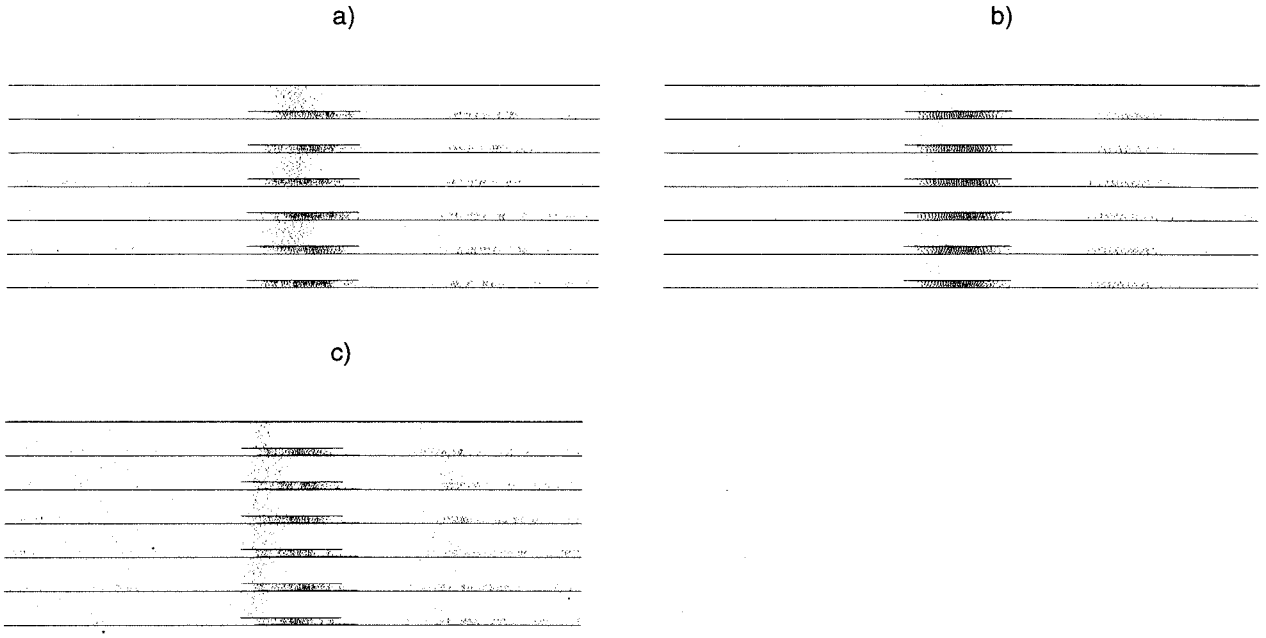

Figure 7.6: **Bimodality in the raster plots for the hysteretic amplifier with few neurons.** Response of pyramidal and smooth neurons to a bar moving at $2^{o}/sec$ in the preferred direction of motion. Six trials are shown for each of three parameter conditions of the cortical amplifier model. The first 40 rows in each trace indicate spiking activity in 40 pyramidal cells. The continuous bar just below these rows indicates when the stimulus is within the receptive fields of the LGN inputs to the pyramidal cells, and is approximately 300 *msec* in duration. The 10 rows below the bar correspond to firing activity in 10 smooth cells. **(a)** Hysteretic amplifier model with 50 cortical and 13 LGN neurons, 41% contrast. **(b)** Hysteretic amplifier model with 800 cortical neurons and 1248 LGN neurons, 52% contrast **(c)** Proportional amplifier model with 50 cortical and 13 LGN neurons, 30% contrast. The firing rate variability among trials is large in the hysteretic amplifier case with few neurons, but not in the other parameter conditions.

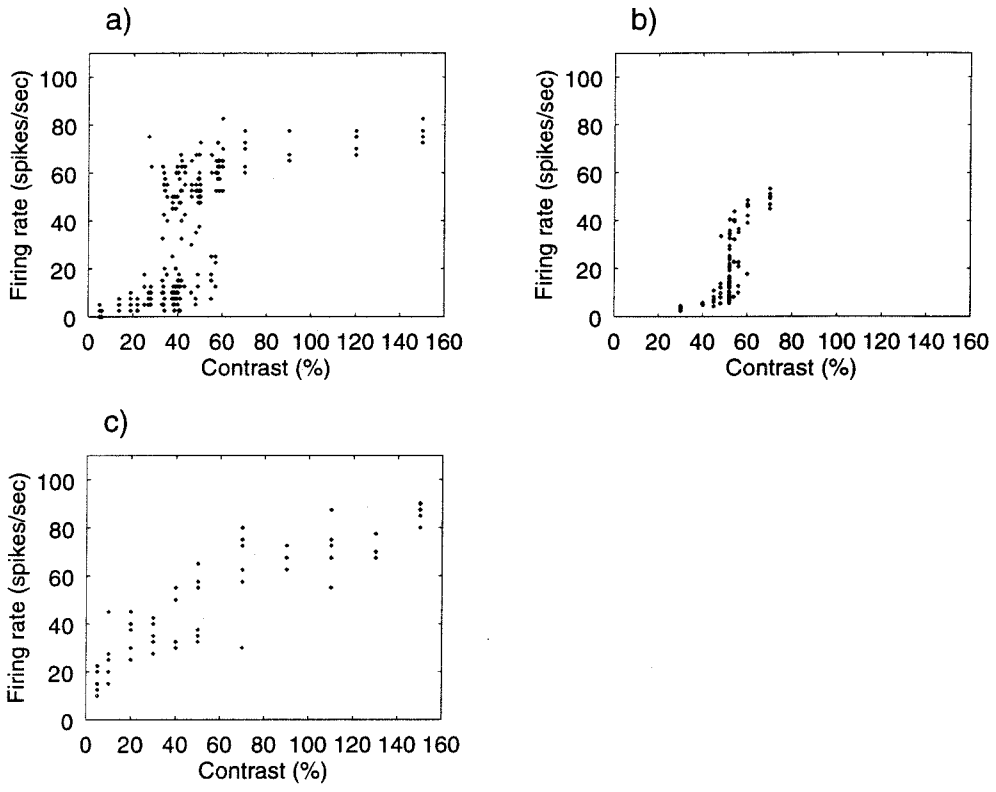

Figure 7.7: **Bimodality in the distribution of peak rates per trial for the hysteretic amplifier with few neurons.** For each of many individual trials of a moving bar stimulus (2 *deg/sec*) at many contrasts, peak firing rate for the pyramidal neurons (from the Post-Stimulus Time Histogram - PSTH summed over all pyramidal neurons) for **(a)** hysteretic amplifier model with 50 cortical and 13 LGN neurons; **(b)** hysteretic amplifier model with 800 cortical neurons and 1248 LGN neurons; **(c)** proportional amplifier model with 50 cortical and 13 LGN neurons. Bimodality of the distribution of peak firing rates is seen in the hysteretic amplifier case with few neurons only.

In other words, at each trial all model neurons either fail to discharge, or discharge very strongly. This phenomenon is apparently not seen in cat cortical neurons (see for instance Tolhurst et al., 1983). However, if we increase the number of neurons to 800/1248, we obtain the situation of Figs. 7.6b and 7.7b. While there is still a latent tendency for the peak firing rates to group around two values at intermediate contrasts, this trend is weak and over all contrasts the peak firing rates span the entire range. This situation can be contrasted with the proportional amplifier model. Even with few neurons, bimodality is not observed (Figs. 7.6c and 7.7c).

We provide the following explanation for this large trial-to-trial variability in the case with few neurons, with the caveat that we do not justify it in detail. Essentially, trial-to-trial noise in the system is amplified by the excitatory feedback. The mechanism for amplification of the noise is the exponential dynamics with positive exponent (see Sections 3.5 and 5.6). Noise in the individual neurons (originating from the current and synaptic noises, and the LGN input; see Section 2.5.1) causes random spikes when the stimulus brings the cortical neurons near threshold, resulting in firing rate noise in the network. Whenever the firing noise in the network is larger than the threshold of $F(f)$, the network turns on according to an exponential with a positive exponent. The stimulus duration is apparently considerably longer than the time constant of the network (and there are some indications that the time constant is shorter when there are few neurons); so for most trials, either the firing rate noise did not reach the network's threshold for the whole duration of the trial and the peak firing rate in the trial is small; or the firing rate noise reached at some point the threshold and the network has had time to rise to upper attractor's firing rate, so that the peak firing rate is large. The trials that have intermediate peak firing rates are only those few trials for which the firing noise reached the network's threshold within less than a time constant from the end of the trial.

How does this mechanism depend on the number of neurons? The spike mecha-

nism itself acts as noise amplifier. Indeed, small amounts of noise in a single neuron will result in a spike. The network average firing rate corresponding to this one spike at time t, *i.e.*, the corresponding firing rate noise, is a delta function:

$$f(t) = \frac{1}{N}\delta(t)\,, \tag{7.1}$$

where N is the number of neurons in the network (of course, in a discrete-time digital simulation, the delta function becomes a discrete-time impulse, with a finite height). The resulting firing rate noise is large for small neuron numbers, and becomes vanishingly small for very large neuron numbers. As a result, this noise amplification process becomes less and less prevalent as N increases, and the orderly buildup of network excitation with stimulus strength increasingly dominates, as in a firing rate model (see Sections 3.5 and 5.7).

Both current and synaptic noise of different neurons are not correlated, so that the firing rate noise averaged over all neurons originating from these sources will decrease quickly as N increases. However, single neuron noise resulting from the LGN input shows correlations due to common LGN inputs, and will not decrease as quickly (if at all). So increasing the number of LGN neurons is needed to reduce the correlated single neuron noise and ensure that the firing rate noise is small enough.

7.5 Conclusions and summary

Assumptions made in the model were simplified model neurons, that did not include many biophysical nonlinearities, the assumption of excitatory interconnections between neurons with similar direction selectivities, and the lack of excitatory connections from pyramids to smooth neurons. Because of amplification, model responses depend very strongly on some parameters, for instance neuron threshold, shape of the

network transfer function, and the strength of feedback excitation and feedforward inhibition; so, a major assumption of the model is that parameters of cortical neurons can be fine tuned to that extent by biological mechanisms. Possibly, adaptive mechanisms could help keep neurons in a valid operating range, as in Abbott and LeMasson (1993).

However, this strong parameter sensitivity also suggests that transmitters that modulate ionic currents even slightly could easily exert strong control on cortical responses, just as long as each neuron in the network is modulated in the same way at the same time. Ca^{2+} currents can be blocked or modulated by various transmitters (Fisher et al., 1990; Plummer et al., 1991; Swandulla et al., 1991; Sayer et al., 1992; Cox and Dunlap, 1992). An M current can be reduced by activation of muscarinic receptors (McCormick and Williamson, 1989), and muscarinic fibers innervate cortex (Bear et al., 1985; De Lima and Singer, 1986). The presence of these transmitters even suggest experimental predictions. These transmitters could be applied to cortex during physiological experiments in amounts that result in only small modifications of neuronal thresholds (that can be measured by recording neuronal responses to visual stimuli or intracellular current injections). Such minute changes in thresholds might be expected to produce large changes in contrast-response curves.

Also, substances that change the amount of excitatory feedback, such as NMDA antagonists, are expected to change the contrast-response curve. However, the predictions are a lot more specific: NMDA antagonists should change more strongly hysteretic amplifier-type contrast-response curves and less strongly proportional amplifier-type curves. Also, hysteretic amplifier-type curves should be changed into proportional amplifier-type curves.

Finally, we have suggested that bimodality of the distribution of peak firing rates per trial originates from noise amplification through the attractor dynamics, and was a major problem for the hysteretic amplifier, but can be overcome by increasing the

number of neurons in the simulation.

Chapter 8

Conclusions

Interest in computational neuroscience has been sparked by the realization that experimental analysis is not enough to understand the information processing performed by neurons. This realization has been more acute in some cases, such as the cerebellum, whose function is still not very well understood; although its circuitry shows striking regularities, it has been difficult to correlate it with the underlying information processing task.

Visual cortex, however, has always seemed more accessible to immediate understanding. Response properties of neurons can be directly correlated with parameters of visual stimuli, leading to such intuitively appealing properties as retinotopy, receptive fields, direction selectivity, orientation selectivity, color opponency, and the like.

Nevertheless, there has also been a realization that vision is a very complex process; computer vision has been an ongoing research topic for many years, and even some simple tasks cannot be performed by artificial systems. With that realization, neuroscientists have had to confront the reality that understanding visual processing in the brain will require a combination of experimental and computational techniques.

There is a wealth of physiological and anatomical data about visual cortex and especially about primary visual cortex. A obvious first step for understanding the information processing is to understand the relations between the physiological and anatomical descriptions at the level of, say, primary visual cortex. This thesis fits in this framework, by attempting to provide an explanation for some response properties of visual cortex, in terms of the underlying circuitry, in this case a combination of feedforward, spatially displaced inhibition, and feedback excitation.

There are striking similarities between cortical responses and the model's responses, to moving bars and stationary and moving gratings. Furthermore, some of the radical transformations in response properties between LGN and cortex might be explained by the positive feedback, including strong responses at low velocities in cortex, and expansive and compressive nonlinearities in contrast-response curves.

This model clearly shows predictive power. Some of the results presented in this thesis came from predicting rather than fitting experimental data: for instance linearity to grating superposition and the experiment of Nelson et al. (1994). Further predictions were generated, about ways of modifying velocity-response and contrast-response curves selectively, and about a modified linearity test.

This model is also an example of how a hypothesis about cortical circuitry can be tested. Recent experimental results have provided firm support for the canonical microcircuit model (Douglas et al., 1988; Berman et al., 1992; Peters and Payne, 1993; Ahmed et al., 1994; Nelson et al., 1994; Peters et al., 1994). This model helps interpret these experimental results in a precise, quantitative way, and confirms intuition about the canonical microcircuit. By generating detailed predictions about cortical response properties, and confirming that the canonical microcircuit can explain many features of cortical response, this model goes a step further towards establishing it on sound theoretical foundations.

The model also demonstrates how the methodology of a physiological experiment

can be tested, and why it should be tested. The Jagadeesh et al. (1993) linearity test has been shown to lack sensitivity.

The model also made a provocative proposal about the operation of primary visual cortex: it may operate through hysteresis and attractor dynamics.

We have shown the extent of this model's parameter sensitivity, that is directly related to amplification. This sensitivity suggests that adaptive mechanisms in single cortical cells may be even more important than previously thought. Future research on the biological implementation and computational foundations of such adaptive mechanisms is needed.

This model has only scratched the surface of what can be modelled in visual cortex. The model is one dimensional, represents motion detection at only one spatial position, and we have examined its responses to only a subset of the stimuli that have been presented to cortical neurons. This is only a model of simple cells, and does not explain developpement of direction selectivity; neither does it deal with NMDA transmission. Validating other linearity tests is also a major possible application of future modeling.

Finally, we have not examined issues such as "Why amplification in primary visual cortex ?". "Why is the canonical microcircuit useful ?". Possibly, excitatory connections would allow responses in primary visual cortex to be selectively and strongly modified by visual memories stored in synaptic weights. Noise can be filtered out (Douglas et al., 1994a). Higher areas can influence the responses of visual cortical neurons, rather than having thalamic input provide most of the drive, possibly allowing the influence of higher cognitive processes. We leave these future exciting explorations to you, dear reader.

Chapter 9

Appendix: model parameters

9.1 Retino-geniculate module

The visual input to the entire model is a one-dimensional array of N_{pix} (150 in the model) real-valued image pixels. As in Victor (1987), the average luminance over both space and time was taken to be constant ($L_0 = 100\,cd/m^2$), and the input to the model (the value of the image pixels) was the fractional deviation from this mean luminance (the signed Weber fraction). Thus, the luminance $L(X,t)$ of the stimulus at a pixel X ($0 \leq X < N_{pix}$) and time t is:

$$L(X,t) = L_0[1 + s(X,t)]. \tag{9.1}$$

$s(X,t)$ is the value of the image pixels input to the model.

The input to the cortex itself is provided by our LGN model, which models the filtering operations of both retina and LGN as a single unit. A summary of the model parameters and their values is shown in Table ??.

A conduction delay $D = 4.4msec$ between LGN spikes and cortical synapses was also used , as in Victor (1987). This represents only the delay between the generation

T_s	0.1	$msec$	Sampling interval
A_0	300	Hz	Gain
M_0	8	Hz	Spont. firing rate
K_c	2		Strength of the ctr
σ_c	6	'	Std dev. of ctr's Gaussian fltr
K_s	1.88		Strength of surr.
σ_s	24	'	Std dev. of surr.'s Gaussian fltr
τ_L	1.94	$msec$	Time cst of 1st lowp. fltr
H	0.806		Strength of highp. fltr
τ_0	0.193	sec	Baseline time cst of highp. fltr
c_0	0.054		See eq. 9.8
τ_C	15	$msec$	Time cst for contrast measure

Table 9.1: **Parameters of the LGN model** For full definitions of the parameters, see text

of spikes in retinal ganglion cells and their arrival at the point in the optic tract where recordings are made.

The LGN output $y(t)$ consists of a center and a surround component. The output of the surround component is delayed by 3 $msec$ with respect to the center response (Enroth-Cugell *et al.*, 1983) and then substracted from the center output. The firing rate output $r(t)$ of the LGN model is computed as:

$$r(t) = |A_0 y(t) + M_0| \tag{9.2}$$

For the values of A_0 and M_0 see table 9.1. Spikes are then generated at each moment in time t from a Poisson process with mean $r(t)$. Both center and surround components have a similar structure: a Gaussian spatial filter acting on the image pixels

$$G(x, x_0) = \frac{K}{\sqrt{2\pi}\sigma} e^{-\frac{(x-x_0)^2}{2\sigma}} \tag{9.3}$$

is followed by a series of temporal filters that are responsible for the dynamics of

the LGN response (Victor, 1987). The only difference between the center and the surround lies in their spatial filters. Their temporal filters are identical.

Now we describe these temporal filters. Lowpass filters in the model are derived from the first-order leaky integrator. Its impulse response is a decaying exponential (time constant τ), in continuous time[1]:

$$h(t) = \frac{1}{\tau} e^{-t/\tau} \tag{9.4}$$

or in discrete time [2] (T_s is the sampling interval - the inverse of the sampling rate, $a = e^{-T_s/\tau}$):

$$h[n] = (1-a)a^n \tag{9.5}$$

and is implemented efficiently, in discrete time, using a difference equation ($x[n]$ and $y[n]$ are the filter's input and output at time n):

$$y[n] = (1-a)x[n] + ay[n-1]\,. \tag{9.6}$$

In the series of temporal filters for each of the center and surround, the first is a n_L-th order lowpass filter ($n_L = 16$ throughout this study; Victor, 1987), implemented as n_L first-order lowpass filters in series, each with time constant τ_L (see table). The second filter is a highpass filter, derived in the following way from the output $l[n]$ of a lowpass filter with time constant τ_S:

$$y[n] = x[n] - H\, l[n] \tag{9.7}$$

A particularity of this highpass filter is that τ_S is not constant; rather, a "neural

[1]Note that this filter is normalized, meaning that for a constant input, its output is the same as the input

[2]Note that this filter also normalized

measure of contrast" $c(t)$ is computed, as we will explain, and the value of τ_S is given by

$$\tau_S = \frac{\tau_0}{1 + \frac{c(t)}{c_0}}. \tag{9.8}$$

Thus the dynamics of the LGN response change when the neural measure of contrast changes. Usually this happens when the strength of the input changes. Indeed, to compute the neural measure of contrast, the output of the highpass filter is rectified by passing it through the following nonlinearity:

$$y[n] = |x[n]| \tag{9.9}$$

A first-order lowpass filter (time constant τ_C) is connected in series with the rectifier, and its output is the neural measure of contrast $c(t)$.

The values for most parameters of the LGN model were set to values that were found to be average for retinal ganglion cells (Victor, 1987), reflecting the similarity of retinal and LGN dynamics. However, the gain and spontaneous firing rate of the LGN neurons is different, so we chose for A_0 and M_0 values that were correspondingly different from those of retinal ganglion cells.

Choice of spatial filter parameters Enroth-Cugell and Robson (1966) and Linsenmeier et al. (1982) report a ratio σ_s/σ_c of 4. This is the value chosen by Wehmeier et al. (1989) in their simulations. We choose the same value. The ratio of the integrated center response to full field stimulation over the integrated surround response is 17/16 according to these two papers. Defining (as in Wehmeier et al., 1989, but differently from Enroth-Cugell and Robson, 1966; Linsenmeier et al., 1982) the spatial filter in two dimensions as:

$$\frac{K_c}{2\pi\sigma_c^2} e^{-\frac{r^2}{2\pi\sigma_c^2}} - \frac{K_s}{2\pi\sigma_s^2} e^{-\frac{r^2}{2\pi\sigma_s^2}}, \tag{9.10}$$

Compartment	Diameter μm	Length μm	Electrotonic length μm
Pyramidal			
Distal Apical	3	200	330
Proximal Apical	7	200	750
Soma	12.6	17.8	
Basal	15	200	486
Smooth			
Distal	5.4	140	330
Proximal	14.3	140	486
Soma	16.9	24.1	

Table 9.2: Compartmental parameters of the simplified model for the pyramidal and smooth neuron. Values of the diameter, lengths, and desired electrotonic lengths for each of the compartments of the two neurons. The somas are revolution ellipsoids and the other compartments are cylinders. For the somas, the diameter is the length of the ellipsoid in the two dimensions where the length is the same, and the length is the length in the third dimension. These dimensions were derived from dimensions of cells reconstructed from horseradish peroxidase injections. The desired electrotonic length is the electrotonic length estimated for the corresponding compartment in those reconstructions; the constraint that the compartments in the model have those electrotonic lengths is enforced by eq. 9.13.

where r is the distance from the center. The ratio of the integrated responses is K_c/K_s; Arbitrarily choosing $K_c = 2$, we arrive to a value of $K_s = 1.88$. If we choose $\sigma_c = 6'$ (and thus $\sigma_s = 24'$, the size of the effective center will be $30'$, as in Peichl and Wässle (1979) at 4.5^o eccentricity, which is the eccentricity we chose as in Wehmeier et al. (1989). Note however that we use the spatial filter in only one dimension, with the formula:

$$\frac{K_c}{\sqrt{2\pi}\sigma_c} e^{-\frac{r^2}{2\pi\sigma_c^2}} - \frac{K_s}{\sqrt{2\pi}\sigma_s} e^{-\frac{r^2}{2\pi\sigma_s^2}} . \tag{9.11}$$

It gives the same ratio of integrated center and surround response, and the same receptive field size.

9.2 Single cortical cell model and synapses

Each simplified compartmental neuron consists of an ellipsoidal somatic compartment, and two to three cylindrical compartments that represent the dendritic arbour (Table 9.2). The sizes of the compartments were obtained from summing the areas of the compartments obtained from reconstructing neurons injected with horseradish peroxidase. The termination conditions for the branches are sealed-end. The passive leak current is modeled as:

$$I_{leak} = G_{leak}(V - E_{leak}) \tag{9.12}$$

where V is the membrane potential. E_{leak} is given in Table 9.4. G_{leak} is computed from R_m, the surface membrane resistance, and the membrane area of the compartments, and the membrane capacitance is computed from C_m in a similar way. The axial resistance between two compartments was calculated so that the electrotonic length between the soma and any compartment of the simplified neurons is the same as in the neurons reconstructed from the horseradish peroxidase injections (and modeled by Bernander, 1993). To enforce this constraint, the intracellular resistivity was corrected for each compartment according to the desired electrotonic length; for compartment k, it is called $R_{i,c}^{(k)}$ and given by:

$$R_{i,c}^{(k)} = R_m \frac{d^{(k)}}{4 * (\lambda^{(k)})^2}. \tag{9.13}$$

$d^{(k)}$ is the diameter of compartment k and $\lambda^{(k)}$ is the desired electrotonic length of the compartment. The axial resistance between two compartments (say 1 and 2) is the sum of half of the axial resistance in each compartment, and depends on the corrected intracellular resistivity for each compartment, and the lengths and sections $l^{(k)}$ and

Compartment	Area $10^3 \mu m^2$	Axial Res. to next comp. $10^6 \Omega$
Pyramidal		
Distal Apical	1.88	105.6
Proximal Apical	4.4	8.09
Soma	0.64	8.99
Basal	9.42	-
Smooth		
Distal	2.37	44.5
Proximal	6.29	6.6
Soma	1.16	-

Table 9.3: Membrane areas and axial resistances for the compartmental models of the pyramidal and smooth neurons. The membrane areas of each compartment are given in μm^2, enabling the computatation of the leak resistances and capacitances of each compartment. These membrane areas can be computed from the diameters and lengths of the compartments given in Table 9.2. The axial resitances between each compartment and the next one in the table are also given, in Ω, enabling the computation of the currents flowing between compartments from the differences in potential between compartments. These axial resistances can be computed from the sizes of the compartments and the membrane resistance per unit area according to eq. 9.14 and 9.13.

$S^{(k)}$ of the two compartments:

$$R_a^{(1,2)} = R_{i,c}^{(1)} \frac{l^{(1)}}{2} / S^{(1)} + R_{i,c}^{(2)} \frac{l^{(2)}}{2} / S^{(2)} \tag{9.14}$$

The axial resistance of the soma is small, so it is not included in this calculation.

The results of these calculations, in terms of the membrane areas of the individual compartments and axial resistances between compartments, as used directly in the parameter files of the computer simulations, are shown in Table 9.3.

Synaptic conductances changes are described in Chapter 2, Section 2.5. Connection weights and time constants of the synapses are shown in Tables 2.1 and 2.2. The impulse responses of the synapses were implemented as two leaky integrators placed

C_m	2	$\mu F\, cm^{-2}$	Membrane cap. / area
R_m	10000	$\Omega\, cm^2$	Membrane leak res. / area
E_{Na}	50	mV	Na rev. potential
E_K	-90	mV	K rev. potential
E_{Cl}	-75	mV	Cl rev. potential
E_{Ca}	115	mV	Ca rev. potential
E_{leak}	-60	mV	Leak rev. potential
E_{exc}	0	mV	Exc. syn. rev. potential

Table 9.4: Other single cortical cell cortical parameters.

in series or a difference of two leaky integrators placed in parallel, or a plain leaky integrator (see eq. 9.6). All reversal potentials are shown in table 9.4. The reversal potential used to calculate the current flowing through a given synapse are that of Cl for $GABA_A$, K for $GABA_B$, and E_{exc} for the LGN and cortical excitatory synapses. A synaptic delay of 0.8 $msec$ (Wilson and Bower 1989) was used for all synapses, except the $GABA_B$ synapse where the delay was 2 $msec$.

The active ionic currents, Na, DR, Ca, Ca-K, A, and Na,p (Table 9.5 and 9.6), have corresponding gating "particles" m and h with first-order kinetics, as in the Hodgkin-Huxley model:

$$\frac{dX}{dt} = -\frac{(X - X_{ss})}{\tau} \qquad X\text{: } m \text{ or } h \tag{9.15}$$

The current depends on powers of m and h and on the driving potential:

$$I = Gmax \cdot m^k \cdot h^l \cdot (V - E_{rev}) \tag{9.16}$$

where E_{rev} is the ion's reversal potential; the reversal potentials for the different ions are given in Table 9.4, and the powers k and l and . A sigmoid function allows the computation of the steady-state value of any particle X_{ss} from the membrane

		$Gmax$ mS/cm^2	$V_{1/2}$ mV	θ mV	τ $msec$
Na	m^2h	200 (150)	-40|-45	-3|3	0.05|0.5
DR	m^2	120 (50)	-40	-3	3 (2)
Ca	m^2	0.75 (0)	-30	-4	2
Ca-dep K	m^2	3.2 (0)	0.04	3	2
A	m^2h	0.5 (0)	-65|-60	-2|4	20|100

Table 9.5: Parameters of the active ionic currents for the proportional amplifier model. Na is the fast Hodgkin-Huxley like sodium current, responsible for spiking, together with the delayed rectifier potassium current DR. Ca is the calcium current, activated after spiking. Ca-dep K is the calcium-dependent potassium current, activated by the calcium influx, and responsible for adaptation. A is the A-current, which allows firing at low rates for small input currents. Note that there is no persistent sodium current Na,p in the proportional amplifier, in contrast to the hysteretic amplifier model. Values of the peak conductance $Gmax$, the half- activation $V_{1/2}$, the steepness of the activation θ, and the time constant τ. Parameter values for both the m and the h particle are given separated by a |. Wherever applicable, parameter values for the smooth neurons are given in parenthesis when different. Note that for the calcium-dependent K current, $V_{1/2}$ is in $mmol/l$ and θ is a unitless quantity.

		$Gmax$ mS/cm^2	$V_{1/2}$ mV	θ mV	τ $msec$
Na	m^2h	200 (150)	-40|-45	-3|3	0.05|0.5
DR	m^2	100 (50)	-40	-3	4.5 (2)
Ca	m^2	0.4 (0)	-25	-4	2
Ca-dep K	m^2	5 (0)	0.04	3	2
Na,p	m^2	1 (0)	-40	-7	2

Table 9.6: Parameters of the active ionic currents for the hysteretic amplifier. Parameters of the active ionic currents for the proportional amplifier model. Na is the fast Hodgkin-Huxley like sodium current, responsible for spiking, together with the delayed rectifier potassium current DR. Ca is the calcium current, activated after spiking. Ca-dep K is the calcium-dependent potassium current, activated by the calcium influx, and responsible for adaptation. Na,p is a persistent sodium current. There is no A-current for the hysteretic amplifier, in contrast to the proportional amplifier model. For these currents, the table lists values of the peak conductance $Gmax$, the half-activation $V_{1/2}$, the steepness of the activation θ, and the time constant τ. Parameter values for both the m and the h particle are given separated by a | when both particles exist. Wherever applicable, parameter values for the smooth neurons are given in parenthesis when different. Note that for the calcium-dependent K current, $V_{1/2}$ is in $mmol/l$ and θ is a unitless quantity.

potential:

$$X_{ss} = \frac{1}{1 + e^{(V - V_{1/2})/\theta}} \tag{9.17}$$

There is one exception: the m particle of the Ca- dependent K current does not depend directly on the membrane voltage. Rather, its steady-state value depends on the concentration of calcium c (in $mmol/l$):

$$m_{ss} = \frac{\theta \cdot c}{c + V_{1/2}} \tag{9.18}$$

c is computed from the Ca current through a first-order differential equation:

$$\dot{c} = \alpha I_{Ca} - \frac{c}{\tau_{co}} \tag{9.19}$$

with $\alpha = 10^{10}\ mmol/(l \cdot A \cdot s)$ and $\tau_{co} = 50\ msec$. Another exception is that the h particle of A-current was reset to 1 whenever the neuron started a spike.

The excitatory and inhibitory noises represent the synaptic input from neurons outside the small network. This is one of the sources of random noise in the model. Transient events produced at random times are of two different kinds: either synaptic conductance changes or current injections. Events are generated from a Poisson process with a set rate R, The time course of each event is a dual exponential:

$$G(t) = e^{-t/\tau_1} - e^{-t/\tau_2} \tag{9.20}$$

or single exponential:

$$G(t) = e^{-t/\tau_1}\,. \tag{9.21}$$

The amplitude of these conductance or current events can be measured by the integral of the transient conductance or current change over time, in units of $pS \cdot sec$ or $pA \cdot sec$, and is given in Tables 9.7 and 9.8, as well as the time constants, for both smooth

Cond. or curr. In	Rate of events pyr./sm.	Integrated Pyramidal	strength smooth	Time τ_1	constants τ_2
Exc. conductance	4000	0.432	0.220	10	2
$GABA_B$ inh. cond.	500	0	8.28	40	10
Exc. current	200	0.3	0	10	
$GABA_A$ current	200	0.3	0	10	

Table 9.7: Parameters for the noise events in the proportional amplifier model. There are two types of noise events, conductance changes and current injections. There are both excitatory and inhibitory subtypes of noise events, distinguished by their reversal potential for the conductance noise, and their sign for the current noise. The inhibitory noise events are either $GABA_A$ or $GABA_B$, distinguished by their time constants and reversal potentials. The number of noise events per second (rate) are given for each of the types of noise. Noise events are generated from a Poisson distribution at those rates. The integrated strength of each noise event is the integral over time of the conductance or current increase, in units of $pS \cdot sec$ or $pA \cdot sec$, respectively, as in Tables 2.1 and 2.2, and is given for the noise events in both pyramidal and smooth neurons. The time courses of the noise events are either exponentials or differences of two exponentials, as in those tables, and the corresponding time constants are given, in $msec$.

Cond. or curr. In	Rate of events pyr./sm.	Integrated Pyramidal	strength smooth	Time τ_1	constants τ_2
Exc. conductance	4000	0.096	0.220	10	2
$GABA_B$ inh. cond.	500	0	8.28	40	10
Exc. current	200	0.3	0	10	
$GABA_A$ current	200	0.3	0	10	

Table 9.8: Parameters for the noise events in the hysteretic amplifier model. There are two types of noise events, conductance changes and current injections. There are both excitatory and inhibitory subtypes of noise events, distinguished by their reversal potential for the conductance noise, and their sign for the current noise. The inhibitory noise events are either $GABA_A$ or $GABA_B$, distinguished by their time constants and reversal potentials. The number of noise events per second (rate) are given for each of the types of noise. Noise events are generated from a Poisson distribution at those rates. The integrated strength of each noise event is the integral over time of the conductance or current increase, in units of $pS \cdot sec$ or $pA \cdot sec$, respectively, as in Tables 2.1 and 2.2, and is given for the noise events in both pyramidal and smooth neurons. The time courses of the noise events are either exponentials or differences of two exponentials (see eqs. 9.20 and 9.21). as in those tables, and the corresponding time constants are given, in $msec$.

and pyramidal neurons. For the excitatory conductance noise, the reversal potential is E_{exc} (see Table 9.4) and for the inhibitory $GABA_B$ conductance noise the reversal potential is that of K.

In addition to the leak current I_{leak} mentioned above, there is another constant leak conductance, in the smooth neurons only. This is an excitatory current with a reversal potential at 0 mV and a conductance of 0.75 nS. The main purpose of this current is to set the threshold of the smooth neurons appropriately.

References

Abbott LF, LeMasson G (1993) Analysis of neuron models with dynamically regulated conductances. Neural Comp 5:823-842.

Adelson EH, Bergen JR (1985) Spatiotemporal energy models for the perception of motion. J Opt Soc Am A 2:284-299.

Ahmed B, Anderson JC, Douglas RJ, Martin KAC, Nelson C (1994) Polyneuronal innervation of spiny stellate neurons in cat visual cortex. J Comp Neurol 341:39-49.

Ahmed B, Anderson JC, Douglas RJ, Martin KAC, Whitteridge D (1995) The current-discharge patterns of identified neurons in cat visual cortex. J Neurophysiol, submitted.

Albrecht DG, Geisler WS (1991) Motion selectivity and the contrast-response function of simple cells in the visual cortex. Visual Neuroscience 7:531-546.

Albrecht DG, Hamilton DB (1982) Striate cortex of monkey and cat: contrast-response function. J Neurophysiol 48:217-237.

Albus K (1980) The detection of movement direction and effects of contrast reversal in the cat's striate cortex. Vis Res 20:289-293.

Allman J, Miezin F, McGuiness E (1985) Stimulus spcific responses from beyond the classical receptive field - neurophysiological mechanisms for local global comparisons in visual neurons. Annu Rev Neurosci 8:407-430.

Amit DJ, Brunel N, Tsodyks MV (1994) Correlations of cortical hebbian reverberations: theory versus experiment. J Neurosci 14:6435-6445.

Baker CL, Cynader MS (1986) Spatial receptive-field properties of direction-selective neurons in cat striate cortex. J Neurophysiol 55:1136-1152.

Barlow HB, Levick WR (1965) The mechanism of directionally selective units in rabbit's retina. J Physiol 178:477-504.

Baumfalk U, Albus K (1988) Phaclofen antagonizes baclofen-induced suppression of visually evoked responses in the cat's striate cortex. Brain Research 463:398-402.

Bear MF, Carnes KM, Ebner FF (1985) An investigation of cholinergic circuitry in cat striate cortex using acetylcholinesterase histochemistry. J Comp Neurol 234:411-430.

Beaulieu C, Colonnier M (1983) The number of neurons in the different laminae of the binocular and monocular regions of area 17 in the cat. J Comp Neurol 231:180-189.

Bekkers JM, Stevens CF (1989) NMDA and non-NMDA receptors are co-localized at individual excitatory synapses in cultured rat hippocampus. Nature 341:230-233.

Benevento L, Creutzfeldt O, Kuhnt U (1972) Significance of intracortical inhibition in the visual cortex. Nature 238:124-126.

Berman NEJ, Wilkes ME, Payne BR (1987) Organization of orientation and direction selectivity in areas 17 and 18 of cat cerebral cortex. J Neurophysiol 58:676-699.

Berman NJ, Douglas RJ, Martin KAC, Whitteridge D (1991) Mechanisms of inhibition in cat visual cortex. J Physiol 440:697-722.

Berman NJ, Douglas RJ, Martin KAC (1992) GABA-mediated inhibition in the neural networks of visual cortex. In: Progress in brain research, vol. 90 (Mize RR, Marc RE, Sillito AM, eds), pp 443-476. Elsevier.

Bernander O (1993) Synaptic integration and its control in neocortical pyramidal cells. Ph.D. thesis, California Institute of Technology.

Bernander O, Douglas R, Martin K, Koch C (1991) Synaptic background activity influences spatiotemporal integration in single pyramidal cells. Proc Nat Acad Sci, USA 88:11569-11573.

Bernander O, Douglas RJ, Koch C (1994) Amplification and linearization of synaptic input to the apical dendrites of cortical pyramidal neurons. J Neurophysiol 72:2743-2753.

Bishop PO, Coombs JS, Henry GH (1971) Responses to visual contours: spatio-temporal aspects of excitation in the receptive fields of simple striate neurones. J Physiol 219:625-657.

Bliss TVP, Collingridge GL (1993) A synaptic model of memory: Long-term potentiation in the hippocampus. Nature 361:31-39.

Braitenberg V, Schüz A (1991) Anatomy of the cortex. Berlin, Germany: Springer-Verlag.

Bullier J, Norton TN (1979) Comparison of receptive-field properties of X and Y ganglion cells with X and Y lateral geniculate cells in the cat. J Neurophysiol 42:274-291.

Burr DC (1981) Temporal summation of moving images by the human visual system. Proc R Soc Lond B Biol Sci 211:321-339.

Busch C, Sakmann B (1990) Synaptic transmission in hippocampal neurons: numerical reconstruction of quantal IPSCs. Cold Spring Harbor symposia on quantitative biology LV:69-80.

Bush PC, Douglas RJ (1991) Synchronization of bursting action potential discharges in a model network of neocortical neurons. Neural Computation 3:19-30.

Bush PC, Sejnowski TJ (1993) Reduced compartmental models of neocrotical pyramidal cells. J Neuroscience Methods 46:159-166.

Carandini M, Heeger DJ (1994) Summation and division by neurons in primate visual cortex. Science 264:1333-1335.

Cleland BG, Lee BB (1985) A comparison of visual responses of cat lateral geniculate nucleus neurones with those of ganglion cells afferent to them. J Physiol 369:249-26.

Connors BW, Malenka RC, Silva LR (1988) Two inhibitory postsynaptic potentials, and GABA-A, and GABA-B receptor-mediated responses in neocortex of rat and cat. J Physiology 406:443-468.

Cox DH, Dunlap K (1992) Pharmacological discrimination of N-type from L-type calcium current and its selective modulation by transmitters. J Neuroscience 12:906-914.

Creutzfeldt OD, Kuhnt U, Benevento LA (1974) An intracellular analysis of visual cortical neurones to moving stimuli: responses in a co-operative neuronal network. Exp Brain Res 21:251-274.

Dawis S, Shapley R, Kaplan E, Tranchina D (1984) The receptive field organization of X-cells in the cat: spatiotemporal coupling and asymmetry. Vision Res 24:549-564.

De Lima AD, Singer W (1986) Cholinergic innervation of the cat striate cortex: a choline acetyltransferase immunocytochemical analysis. J Comparative Neurology 250:324-338.

Dean AF (1980) The contrast dependance of direction selectivity. J Physiol 303:38-39.

Dean AF (1981) The relationship between response amplitude and contrast for cat striate cortical neurons. JPhysiol 318:413-427.

DeAngelis GC, Ohzawa I, Freeman RD (1993) Spatiotemporal organization of simple-cell receptive fields in the cat's striate cortex. II. Linearity of temporal and spatial summation. JNeurophysiol 69:1118-1135.

Dehay C, Douglas RJ, Martin KAC, Nelson C (1991) Excitation by geniculocortical synapses is not 'vetoed' at the level of dendritic spines in cat visual cortex. J Physiol 440:723-734.

Derrington AM, Fuchs AF (1979) Spatial and temporal properties of x and y cells in the cat lateral geniculate nucleus. J Physiol (London) 293:347-364.

Douglas RJ, Martin KAC, Whitteridge D (1988) Selective responses of visual cortical cells do not depend on shunting inhibition. Nature 332:642-644.

Douglas RJ, Martin KAC, Whitteridge D (1989) A canonical microcircuit for neocortex. Neural Comput 1:480-488.

Douglas RJ, Martin KAC, Whitteridge D (1991) An intracellular analysis of the visual responses of neurones in cat visual cortex. J Physiol 440:659-696.

Douglas RJ, Mahowald MA, Martin KAC (1994a) Hybrid analog-digital architectures for neuromorphic systems. preprint.

Douglas RJ, Mahowald MA, Martin KAC (1994b) Hybrid analog-digital architectures for neuromorphic systems. In: Ieee international conference on neural networks, pp 1848-1853. Orlando:

Douglas RJ, Martin KAC (1990) Neocortex. In: The synaptic organization of the brain, 2nd edition (Shepherd GM, ed), pp 389-438. Oxford University Press, Oxford.

Douglas RJ, Martin KAC (1991) A functional microcircuit for cat visual cortex. J Physiol 440:735-769.

Dreher B, Sanderson KJ (1973) Receptive field analysis: responses to moving visual contours by single lateral geniculate neurones in the cat. J Physiol 234:95-118.

Duysens J, Orban G, Cremieux J (1985a) Velocity sensitivity in the cat visual system. Ii. Independence from interactions between different loci. J Neurophysiol 54:1050-1067.

Duysens J, Orban GA, Cremieux J, Maes H (1985b) Velocity selectivity in the cat visual system. III. Contribution of temporal factors. J Neurophysiol 54:1068-1083.

Duysens J, Maes H, Orban G (1987) The velocity dependence of direction selectivity

of visual cortical neurones in the cat. J Physiol 387:95-113.

Edwards FA, Konnerth A, Sakmann B (1990) Quantal analysis of inhibitory synaptic transmission in the dentate gyrus of rat hippocampal slices: a patch-clamp study. J Physiology 430:213-249.

Emerson RC, Gerstein GL (1977) Simple striate neurons in the cat. II. Mechanisms underlying directional asymmetry and directional selectivity. J Neurophysiol 40:136-155.

Enroth-Cugell C, Robson JG, Schweitzer DE, Watson AB (1983) Spatio-temporal interactions in cat retinal ganglion cells showing linear spatial summation. J Physiol 341:279-307.

Enroth-Cugell C, Robson JG (1966) The contrast sensitivity of retinal ganglion cells of the cat. J Physiol 187:517-552.

Eysel UT, Muche T, Wörgötter F (1988) Lateral interactions at direction-selective striate neurones in the cat demonstrated by local cortical inactivation. J Physiol 399:657-675.

Ferster D (1987) Origin of orientation-selective epsps in simple cells of cat visual cortex. J Neurosci 7(6):1780-1791.

Ferster D (1988) Spatially opponent excitation and inhibition in simple cells of the cat visual cortex. J Neurosci 8:1172-1180.

Ferster DL (1989) The synaptic inputs to simple cells of the cat visual cortex. In: Neural mechanisms of visual perception (Lam DMK, Gilbert CD, eds), pp 63-85.

Ferster D, Jagadeesh B (1992) Epsp-ipsp interactions in cat visual cortex studied with in vivo whole-cell patch recording. J Neurosci 12:1262-1274.

Fisher RE, Gray R, Johnston D (1990) Properties and distribution of single voltage-gated calcium channels in adult hippocampal neurons. J Neurophysiol 62:91-104.

Freund TF, Martin KAC, Somogyi P, Whitteridge D (1985a) Innervation of cat visual areas 17 and 18 by physiologically identified X- and Y-type afferents. II.

Identification of postsynaptic targets by GABA immunocytochemistry and Golgi impregnation. J Comp Neurol 242:275–291.

Freund TF, Martin KAC, Whitteridge D (1985b) Innervation of cat visual areas 17 and 18 by physiologically identified X- and Y-type afferents. I. Arborization patterns and quantitative distribution of postsynaptic elements. J Comp Neurol 242:263–274.

Frishman LJ, Schweitzer-Tong DE, Goldstein EB (1983) Velocity tuning of cells in dorsal lateral geniculate nucleus and retina of the cat. J Neurophysiol 50:1393-1414.

Fuster JM (1990) Inferotemporal units in selective visual attention and short-term memory. J Neurophysiol 64:681-697.

Fuster JM, Jervey JP (1980) Inferotemporal neurons distinguish and retain behaviorally relevant features of visual stimuli. Science 212:952-955.

Fuster JM, Jervey JP (1982) Neuronal firing in the inferotemporal cortex of the monkey in a visual memory task. J Neurosci 2:361-375.

Gabbott PLA, Martin KAC, Whitteridge D (1987) Connections bewteen pyramidal neurons in layer 5 of cat visual cortex (area 17). J Comp Neurol 259:364-381.

Gabbott PLA, Somogyi P (1986) Quantitative distribution of GABA-immunoreactive neurons in the visual cortex (area 17) of the cat. Exp Brain Res 61:323-331.

Ganz L (1984) Visual cortical mechanisms responsible for direction selectivity. Vision Res 24:3-11.

Gilbert CD, Wiesel TN (1983) Clustered intrinsic connections in cat visual cortex. J Neurosci 3:1116-1133.

Gilbert CD, Wiesel TN (1990) The influence of contextual stimuli on the orientation selectivity of cells in primary visual cortex of the cat. Vision Res 30:1689-1701.

Gizzi MS, Katz E, Schumer RA, Movshon JA (1990) Selectivity for orientation and direction of motion of single neurons in cat striate and extrastriate visual cortex.

J Neurophysiol 63:1529-1543.

Goodwin AW, Henry GH (1978) The influence of stimulus velocity on the responses of single neurones in the striate cortex. J Physiol 277:467-482.

Grieve KL, Sillito AM (1991) A re-appraisal of the role of layer vi of the visual cortex in the generation of cortical end inhibition. Exp Brain Res 87:521-529.

Gulyas B, Orban GA, Duysens J, Maes H (1987) The suppressive influence of moving textured backgrounds on responses of cat striate neurons to moving bars. J Physiology 57:1767-1791.

Gulyas B, Lagae L, Eysel U, Orban GA (1990) Corticofugal feedback influences the responses of geniculate neurons to moving stimuli. Exp Brain Res 79:441-446.

Hamilton DB, Albrecht DG, Geisler WS (1989) Visual cortical receptive fields in monkey and cat: spatial and temporal phase transfer function. Vision Res 29:1285-1308.

Hamos JE, Davis LD, Sterling P (1983) Four types of neuron in layer IVab of cat cortical area 17 accumulate 3H-GABA. J Comp Neurol 217:449-457.

Heeger D (1992) Normalization of cell responses in cat striate cortex. Visual Neuroscience 9:181-197.

Heeger DJ (1993) Modeling simple-cell direction selectivity with normalized, half-squared, linear operators. J Neurophysiol 70:1885-1898.

Holub RA, Morton-Gibson M (1981) Response of visual cortical neurons of the cat to moving sinusoidal gratings: response-contrast functions and spatiotemporal interactions. J Neurophysiol 46:1244-1259.

Hubel DH, Wiesel TN (1962) Receptive fields, binocular interaction and functional architecture in the cat's visual cortex. J Physiol 160:106–154.

Ikeda H, Wright MJ (1975) Spatial and temporal properties of sustained and transient neurones in area 17 of the cat's visual cortex. Exp Brain Res 22:363-383.

Jack J, Noble D, Tsien R (1975) Electric current flow in excitable cells. Oxford:

Clarendon Press.

Jagadeesh B, Wheat HS, Ferster D (1993) Linearity of summation of synaptic potentials underlying direction selectivity in simple cells of the cat visual cortex. Science 262:1901-1904.

Jones JP, Palmer LA (1987) An evaluation of the two-dimensional gabor filter model of simple receptive fields in cat striate cortex. J Neurophysiol 58:1233-1258.

Kaplan E, Purpura K, Shapley R (1987) Contrast affects the transmission of visual information through the mammalian lateral geniculate nucleus. J Physiol 391:267-288.

Koch C, Douglas R, Wehmeier U (1990) Visibility of synaptically induced conductance changes: theory and simulations of anatomically characterized cortical pyramidal cells. J Neurosci 10:1728-1744.

Koch C, Poggio T (1985) The synaptic veto mechanism: does it underlie direction and orientation selectivity in the visual cortex? In: Models of the visual cortex (Rose D, Dobson VG, eds), pp 408-419. John Wiley & Sons.

Kriegstein AR, LoTorco JJ (1990) Gabaergic synaptic currents in slices of neocortex analyzed with whole-cell and cell-detached patch-clamp techniques. In: Neuroscience abstr. 16, p 30.9.

LaCaille JC (1991) Postsynaptic potentials mediated by excitatory and inhibitory amino acids in interneurons of stratum pyramidale of the CA1 region of rat hippocampal slices in vitro. J Neurophysiol 66:1441-1454.

Larkman AU, Stratford KJ, Jack JJB (1990) Quantal analysis of excitatory synaptic transmission in the CA1 subfield of rat hippocampus in vitro. In: Oxford meeting, p 61P.

Lee B, Willshaw D (1978) Responses of the various types of cat retinal ganglion cells to moving contours. Vision Res 18:757-765.

Lennie P (1980) Parallel visual pathways: a review. Vision Res 20:561-594.

Li C, Creutzfeldt O (1984) The representation of contrast and other stimulus parameters by single neurons in area 17 of the cat. Pfluegers Arch 401:304-314.

Linsenmeier RA, Frishman LJ, Jakeila HG, Enroth-Cugell C (1982) Receptive field properties of X and Y cells in the cat retina derived from contrast sensitivity measurements. Vision Res 22:1173-1183.

Lytton WW, Sejnowski TJ (1991) Simulations of cortical pyramidal neurons synchronized by inhibitory interneurons. J Neurophysiol 66:1059-1079.

Maex R, Orban GA (1991) Subtraction inhibition combined with a spiking threshold accounts for cortical direction selectivity. Proc Natl Acad Sci USA 88:3549-3553.

Maex R, Orban GA (1992) A model circuit for cortical temporal low-pass filtering. Neural Computation 4:932-945.

Martin KAC (1984) Neuronal circuits in cat striate cortex. In: Cerebral Cortex. Vol. II. Functional Properties of Cortical Cells (Jones EG, Peters A, eds), pp 241-284. New York and London: Plenum Press.

Martin KAC, Somogyi P, Whitteridge D (1983) Physiological and morphological properties of identified basket cells in the cat's visual cortex. Exp Brain Res 50:193-200.

Martin KAC, Somogyi P (1985) Local excitatory circuits in area 17 of the cat. In: Models of the Visual Cortex (Rose D, Dobson VG, eds), pp 504-513. Chichester: John Wiley and Sons.

Mason A, Nicoll A, Stratford K (1991) Synaptic transmission between individual pyramidal neurons of the rat visul cortex. J Neurosci 11:72-84.

McCormick DA, Connors BW, Lighthall JW, Prince DA (1985) Comparative electrophysiology of pyramidal and sparsely spiny stellate neurons of the neocortex. J Neurophysiol 54:782-806.

McCormick DA, Williamson A (1989) Convergence and divergence of neurotransmitter action in human cerebral cortex. Proc Natl Acad Sci USA 86:8098-8102.

McLean J, Raab S, Palmer LA (1994) Contribution of linear mechanisms to the specification of local motion by simple cells in areas 17 and 18 of the cat. Visual Neuroscience 11:271-294.

McLean J, Palmer L (1989) Contribution of linear spatiotemporal receptive field structure to velocity selectivity of simple cells in area 17 of cat. Vision Res 29:675-679.

McLean J, Palmer LA (1994) Organization of simple cell responses in the three-dimensional (3-D) frequency domain. Visual Neuroscience 11:295-306.

Mel B (1994) Information processing in dendritic trees. Neural Computation 6:1031-1085.

Miles R, Wong RKS (1984) Unitary inhibitory synaptic potentials in the guinea-pig hippocampus in vitro. J Physiology 356:97-113.

Miller KD (1992) Models of activity-dependent neural development. Seminars Neurosci 4:61-73.

Movshon JA, Thompson ID, Tolhurst DJ (1978) Spatial and temporal contrast sensitivity of neurones in areas 17 and 18 of the cat visual cortex. J Physiol 283:101-120.

Nelson S, Toth L, Sheth B, Sur M (1994) Orientation selectivity of cortical neurons during intracellular blockade of inhibition. Science 265:774-777.

Ohzawa I, Sclar G, Freeman RD (1982) Contrast gain control in the cat visual cortex. Nature 298:266-268.

Orban GA (1984) Neuronal Operations in the Visual Cortex. Berlin Heidelberg NewYork Tokyo: Springer-Verlag.

Orban GA, Kennedy H, Maes H (1981a) Response to movement of neurons in areas 17 and 18 of the cat: velocity sensitivity. J Neurophysiol 45:1043-1058.

Orban GA, Kennedy H, Maes H (1981b) Response to movement of neurons in areas 17 and 18 of the cat: direction selectivity. J Neurophysiol 45:1059-1073.

Orban G, Hoffmann KP, Duysens J (1985) Velocity selectivity in the cat visual system. I.Response of LGN cells to moving bar stimuli: a comparison with cortical areas 17 and 18. J Neurophysiol 54:1026-1049.

Orban GA, Kennedy H, Bullier J (1986) Velocity sensitivity and direction selectivity of neurons in areas V1 and V2 of the monkey: influence of eccentricity. J Neurophysiol 56:462-480.

Orban GA, Gulyas B, Spileers W, Maes H (1987) Responses of cat striate neurons to moving light and dark bars: changes with eccentricity. J Opt Soc Am 4:1653-1665.

Palmer LA, Davis TL (1981) Comparison of responses to moving and stationary stimuli in cat striate cortex. J Neurophysiol 46:277-295.

Payne BR, Berman N, Murphy EH (1980) Organization of direction preferences in cat visual cortex. Brain Res 211:445-450.

Pei X, Volgushev M, Vidyasagar TR, Creutzfeldt OD (1991) Whole cell recording and conductance measurements in cat visual cortex in-vivo. NeuroReport 2:485-488.

Peichl L, Wässle H (1979) Size, scatter, and coverage of ganglion cell receptive field centres in the cat retina. J Physiol 291:117-141.

Peters A, Payne BR, Rudd J (1994) A numerical analysis of the geniculocortical input to striate cortex in the monkey. Cerebral Cortex 4:215-229.

Peters A, Payne BR (1993) Numerical relationships between geniculocortical cell modules in cat primary visual cortex. Cerebral Cortex 3:69-78.

Plummer MR, Rittenhouse A, Kanevsky M, Hess P (1991) Neurotransmitter modulation of calcium channels in rat sympathetic neurons. J Neuroscience 11:2339-2348.

Press WH, Teukolsky SA, Vetterling WT, Flannery BP (1992) Numerical recipes in C (2nd edition). Cambridge: Cambridge University Press.

Press WA, Knierim JJ, Van Essen DC (1994) Neuronal correlates of attention to texture patterns in macaque striate cortex. Soc Neurosci Abstr 20:349:10.

Rapp M, Yarom Y, Segev I (1992) The impact of parallel fiber background activity on

the cable properties of cerebellar purkinje cells. Neural Computation 4:518-533.

Reid RC, Soodak RE, Shapley RM (1987) Linear mechanisms of directional selectivity in simple cells of cat striate cortex. Proc Nat Acad Sci 84:'8740-8744.

Reid RC, Soodak RE, Shapley RM (1991) Directional selectivity and spatiotemporal structure of receptive fields of simple cells in cat striata cortex. J Neurosci 66:505-529.

Rodieck RW (1965) Quantitative analysis of cat retinal ganglion cell response to visual stimuli. Vision Res 5:583-601.

Ruff PI, Rauschecker JP, Palm G (1987) A model of direction-selective simple cells in the visual cortex based on inhibition asymmetry. Biol Cybern 57:147-157.

Saul AB, Humphrey AL (1990) Spatial and temporal response properties of lagged and nonlagged cells in cat lateral geniculate nucleus. J Neurophysiol 64:206-224.

Saul AB, Humphrey AL (1992) Temporal-frequency tuning of direction selectivity in cat visual cortex. Visual Neuroscience 8:365-372.

Sayer RJ, Schwindt PC, Crill WE (1992) Metabotropic glutamate receptor-mediated suppression of l-type calcium current in acutely isolated neocortical neurons. J Neurophysiol 68:833-842.

Schiller PH (1982) Central connections of the retinal ON and OFF pathways. Nature 297:580-583.

Schiller PH (1992) The ON and OFF channels of the visual system. Trends Neurosci 15:86-92.

Shapley R, Lennie P (1985) Spatial frequency analysis in the visual system. Ann Rev Neurosci 8:547-583.

Shapley R, Perry VH (1986) Cat and monkey retinal ganglion cells and their visual functional roles. Trends Neurosci 9:229-235.

Sherk H, Horton JC (1984) Receptive field properties in the cat's area 17 in the absence of ON-center geniculate input. J Neurosci 4:381-393.

Sherman SM (1985) Functional organization of the W-, X-, and Y-cell pathways in the cat: a review and hypothesis. Progr Psychobiol Physiol Psychol 11:233-314.

Sillito AM (1975) The contribution of inhibitory mechanisms to the receptive field properties of neurones in the striate cortex of the cortex of the cat. J Physiol 250:305-329.

Sillito AM (1977) Inhibitory processes underlying the directional specificity of simple, complex and hypercomplex cells in the cat's visual cortex. J Physiol 271:699-720.

Sillito AM, Grieve KL, Cudeiro J, Davis JN (1994) Spatial integration and response correlation in the central visual system of cat and monkey. Soc Neurosci Abstr 20:608.10.

Swandulla D, Carbone E, Lux HD (1991) Do calcium channel classifications account for neuronal calcium channel diversity? Trends Neurosci 14:46-51.

Tanaka K (1983) Cross-correlation analysis of geniculostriate neuronal relationships in cats. J Neurophysiol 49:1303-1318.

Thomson AM, Girdlestone D, West DC (1988) Voltage-dependent currents prolong single-axon postsynaptic potentials in layer III pyramidal neurons in rat neocortical slices. J Neurophysiol 60:1896-1907.

Tolhurst DJ, Dean AF (1991) Evaluation of a linear model of directional selectivity in simple cells of the cat's striate cortex. Visual Neuroscience 6:421-428.

Tolhurst DJ, Dean AF, Thompson ID (1981a) The dependence of response amplitude and variance of cat visual cortical neurones on stimulus contrast. Exp Brain Res 41:414-419.

Tolhurst DJ, Dean AF, Thompson ID (1981b) Preferred direction of movement as an element in the orgenization of cat visual cortex. Exp Brain Res 44:340-342.

Tolhurst DJ, Movshon JA, Dean AF (1983) The statistical reliability of signals in single neurons in cat and monkey visual cortex. Vision Res 23:775-785.

Torre V, Poggio T (1978) A synaptic mechanism possibly underlying directional se-

lectivity to motion. Proc R Soc Lond B 202:409-416.

Victor JD (1987) The dynamics of the cat retinal X cell centre. J Physiol 386:219-246.

Watson AB, Ahumada AJ (1985) Models of human visual-motion sensing. J OptSocAm 2:322-342.

Wehmeier U, Dong D, Koch C, van Essen D (1989) Modeling the visual system. In: Methods in neuronal modeling (Koch C, Segev I, eds), pp 335-359. Cambridge, MA: MIT Press.

White EL (1989) Cortical circuits: synaptic organization of the cerebral cortex — structure, function and theory. Boston: Birkhauser.

Williams SH, Johnston D (1991) Kinetic properties of two anatomically distinct excitatory synapses in hippocampal CA3 neurons. J Neurophysiol 66:1010-1020.

Wilson MA, Bower JM (1989) The simulation of large-scale neural networks. In: Methods in neuronal modeling (Koch C, Segev I, eds), pp 291-333. Cambridge, MA: MIT Press.

Winfield DA, Gatter KC, Powell TPS (1980) An electron microscopic study of the types and proportions of neurons in the cortex of the motor and visual areas of the cat and rat. Brain 103:245-258.

Wolf W, Hicks TP, Albus K (1986) The contribution of gaba-mediated inhibitory mechanisms to visual response properties of neurons in the kitten's striate cortex. J Neurosci 6(10):2779-2795.

Wörgötter F, Niebur E, Koch C (1992) Generation of direction selectivity by isotropic intracortical connections. Neural Computation 4:332-340.

Wörgötter F, Holt G (1991) Spatiotemporal mechanisms in receptive fields of visual cortical simple cells: a model. J Neurophysiol 65:494-510.

Wörgötter F, Koch C (1991) A detailed model of the primary visual pathway in the cat: Comparison of afferent excitatory and intracortical inhibitory connection schemes for orientation selectivity. J Neurosci 11:1959-1979.

Zipser D, Kehoe B, Littlewort G, Fuster J (1993) A spiking network model of short-term active memory. J Neurosci 13:3406-3420.